Key Emerging Issues and Recent Progress related to Structural Materials Degradation

Author

François Cattant
Plescop, France

A.N.T. INTERNATIONAL®

Advanced Nuclear Technology International
Analysvägen 5, SE-435 33 Mölnlycke
Sweden

info@antinternational.com
www.antinternational.com

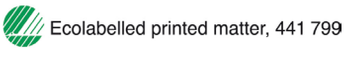
Ecolabelled printed matter, 441 799

Disclaimer

The information presented in this report has been compiled and analysed by Advanced Nuclear Technology International Europe AB (ANT International®) and its subcontractors. ANT International has exercised due diligence in this work, but does not warrant the accuracy or completeness of the information. ANT International does not assume any responsibility for any consequences as a result of the use of the information for any party, except a warranty for reasonable technical skill, which is limited to the amount paid for this assignment by each Project programme member.

Contents

1 Discussion and conclusion

1.1 General comments

This document is an extensive summary of the 17th Environmental Degradation of Materials in Nuclear Power Systems – Water Reactors held August 9-13, 2015 in Ottawa, Ontario, Canada.

The conference had 23 tracks and a poster session. The 23 tracks are listed hereafter:

- Irradiation damage
- IASCC characterization and mechanisms
- IASCC testing & engineering assessments
- PWR Ni alloy SCC tests
- PWR Ni alloy SCC precursors
- PWR Ni alloy SCC material factors
- PWR Stainless Steel SCC
- PWR stainless steel SCC testing
- PWR SCC Modeling
- PWR stainless steel corrosion fatigue
- PWR secondary side
- PWR oxides and deposits
- Welds and weld metals
- Welds, assessments and modeling
- Ferritic steel SCC & corrosion fatigue
- Ferritic steel FAC and other corrosion
- Plant operating experience
- BWR SCC and water chemistry
- BWR crack growth testing
- Low temperature corrosion and waste storage
- Zirconium and fuel cladding
- Fukushima
- Supercritical water corrosion

The poster session contained 13 additional papers; their abstracts are reported at the end of this document.

This report has five sections.

The first section contains brief descriptions (average of 5 to 10 lines) of each of the papers reviewed in order to give the reader an overview of the content of the original papers.

The second section contains extended summaries (in general 2 to 3 pages) of the papers.

The third section is the list of references.

The fourth section contains the nomenclature.

The last section is a unit conversion table.

1.2 Irradiation damage

This track has 10 papers.

4 papers deal with microstructural characterization, voids generation and swelling ([Garner F. et al, 2015a], [Fujii K. et al, 2015], [Gussev M. et al, 2015a] and [Stoller R. et al, 2015]).

3 papers are about the use of ion bombardment ([Garner F. et al, 2015b], [Changizian P. et al, 2015] and [Hosemann P. et al, 2015]).

2 papers are related to components: internals ([Hiser M. et al, 2015]) and cables ([Fifield L. and Duckworth R., 2015a]).

The last paper ([Nanstad R.K. et al, 2015]) relates to the Master Curve.

The first paper ([Garner F. et al, 2015a]) presents a summary of experimental observations and demonstrates that in principle the separation of the two competing processes which are void formation and phase formation can be accomplished. It is also shown that radiation-induced modification of physical properties allows in-situ non-destructive measurements to be used to measure swelling in LWR structural components. For relatively thin components, electro-resistive measurements appear to yield better results, but for thicker components ultrasonic techniques are more practical and effective. The impact of precipitate/void effects on data interpretation is also discussed, especially with respect to creep relaxation of preloaded components and for development of predictive correlations for void swelling and creep.

In the reference [Hiser M. et al, 2015], the authors use data from existing research programs and generate additional data from ion irradiation, fast reactor irradiation, near-light water reactor spectrum irradiation, and near-LWR spectrum further irradiation of harvested ex-plant materials in order to assess the behavior of reactor internals up to 80 years of irradiation. Highfluence irradiation assisted degradation may become more severe at neutron damage levels approaching or exceeding 80 displacements per atom accumulated during operation up to 80 years. There are several potential approaches for developing a technical basis related to IAD to support extended reactor operation up to 80 years. For each of the potential approaches considered, this paper summarizes both the technical and non-technical benefits and drawbacks.

Atom probe tomography is more and more used for microstructural characterization. The reference [Fujii K. et al, 2015] reports APT work carried out on stainless steel welds after long-term aging and irradiation to investigate the synergistic effects of thermal aging and neutron irradiation on weld material degradation. Phase decomposition into Fe-rich and Cr-rich phases was observed in the ferrite phase of two specimens. Differences in the phase decomposition between the two specimens were small, and no significant acceleration of phase decomposition under neutron irradiation was identified.

The reference [Gussev M. et al, 2015a] is also a microstructural characterization work. Deformation-induced $\gamma \rightarrow \alpha$ phase transformation and martensite accumulation are studied for Type 304 stainless steel irradiated to 5.8 dpa in a water-cooled power reactor. Deformation experiments were conducted at room temperature, and electron backscatter diffraction analysis was employed to investigate the structure of both deformed and non-deformed specimens. The morphology of strain-induced martensite and the role of stress on martensite particle size were analyzed in detail. The local misorientation evolution was investigated for different phases as a function of strain level.

Ion bombardment has been used successfully in earlier fast breeder and fusion materials programs to study the swelling behavior of simple metals and austenitic alloys, and more recently used on ferritic and ferritic martensitic alloys for fusion, fast and spallation reactor systems. Currently there is interest to apply this surrogate irradiation technique to help develop and test improved alloys for light water reactor service, especially with respect to development of accident-tolerant fuel cladding materials. The reference [Garner F. et al, 2015b] presents a review of those features of ion bombardment that simulate neutron-induced behavior and those that do not simulate as well. Some results of ongoing studies on ferritic martensitic alloys and their ODS variants are shown to illustrate the value of the charged particle simulation technique.

In the reference [Changizian P. et al, 2015], the ion bombardment is carried out employing the dual beam irradiation method with 1 MeV Kr^{2+} ions and 10 KeV He^{+} ions, in the temperature range of 200-500°C. The material here is Alloy X-750. In CANada Deuterium Uranium reactors X-750 is used for fuel channel spacers that maintain a gap between fuel channel pressure tubes and the surrounding calandria tubes. Ex-service CANDU spacers have been found to be embrittled. The change in properties is attributed to the neutron irradiation which leads to lattice defects and cavities in the structure of the alloy X-750. This study deals with the simulation of in-service, irradiation-induced microstructural changes in alloy X-750.

In the reference [Hosemann P. et al, 2015], 304SS irradiated with 2 MeV protons are used to assess mechanical property changes from room temperature to reactor operation temperature. Mechanical properties can be derived from small scale mechanical test data and directly compared to macroscopic values. Extending these techniques beyond basic investigations of model materials to reactor-relevant materials has several benefits. In principle, because the measurements can be site specific, the impact of microstructural/microchemical changes in the grain interior can be investigated separately from those that occur at the grain boundary. For ion-irradiated materials, measurements can be conducted entirely within the thin damage layer, unaffected by the non-irradiated substrate; and parameters associated with plastic deformation can be obtained, in addition to hardness. For neutron-irradiated materials, the small amount of material translates into greater ease of material sampling and examination, with significantly reduced concern about dose.

In the reference [Stoller R. et al, 2015], a modern cluster dynamics model has been used to investigate the materials and irradiation parameters that control microstructural evolution under the relatively low-temperature exposure conditions that are representative of the operating environment for in-core light water reactor components. The focus is on components fabricated from austenitic stainless steel. The model accounts for the synergistic interaction between radiation-produced vacancies and the helium that is produced by nuclear transmutation reactions. The results of the computational modeling are generally consistent with recent data obtained by examining exservice components. The long-term objective of this research is to provide a predictive model of void swelling at relevant lifetime exposures to support extended reactor operations.

The next paper is not related to RPV or RPV internals materials but to cables. The thousands of miles of polymer-insulated cables used for power, control and communications in nuclear power plants were originally qualified for forty years of plant operation. Continued use of cables in existing plants for periods greatly exceeding their original qualified life will require a detailed understanding of cable degradation under plant operating conditions to assess and mitigate the risk of continued use. The effect and relative importance of individual and combined environmental stresses including radiation, heat and moisture on reliable cable performance is essential to inform condition monitoring, lifetime prediction and required cable replacement planning. The reference [Fifield L. and Duckworth R., 2015a] presents an overview and update of the nuclear cable aging program at the Pacific Northwest National Laboratory and the Oak Ridge National Laboratory supported by the U.S. Department of Energy, Office of Nuclear Energy, Light Water Reactor Sustainability program.

One of the typical topics of these conferences is specimens size influence on mechanical testing results, the reference [Nanstad R.K. et al, 2015] belongs to this category. The Heavy-Section Steel Irradiation Program had previously irradiated five reactor pressure vessel steels/welds at fast neutron fluxes of about 4 to 8×10^{11} n/cm^2/s (>1 MeV) to fluences from 0.5 to 3.4×10^{19} n/cm^2 and at 288°C. The unirradiated fracture toughness tests were performed by Oak Ridge National Laboratory with 12.7-mm and 25.4-mm thick (0.5T and 1T) compact specimens, while the HSSI Program provided tensile and 5×10-mm three-point bend specimens to SCK•CEN for irradiation in the in-pile section of the Belgian Reactor BR2 at fluxes >10^{13} n/cm^2/s and subsequent testing by SCK•CEN. The BR2 irradiations were conducted at about 2 and 4×10^{13} n/cm^2/s with irradiation temperature between 295°C and 300°C (water temperature), and to fluences between 6 and 10×10^{19} n/cm^2.

1.3 IASCC characterization and mechanisms

This track has 8 papers.

In the references [Gussev M.N. et al, 2015b], [Chimi Y. et al, 2015] and [Stephenson K.J. and Was G.S., 2015] the test samples were irradiated by neutrons. In the reference [Gussev M.N. et al, 2015b],

2 Irradiation damage

The reference [Garner F. et al, 2015a] states that the precipitation effect is more prominent in more complex alloys with a greater range of precipitation. Therefore, for a first attempt to separate the contributions arising from voids and precipitation, it is best to focus on a simpler alloy, namely 304 stainless steel which is subject primarily only to carbide formation, especially $M_{23}C_6$. It also appears that in general the precipitate influence on the elastic properties is less pronounced than in the electrical resistance, so we will focus first on ultrasonic velocity.

In previous papers we described the examination of two hexagonal blocks of 304 stainless steel that were removed from a stack of five blocks (52 mm from one hex face to opposing face, with variable lengths, all at 240 mm or less) residing inside of a reflector assembly irradiated outside the EBR-II fast reactor core, experiencing dpa rates characteristic of PWR internals.

As shown in Figure 2-1, the blocks were labeled 1 to 5 with increasing elevation, with damage dose rate and gamma heating rate highest in the middle of Block 3. Four of these five blocks (#2-5) were subjected to non-destructive examination, and two of these (#3 and #5) were committed to extensive destructive examination thereafter. Measurement techniques employed were non-destructive profilometry and ultrasonic time-of-flight, the latter to map the internal distribution of through-thickness average swelling. Following cutting of the blocks into successively smaller pieces, additional ultrasonic time-of-flight measurements were made, as well as bulk density and void swelling measurements, the latter using electron microscopy. Over the stack there were significant axial and radial gradients in both dose and temperature, with gamma heating acting to cause significant internal temperature increases, producing a complex spatial distribution of void swelling within the block ensemble.

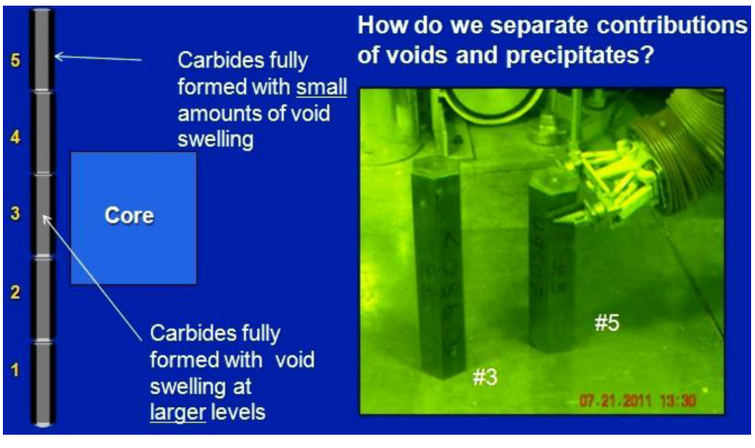

Figure 2-1: Schematic showing two hexagonal blocks (304 stainless steel) chosen for ultrasonic examination that have very different swelling distributions, but essentially the same carbon removal, allowing separation of void and precipitate contributions to changes in ultrasonic velocity [Garner F. et al, 2015a].

While profilometry measurements of block 3 clearly showed swelling dominating to produce an increase in face-to-face dimension, it was also clear that block 5 had experienced a decrease in these dimensions and it was clear from density measurements that block 5 had densified (Figure 2-2). When time-of-flight ultrasonic measurements were made from face-to-face it was clear that block 3 had indeed swollen and block 5 had significantly contracted in thickness.

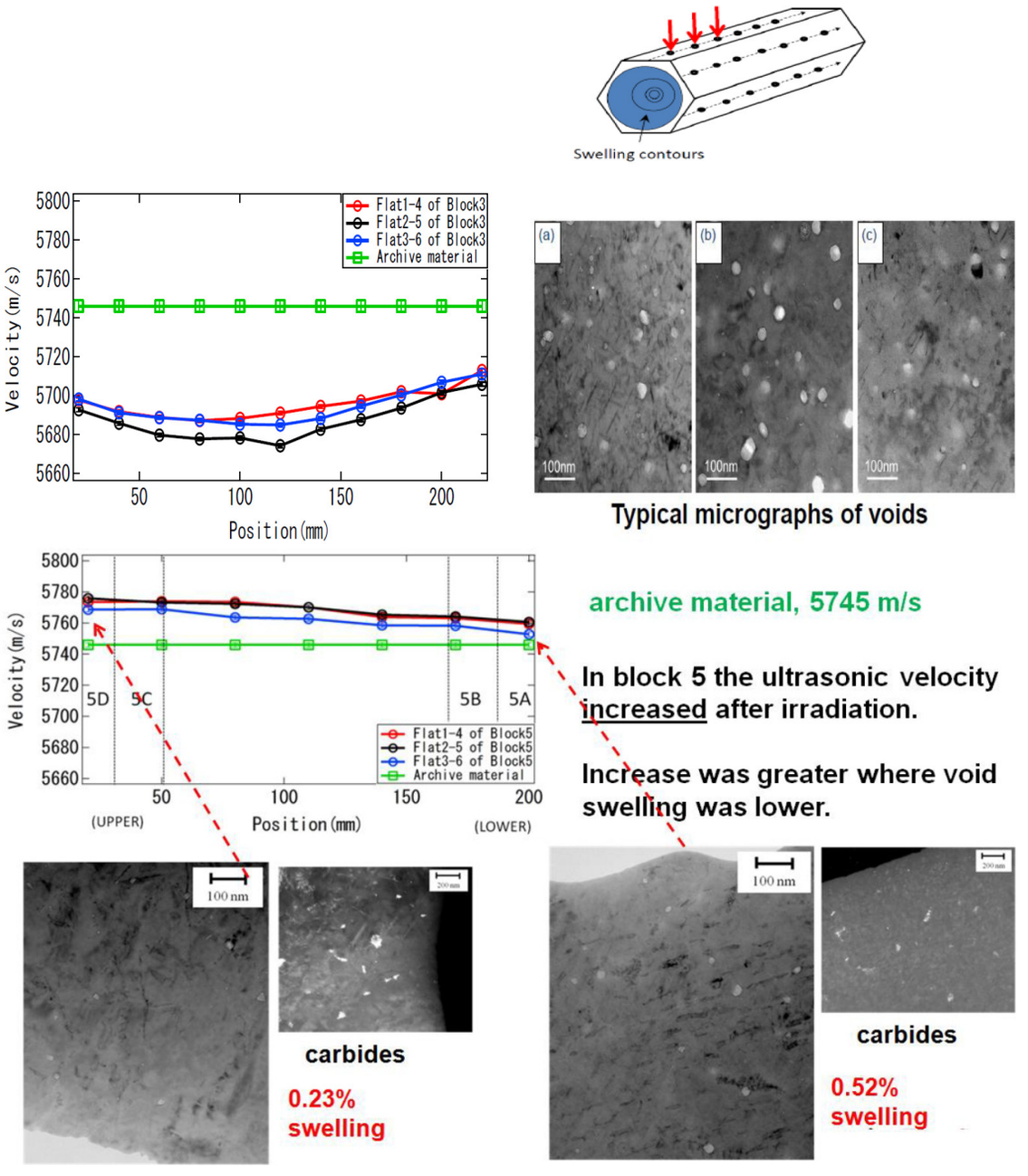

Figure 2-2: Ultrasonic time-of-flight measurements made from three sets of opposing faces of blocks 3 and 5, showing void swelling and carbide precipitation producing changes in ultrasonic velocity. Swelling in block 3 micrographs are a) 1.84, b) 2.76 and c) 1.95% at varying depths from the face midcenter on a 28 dpa iso-dose trace. Block 5 had much smaller amounts of swelling but similar carbides [Garner F. et al, 2015a].

After face-to-face measurements were made the blocks were cut into 2.5 cm thick hex-coins. Time-of-flight measurements were made across the cut-faces of the coin, producing swelling distribution maps that reflected the off-center but almost symmetrical swelling in block 3, a conclusion deduced earlier from profilometry measurements (Figure 2-3). Block 5 had much smaller variations, reflecting lower doses and lower gradients in both dose and temperature (Figure 2-4).

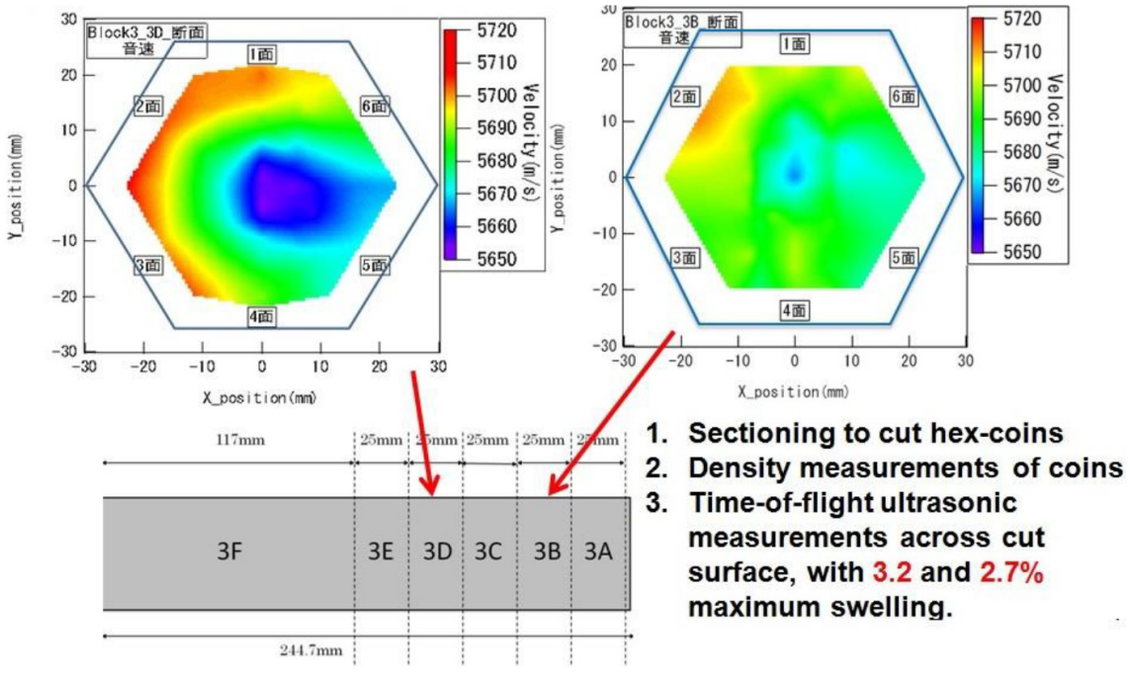

Figure 2-3: Typical distributions of ultrasonic velocity measured in block 3. Two of the five hex-coins are shown [Garner F. et al, 2015a].

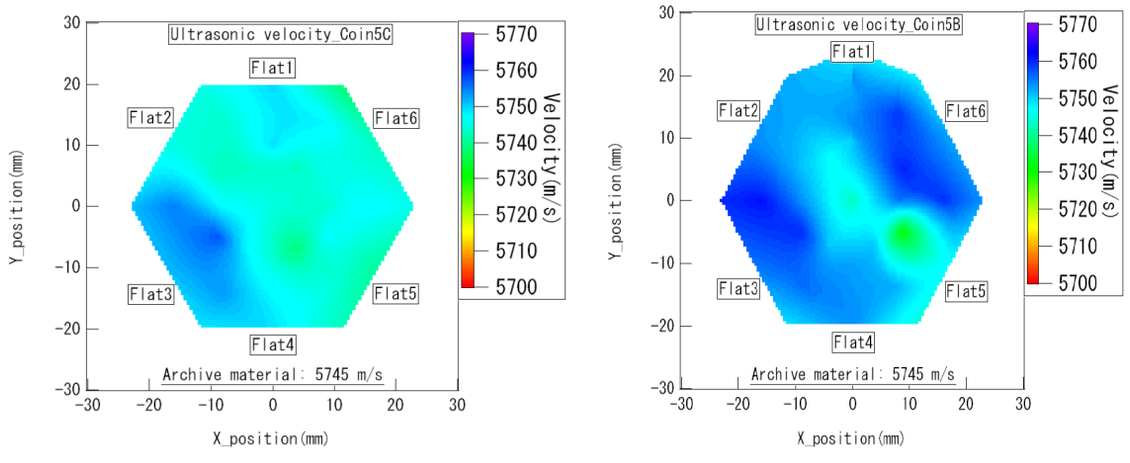

Figure 2-4: Distributions of ultrasonic velocity observed at top of block 5 (~0.3 dpa, left) and bottom of block 5 (~4 dpa, right). At the top of the block the variations in temperature and displacement dose are very small, producing very small variations in swelling and carbide distribution [Garner F. et al, 2015a].

Based on these data and additional data, it was possible to extract the relative contributions of voids and precipitates to the ultrasonic velocity, at least for this alloy. Thus it is possible to modify our understanding of the factors that determine the velocity, as shown below.

Unirradiated alloy

$$V = \sqrt{\frac{E(1-\nu)}{\rho(1+\nu)(1-2\nu)}}$$

V = ultrasonic velocity
E = elastic modulus
ρ = alloy density,
υ = Poisson's ratio.

Irradiated alloy

$$V = \sqrt{\frac{(1-2.5s+3.5c)E_0(1-\nu)}{(1-s+0.33c)\rho_0(1+\nu)(1-2\nu)}}$$

As shown in the equation above, the ultrasonic velocity is determined by decreases of 2.5% per 1% void swelling and increases of 3.5% per 1% carbide volume. The apparently large value for precipitation is put into better context when it is noted that the carbide volume is not very large.

While the time-of-flight method used in this study provides an average swelling over the thickness of the specimen, it appears to be possible to determine the depth dependence of swelling using more advanced ultrasonic techniques involving back-scatter of ultrasonic waves off of the voids and precipitates. More work is required to develop this opportunity, especially for application to in-situ swelling measurement in PWR cores.

Currently, the majority of commercial nuclear power plants in operation in the United States have received renewed licenses to operate for up to 60 years, and virtually all of the remaining plants have either applied or are expected to apply for a renewed license. In addition, there has been significant interest expressed by policymakers and the commercial power industry to determine if the technical basis can be developed for a subsequent license renewal of up to 80 years of operation. The Department of Energy Light Water Reactor Sustainability program and the Electric Power Research Institute are working to develop part of the technical basis for extended reactor operation. One of the key technical issues identified as requiring further research for operation up to 80 years is high-fluence irradiation-assisted degradation of reactor internals.

An approach to evaluating high-fluence IAD is to further irradiate ex-plant materials harvested from a decommissioned LWR to the fluence levels of interest using a near-LWR neutron energy spectrum. Further irradiation of ex-plant materials using ions or fast neutrons are other possible options. However, the advantages and disadvantages of these options are similar to those associated with starting with unirradiated material and are therefore not explicitly addressed in the reference [Hiser M. et al, 2015].

One example of such a program is to take the highest fluence materials that were harvested from the decommissioned Zorita reactor and further irradiate these materials to the target fluence of 80 dpa. These materials have a peak fluence of approximately 50 dpa generated from commercial PWR operation and would require an additional approximately 30 dpa to reach the target fluence. This section will consider the key aspects of a near-LWR spectrum neutron irradiation program starting with the highest dose Zorita materials to achieve high fluence levels of up to 80 dpa.

First, let's consider technical issues.

It is possible with a near-LWR spectrum neutron irradiation starting with irradiated ex-plant materials to achieve similar damage levels to those anticipated for in-service materials. The initial 50 dpa from in reactor service should provide highly representative irradiation conditions to currently operating PWRs. The 150 MWe Zorita reactor core was fairly small compared to larger commercial PWRs which means the reactor internals saw slightly higher fluxes (by about a factor of 2). However, the neutron flux, neutron energy spectrum, and irradiation temperature are quite representative of PWR conditions for the starting materials.

The main uncertainty associated with further irradiating materials that have been previously exposed under different irradiation conditions arises from the effects of flux and temperature. These parameters may affect the final microstructure developed from a further irradiation program when compared to continuous irradiation in a LWR reactor. Unlike the irradiation of virgin materials, there is limited data from further irradiation of previously irradiated microstructures to clearly determine the degree of

3 IASCC characterization and mechanisms

Austenitic AISI 304 and 316 stainless steels, as well as their numerous variants, are susceptible to irradiation-assisted stress corrosion cracking, which is one of the widely recognized and most severe issues associated with this class of materials in light water reactor operating environments. As the existing fleet of LWRs ages, IASCC-related issues are expected to become more severe; this aspect is under active investigation in the framework of the Light-Water Reactor Sustainability Program.

IASCC is a complex process involving many contributing factors including microstructural and microchemical changes induced by irradiation. At a high damage dose (20–40 dpa), stress corrosion cracking may occur even in a low potential corrosion environment, where a very low crack growth rate was observed in nonirradiated or low-dose irradiated materials. Recently, plastic strain and dislocation channeling leading to deformation localization have been recognized to play an important role in IASCC susceptibility. IASCC initiation in austenitic steels has been widely investigated using constant load tests, often with a particular focus on the stress level required for IASCC initiation. However, very limited data showing the influence of material variables, including grain orientation role on IASCC initiation, have been openly reported.

Constant-extension-rate tensile experiments conducted previously revealed multiple cracks in neutron-irradiated 304 steel specimens tested in a primary water environment. High crack density implied that crack nucleation occurred readily, but crack growth was suppressed or at least retarded. The main objective of the reference [Gussev M.N. et al, 2015b] was to investigate crack morphology (size, depth), crack propagation mechanisms, and other corrosion-related phenomena on these previously tested materials with a particular focus on aspects of crack initiation.

In the present work, the initiation of SCC and the early stage of IASCC was investigated for two commercial AISI 304L stainless steels irradiated by neutrons to 4.4–10.2 dpa and subjected to a constant extension rate test (3.5×10^{-7} s^{-1}) in a simulated primary water environment (temperature: 320°C, pressure: 12.4 MPa, 0 ppb O_2, 3,000 ppb H_2, –860 mVSHE).

While straining under these conditions, multiple cracks appeared at the surface, with intergranular cracking as a dominant mechanism. It was shown that intergranular cracks reached some length (~150–200 μm) and depth (~80–100 μm), blunted, and tended to coalescence with limited in-depth propagation (Figure 3-1). The reason for limited crack depth was not found but may be attributed to changes in the in-crack chemistry.

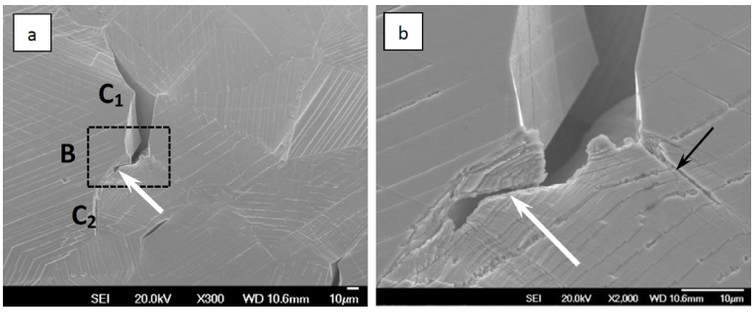

Figure 3-1: a) Cracks C1 and C2 demonstrate a tendency to coalescence via ductile or transgranular fracture (white arrows) of the bridge area (B).
b) Image showing high degree of plastic strain and channel density at the blunted crack tip. Note also oxidized grain boundary (black arrow) [Gussev M.N. et al, 2015b].

Crack initiation required some preliminary plastic deformation, roughly ~0.6% (Figure 3-2). No crack initiation was observed in the non-deformed part of the specimen. It was observed that dislocation channels at the surface might be sensitive to specific corrosion damage; some channels experienced oxidation along the slip plane.

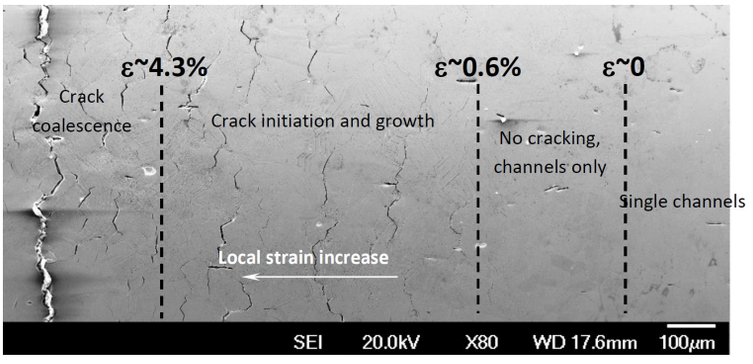

Figure 3-2: Surface of the deformed tensile bar with the strain levels shown (A-alloy) [Gussev M.N. et al, 2015b].

To analyze the local grain configurations, SEM-EBSD was employed, providing crystallography information on the orientation of grains adjacent to the cracks. It was found that grain orientation is an important factor influencing cracking. Grains oriented close to the [111] (with respect to the tensile direction) and the softest grains with a high Schmid factor were most often involved in crack initiation. Grains oriented close to [001] and [101] were much less sensitive to crack initiation. The grain orientation role extends and details the paradigm offered earlier, which included Schmid and Taylor factor analysis. The exact reason underlying the difference in the behavior of different grains is not clear at the moment.

In summary, it may be concluded that SCC initiation involves contributions from deformation localization, selective oxidation of deformation channels, and orientation of the adjacent grains including GB type. Additionally, factors limiting the depth of crack propagation under the primary water conditions exist.

Previous correlations have been observed between dislocation channeling and IASCC susceptibility in proton and neutron irradiated stainless steels, and it is believed that the high local stress at grain boundary – dislocation channel intersections induce crack initiation. Despite the results of previous studies, links between dislocation channeling and cracking in neutron irradiated stainless steel are very limited, and most analyses of cracking behavior are only made after the sample has been strained to the point of complete failure.

To better understand the crack initiation process and its mechanism, an experiment was devised to capture the initiation of IASCC cracks. A four-point bend test was chosen as the best option, due to the creation of a stress gradient through the sample thickness that will limit crack growth, but yield an area of uniaxial tensile stress and strain to enhance crack initiation site density. Previous bend test results on proton irradiated samples demonstrated the capability to determine tensile yield stress, therefore it was anticipated that results would be comparable to more traditionally used constant extension rate tensile (or slow strain rate tensile) experiments.

Previously, a variety of neutron irradiated stainless steels were tested in CERT experiments to determine their relative susceptibility to IASCC initiation. A set of these alloys was chosen for further study ([Stephenson K.J. and Was G.S., 2015]) based on their range in susceptibility, and small samples were removed from the un-deformed heads of the original tensile bars for use in the four-point bend test.

A novel SCC experiment was developed with the capability of creating SCC initiation while limiting crack propagation in highly embrittled neutron irradiated alloys. Experience in the development and use of the bend test has led to the following conclusions:

- Four-point bend tests are an effective way to create SCC initiation with limited crack propagation, allowing isolation of the mechanism of SCC initiation with a higher degree of accuracy than more commonly used tests.

- Results of the four-point bend test exhibit similarity to more widely used crack initiation tests such as CERT and constant load. The threshold stress required to initiate IASCC at ~40% of the irradiated yield strength indicates a stress-controlled initiation mechanism.

- Four-point bend testing of miniature samples creates a region of uniaxial tensile strain up to a total strain of ~2%. Regions of high tensile strain (strain peaks) form under center loading points at larger sample deflection, especially when testing materials with low yield strength. A gradient in uniaxial tensile strain exists along the sample length, which can yield important information regarding crack initiation or deformation behavior as a function of strain.

There are many possible mechanistic factors playing an important role in cracking advance during IASCC of austenitic stainless steels. It is known that one of the key factors is localized deformation which is specific for highly irradiated materials and can also affect the macroscopic mechanical properties. Localized deformation has been intensively studied recently for irradiated stainless steels to clarify the link between grain boundary properties and IASCC. For highly irradiated stainless steels, the locally deformed structure can be observed as surface steps due to dislocation slip along the dislocation channels under applying plastic strain.

Another approach to understand the mechanism of IASCC is characterization of oxidation inside the crack and at the crack tip. General features of oxides inside the crack in stainless steels under LWR simulated water chemistry conditions are known that (1) the oxides have dual-layered structure, (2) the inner (metal side) layer consists of chromium rich spinel oxide and (3) the outer (water side) layer consists of iron rich spinel oxide. Nickel enrichment in metal has been often observed at and ahead of the crack tip.

The actual IASCC crack growth occurs simultaneously with localized deformation and oxidation in the vicinity of the crack tip. However, the correlation between localized deformation and the oxidation has never been investigated systematically. The reference [Chimi Y. et al, 2015] attempts to link local deformation by controlled straining of specimens and the formation of oxide films during immersion tests on austenitic stainless steels neutron-irradiated to different doses to evaluate the synergy between localized deformation and oxidation in high-temperature water for highly irradiated materials.

Microstructural observations of locally deformed areas with up to ~2% plastic strain and oxide films on the deformed areas after immersion test were performed for highly irradiated (up to ~12 dpa) 316L SS using SEM and TEM with EDX. For the locally deformed structures, visible step structure was found on the specimen surface and was localized with increasing dose (Figure 3-3).

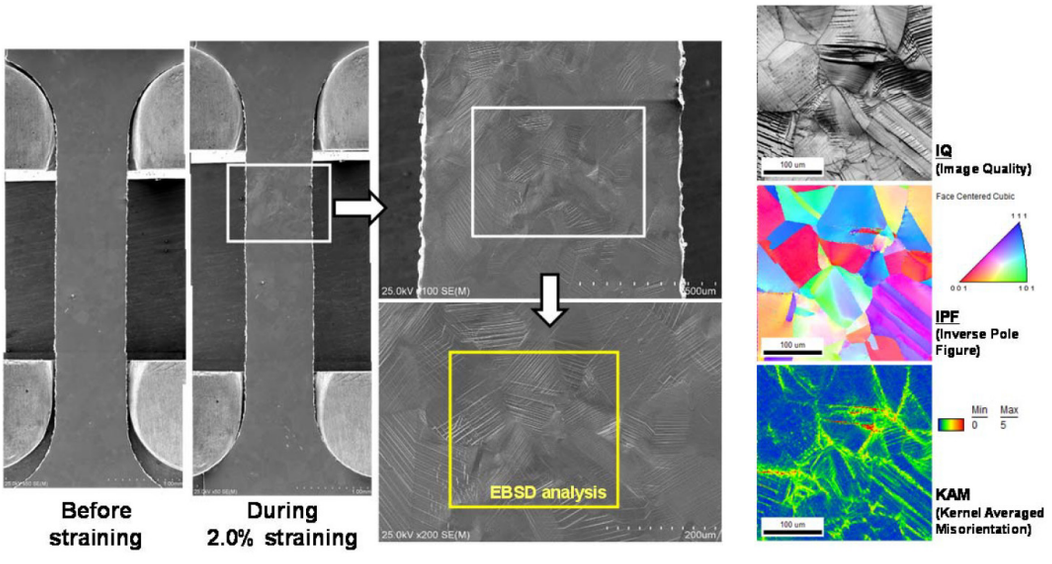

Figure 3-3: Typical observation by SEM and EBSD for 11.6-dpa irradiated specimen with 2.0% strain [Chimi Y. et al, 2015].

The coarse steps with large spacing were introduced firstly for 5.2- and 11.6-dpa irradiated specimen with 0.5% applied strain, and additional steps were produced between the coarse steps as the applied strain increases (Figure 3-4).

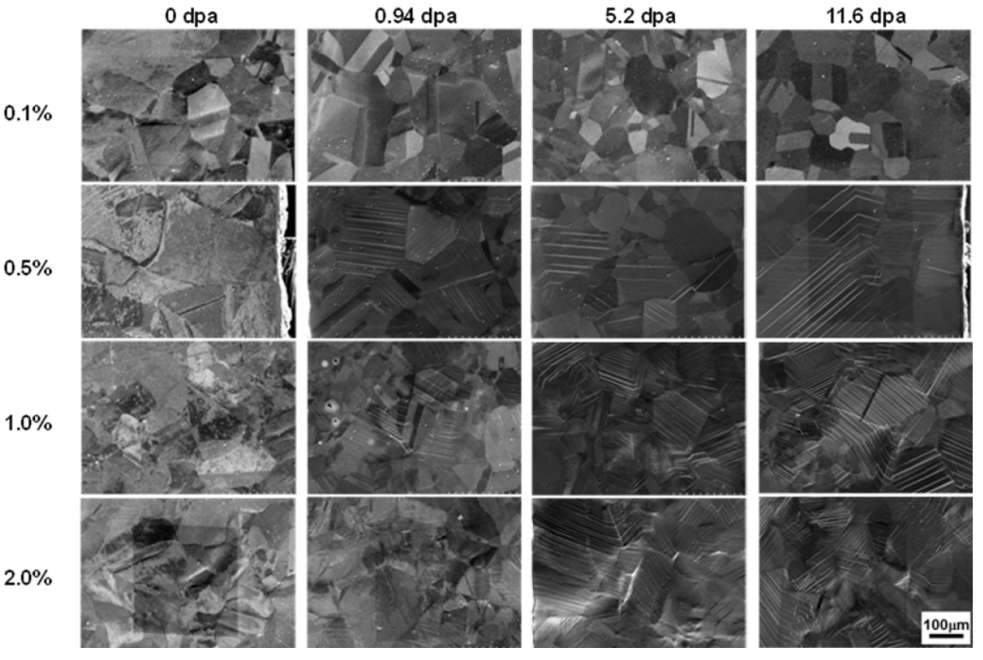

Figure 3-4: Comparison of SEM images of surface structure for all miniature tensile specimens [Chimi Y. et al, 2015].

The step structure for low-dose (0.94-dpa) specimen was caused not by dislocation channel but by tangling of dislocations, whereas the step structure was strongly related to the dislocation channel along with an edge of a twin for high-dose (11.6-dpa) specimen (Figure 3-5).

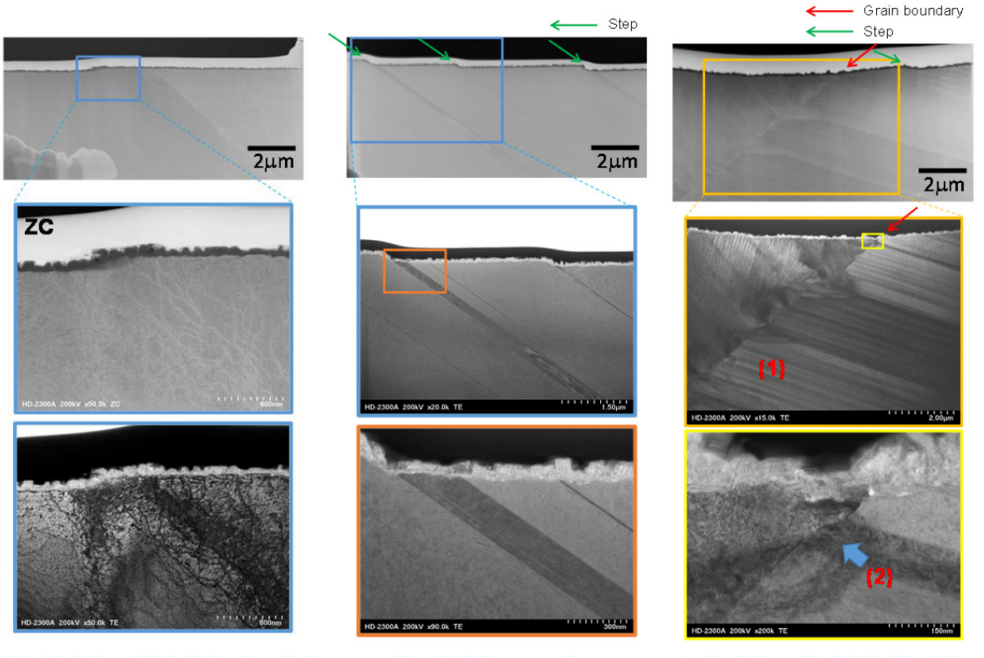

(a) 0.94 dpa, high KAM at GB (b) 11.6 dpa, matrix (c) 11.6 dpa, high KAM at GB

Figure 3-5: Typical TEM images of surface regions for 0.94- and 11.6-dpa irradiated specimens with 2.0% strain after immersion test [Chimi Y. et al, 2015].

4 IASCC testing & engineering assessments

The phenomenon of IASCC is principally caused by the microstructural and microchemical changes induced by irradiation, such as dislocation loops, voids, radiation hardeninradiation-induced precipitates, radiation-induced segregation, etc. All of these microstructural and microchemical changes can increase the cracking susceptibility of IASCC. However, no well-developed mechanism has been established. Radiation hardening is one of the important factors in IASCC. The increase of hardness is due to the microstructural changes after irradiation and results in an increase of yield strength and a decrease in ductility and fracture toughness. A consequence of radiation hardening is the development of localized deformation in which intense slip bands carry the strain in the solid. These slip bands are believed to be a key factor in IASCC. Radiation-induced segregation occurs at sinks and most prominently at grain boundaries. For austenitic alloys, RIS usually results in the depletion of Cr along with the enrichment of Ni and Si at grain boundaries. A drop in Cr content at grain boundaries could result in a thinner protective film (usually enriched in Cr) over the boundary. However, a direct linkage between irradiation induced grain boundary Cr depletion and IASCC has not been established.

The reference [Wang M. et al, 2015] focuses on the two age hardened nickel base alloys 625Plus and 725, and examines the IASCC behavior by using constant extension rate tests in simulated BWR water (288°C, 1500 psi, 2 ppm, dissolved oxygen and conductivity less than 1 μS/cm) on specially designed tensile bars that were irradiated by 2 MeV protons to a dose of approximately 5 dpa at a temperature of 360°C.

Annealing twins (dark contrast) were typically observed within every grain in both alloys, as shown in Figure 4-1 (a) and (b). Precipitates were randomly distributed and had a composition of (Nb, Ti) (C, N). The large particles were typically rich in Ti and N, while smaller precipitates were predominantly Nb and C. Statistical analysis was performed to determine the size distribution from more than 150 grains using the linear intercept method. The average grain size was 110 μm (Figure 4-1 (c)) and 60 μm (Figure 4-1 (d)) for alloy 625Plus and alloy 725, respectively.

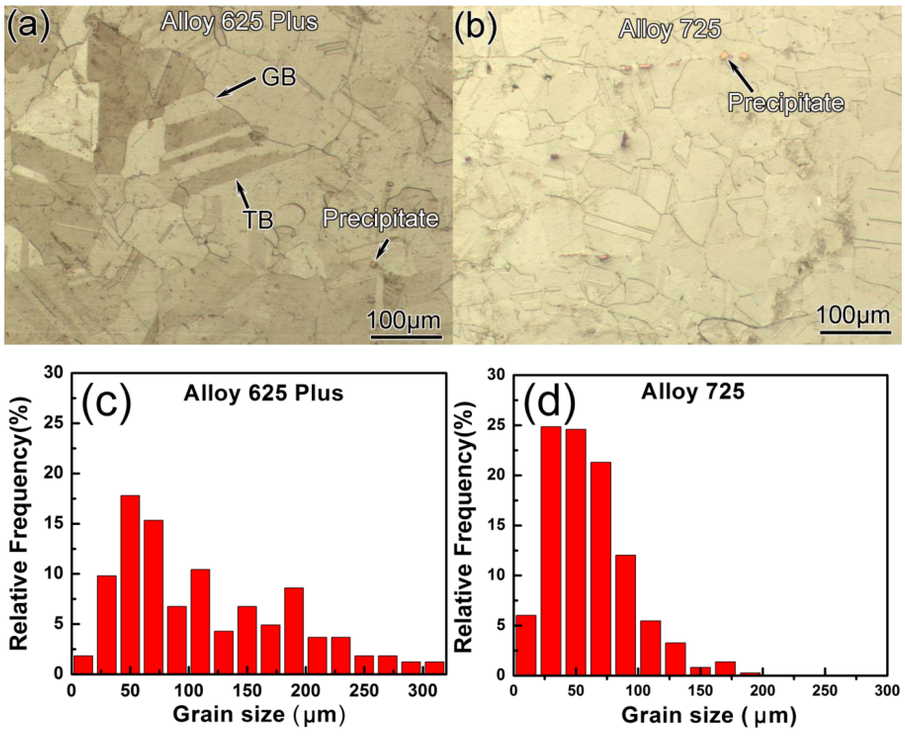

Figure 4-1: Optical images of the grain structures (a) and (b) and grain size distribution (c) and (d) of alloys 625Plus and 725 [Wang M. et al, 2015].

Figure 4-2 illustrates the typical EBSD map for alloy 625Plus and alloy 725. Twin boundaries were highlighted by red lines and regular high angle grain boundaries were in black. No significant texture was observed in either alloy. High angle grain boundaries were prevalent in both alloys as shown in Figure 3, in which more than 65% of the grain boundary length fraction was composed of Σ3 twin boundaries.

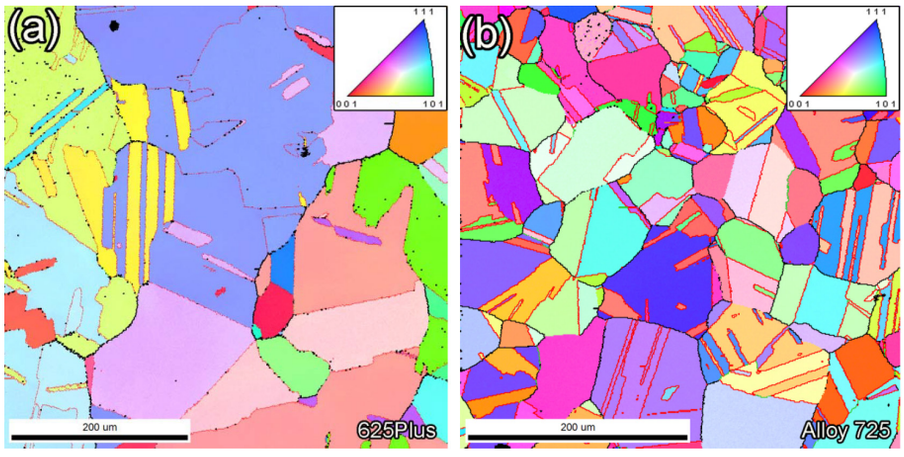

Figure 4-2: EBSD maps of (a) alloy 625Plus and (b) alloy 725. The grain color reflects their position in the inverse pole figure map. Note: Twin boundaries are highlighted by red lines; regular high angle grain boundaries are in black [Wang M. et al, 2015].

TEM images in Figure 4-3 revealed a substantial amount of precipitation in these alloys. The selected area diffraction pattern corresponded well to the γ″ phase which exhibits the following orientation relationships: (001)γ"//{001}γ, and [100]γ"//<100 >γ. There were three variants of the γ″ based on the symmetry of the crystal structure. The precipitates were disk shaped, and homogenously distributedwithin the matrix. The average particles size in alloy 625Plus was approximately 13 nm while the precipitates in alloy 725 were found to be coarser with an average size of approximately 18 nm.

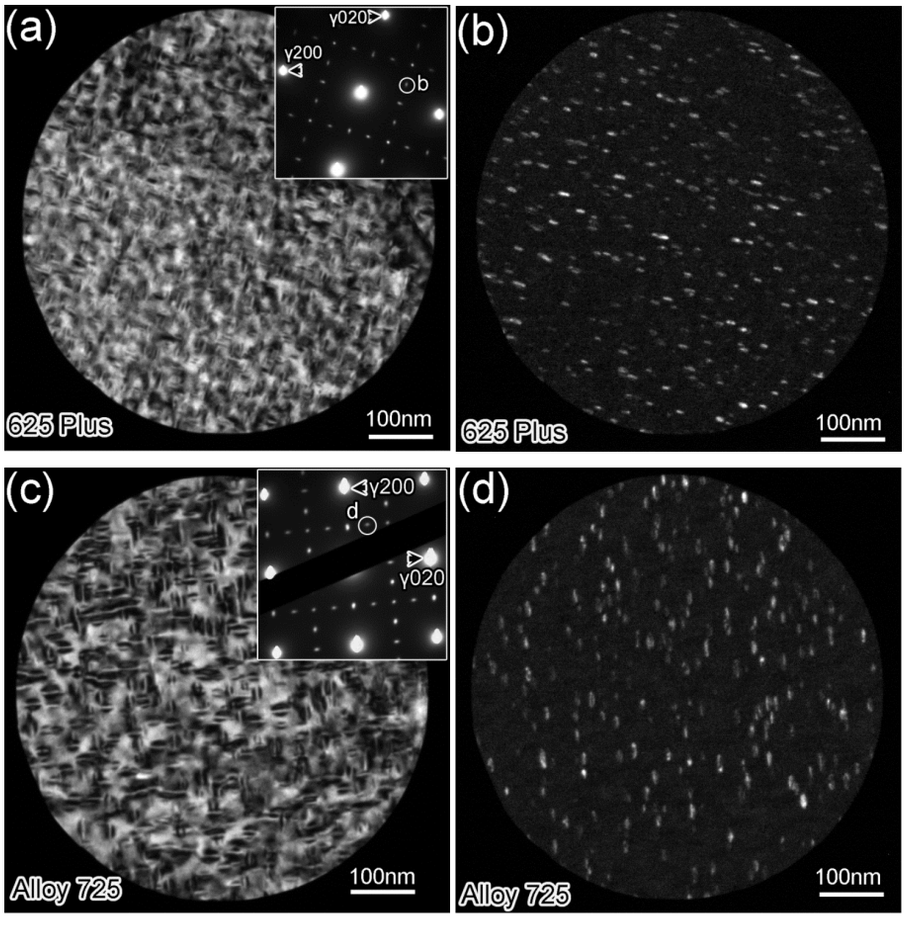

Figure 4-3: Bright field (a) and (c) and dark field (b) and (d) TEM images of non-irradiated alloys 625Plus and 725, respectively. Dark field images of γ″ precipitates with diffraction spots are labeled in the inserted selected area diffraction pattern in (a) and (c) [Wang M. et al, 2015].

The elements from EDX analysis agreed well with the chemical composition of the alloys studied as shown in Figure 4-4. EDX point analysis showed that the grain boundary segregation was insignificant in the as-received specimens in both alloys.

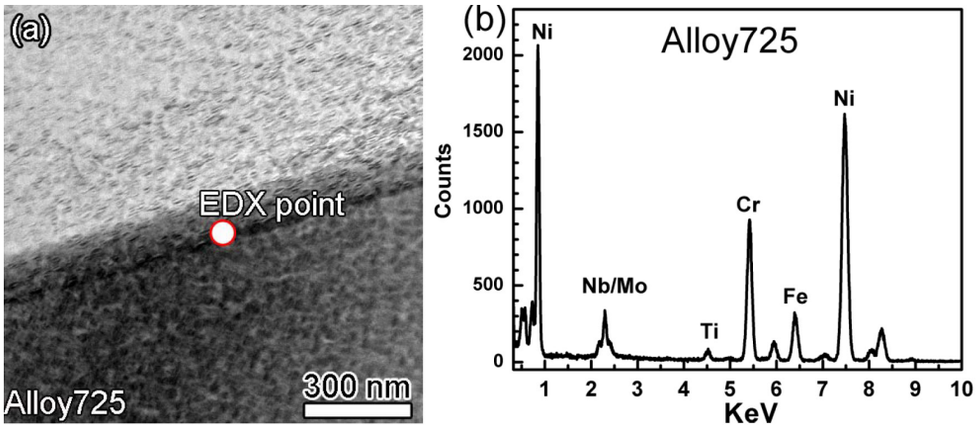

Figure 4-4: Bright field image (a) and EDX analysis (b) of a grain boundary in non-irradiated alloy 725 [Wang M. et al, 2015].

After irradiation, the γ" precipitates were reduced in size and number density which may be due to partial dissolution or amorphization. The particles in alloy 725 were less damaged and remained

5 PWR Ni alloy SCC tests

Measurement and understand of SCCI of Alloy 600 is of interest for understanding PWR nickel-base alloy component lifetimes, including components made from Alloy 690. Presented in the reference [Toloczko M.B. et al, 2015] are the latest data obtained at PNNL on SCCI for three MA Alloy 600 heats. Cold work effects on SCCI are the main focus of this paper because the time to initiation is reduced as the cold-work level (and strength) is increased. The materials were tested in their as-received (non-cold worked) condition and with up to 20% cold work applied either by cold tensile straining or cold rolling. SCCI detection was achieved by using in-situ continuous measurement by DCPD across the gauge section of the specimens. Details of the method and the DCPD response for different cold work levels are described. Crack lengths associated with initiation response are reviewed and compared to the concept of a critical stress intensity for SCC initiation. Results of ongoing complimentary SCC CGR tests on some of these same materials are also presented to help clarify the SCCI response.

SCC initiation was readily detected in the highly cold-worked specimens that exhibited a smooth but very rapid transition to a higher indicated apparent strain rate over a period of 10's of hours (recognizing that the higher strain rate is due to rapid crack growth rather than crack extension). An example is shown in Figure 5-1 for two 18% CTS specimens. More lightly cold-worked materials exhibited a more gradual transition to a higher indicated strain rate with the change taking place over 100's of hours as can be seen for a 7% CTS specimen in Figure 5-2. As-received (non-cold worked) materials, however, exhibited a distinctly different response that consisted of a step-change in observed strain as shown in Figure 5-3 for the service CRDM material (M3935). This step-change response is considered to be a tentative indication of SCC initiation and may be revised at a later date.

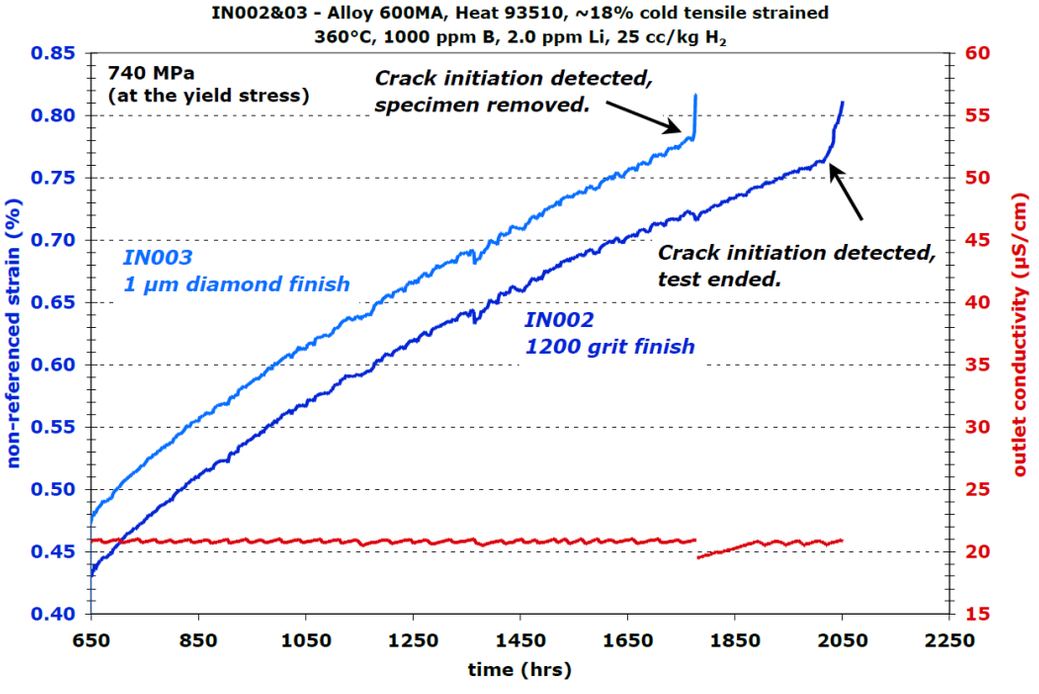

Figure 5-1: SCCI response of two ~18% CTS Alloy 600 plate specimens showing a smooth but sharp transition to a higher indicated strain rate [Toloczko M.B. et al, 2015].

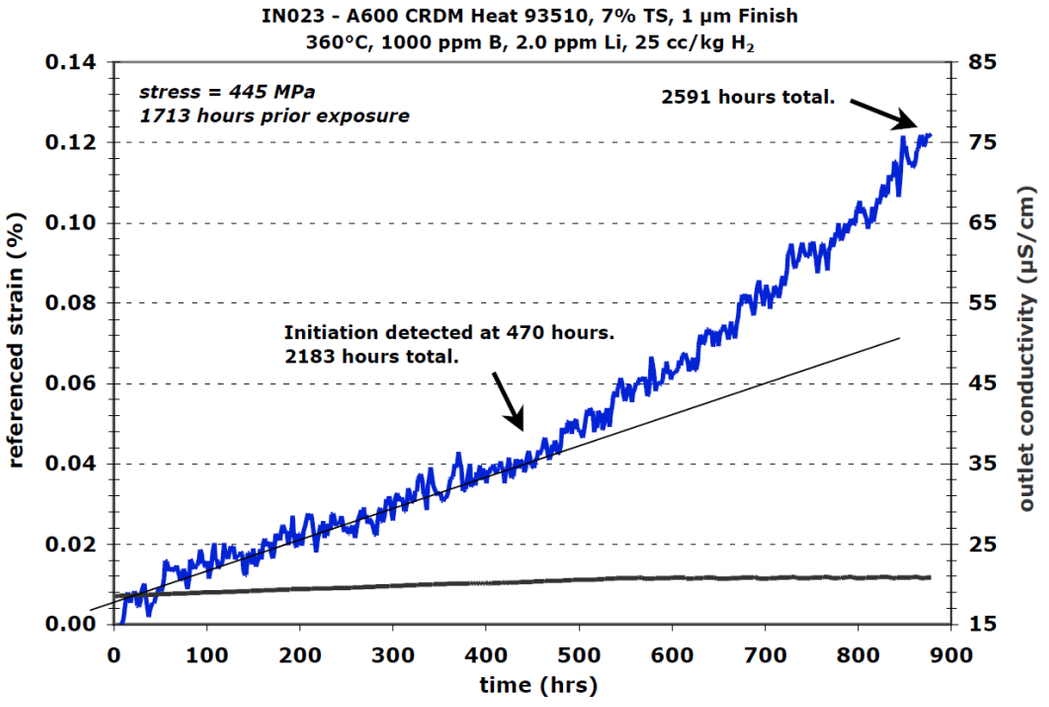

Figure 5-2: SCCI response for an ~7% CTS Alloy 600 CRDM specimen showing a sharp but continuous transition to a higher indicated strain rate [Toloczko M.B. et al, 2015].

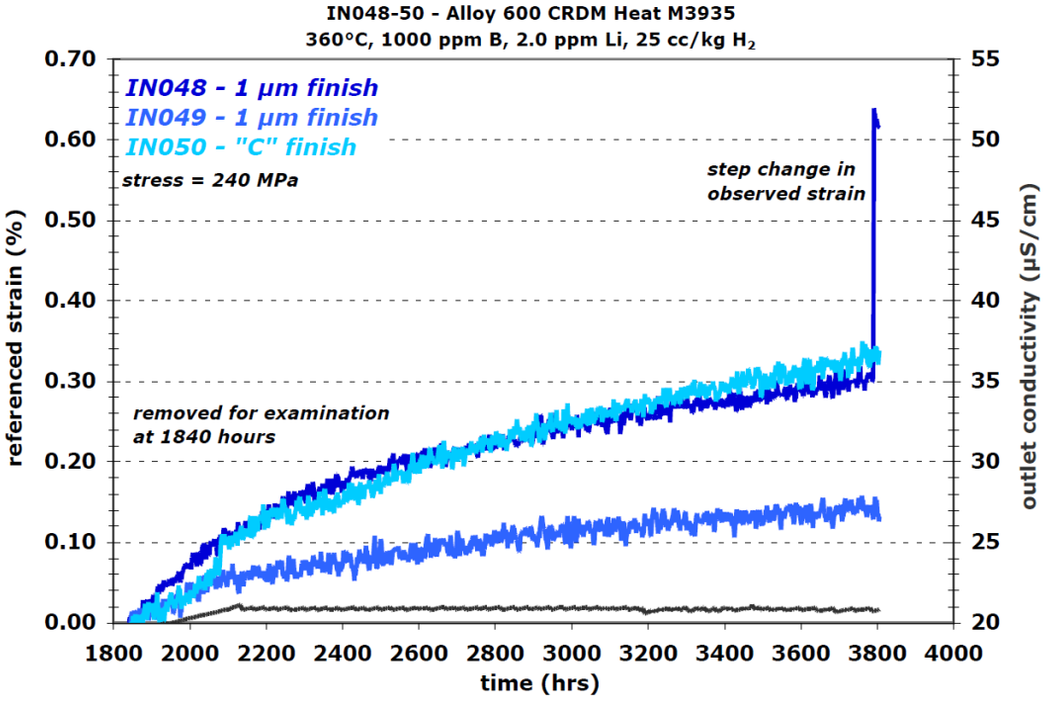

Figure 5-3: Observed response of non-cold worked alloy 600 CRDM specimens [Toloczko M.B. et al, 2015].

Cross section observations of cracks in initiated specimens have revealed a range of morphologies from IGA to well developed IGSCC cracks having depths exceeding 150 µm. Examples are shown in Figure 5-4 for the 18% CTS plate specimen with a polished surface (IN003). IGA observed at grain boundaries along the entire length of the gauge section had depths of no greater than 5 µm, such as in Figure 10a/b. Short cracks were also observed such as in Figure 10c/d. For the cold worked materials,

it appears that a few cracks eventually outpaced the others to produce a deep crack that caused the DCPD-indicated SCC initiation response. These dominant cracks were often readily identified on the surface such as shown in Figure 5-5 for the 8% CTS plate material (IN052). Whether more rapid propagation of one crack was always responsible for the DCPD initiation signal in the cold worked materials is currently under investigation. Smaller cracks were also readily identifiable on specimens with polished surfaces. Observations of small cracks on the surface of ground specimens were much more difficult. When viewed in cross-section, IGA was observed to uniformly progress through the nanocrystalline layer on ground surfaces as shown for example in Figure 5-6 and eventually reach grain boundaries below the ground surface.

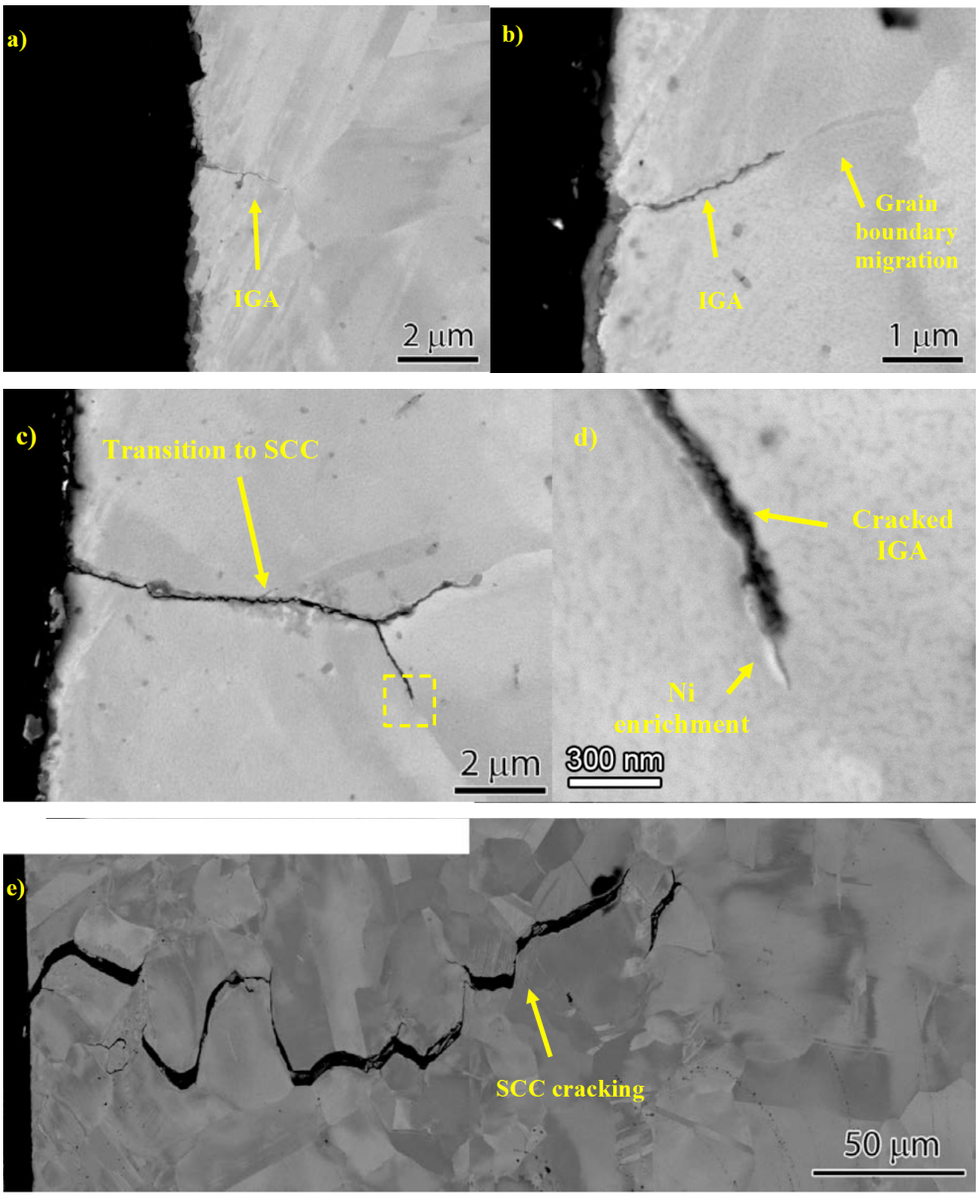

Figure 5-4: Range of SCC morphologies observed in cross section for the 18% CTS plate specimen (IN003) after SCC initiation [Toloczko M.B. et al, 2015].

6 PWR Ni alloy SCC precursors

Many studies have investigated IGSCC of Alloy 600. However, the role of each parameter on the IGSCC mechanism is not clearly understood and quantified. One of the main environmental parameters that influences IGSCC is the dissolved hydrogen content. It is known that the dissolved hydrogen content has an effect on crack initiation and propagation of Alloy 600 in PWR primary water. The crack growth rate reaches a maximum at hydrogen content close to the Ni/NiO transition where the oxide phase stability is not properly developed and affects IGSCC resistance.

IGSCC also depends on intergranular chromium carbides. Several studies have shown that IGSCC is slowed down by the presence of intergranular chromium carbides. One possible explanation is that chromium carbides are oxidized preferentially relative to the metal and the formation of Cr_2O_3 oxide becomes an obstacle to further oxide ingress at the grain boundary.

The goal of the reference [Giovanna Caballero Hinostroza J. et al, 2015] is to evaluate the propensity to intergranular oxidation of Alloy 600 in simulated primary water as a function of time, temperature and DH, assumed to be the main limiting parameters of the oxidation kinetics.

The effect of the dissolved hydrogen content and the role of the chromium carbides on the intergranular oxidation of Alloy 600 were investigated by SEM and TEM.

SEM observations of the oxidized specimen in the titanium loop showed that the dissolved hydrogen content influences the morphology of external layer formed on Alloy 600 after 100 h at 325°C: for 3 mL H_2/kgH_2O, the surface presents large crystallites (hundreds of nanometers) dispersed on the oxidized surface and needle-like oxide, whereas for 30 and 60 mL H_2/kgH_2O, small crystallites (size of 100 nm) are non-homogeneously distributed on the oxidized surface (Figure 6-1).

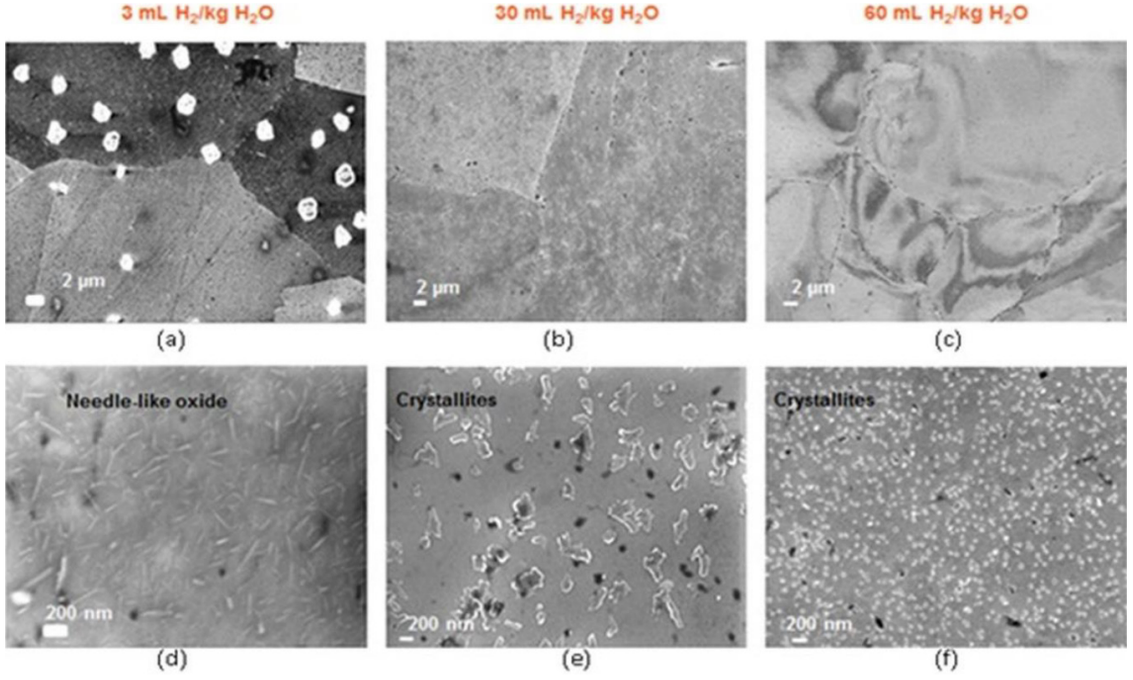

Figure 6-1: SEM observations of the oxide layers formed at 325°C in a rolled bar for different dissolved hydrogen contents: (a) 3 mL H_2/kgH_2O, (b) 30 mL H_2/kgH_2O, (c) 60 mL H_2/kgH_2O, (d) needle-like oxides formed on the surface at 3 mL H_2/kgH2O, (e) and (f) crystallites formed on the surface at 30 and 60 mL H_2/kgH_2O, respectively [Giovanna Caballero Hinostroza J. et al, 2015].

For oxidation tests of 1000h at 360°C performed in the stainless steel loop, crystallites observed at the surface present large crystallites with octahedral shapes (3 µm wide) and needle-like oxides (7 µm wide) homogeneously distributed (Figure 6-2).

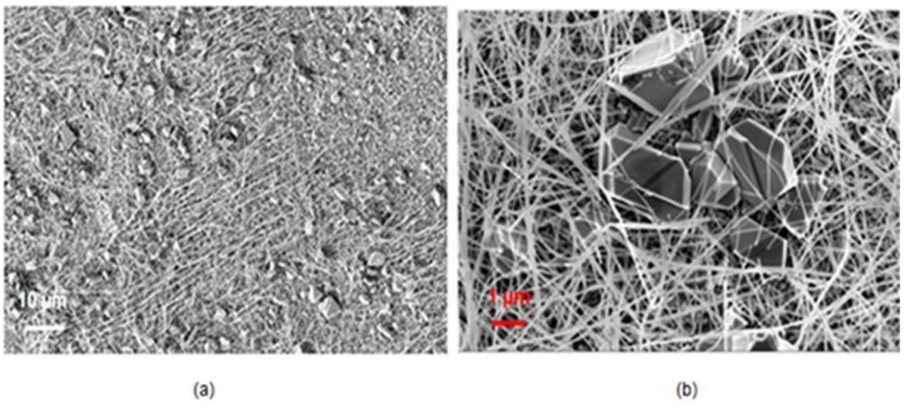

Figure 6-2: SEM observations of the oxide layer formed on the surface of the rolled plate at 360°C during 1000h using 20 mL H_2/kgH_2O [Giovanna Caballero Hinostroza J. et al, 2015].

For brief oxidation tests, TEM observations reveal a decrease of the thickness of the oxide film when the dissolved hydrogen content increases. Additionally, the increase of the dissolved hydrogen implies a slight decrease of the intergranular oxide penetration observed at the carbide/metal interface while the intergranular oxide penetration depth observed at grain boundaries without an emerging chromium carbide decreases when the dissolved hydrogen content increases (Figure 6-3). The results obtained in this work confirm the formation of Cr_2O_3 at the carbide/metal interface and that intergranular chromium carbides delay grain boundary oxidation.

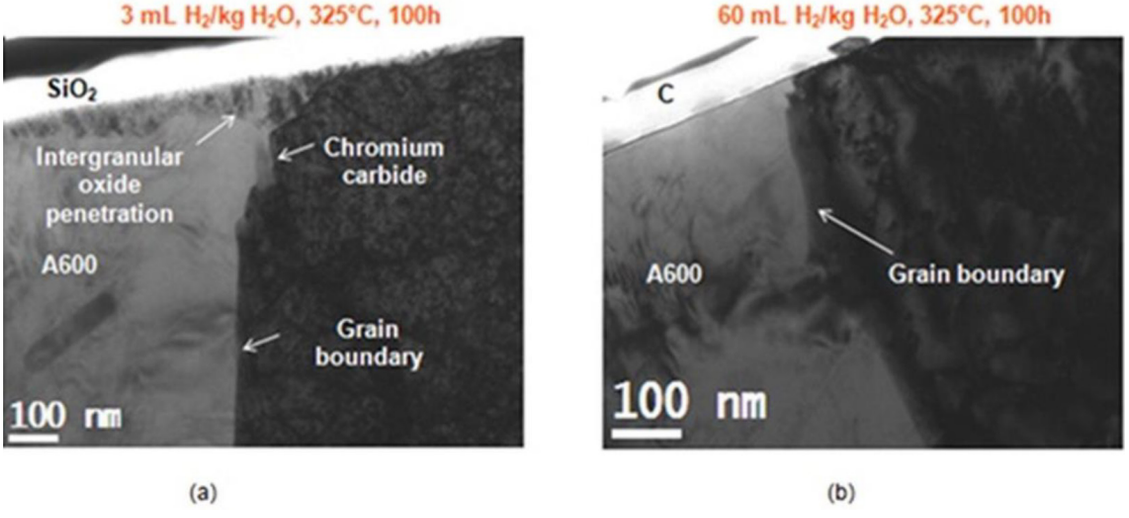

Figure 6-3: TEM bright-field images of grain boundaries without chromium carbide emerging at the surface (a) rolled bar specimen oxidized using 3 mL H_2/kgH_2O, (b) rolled bar specimen oxidized using 60mL H_2/kgH_2O [Giovanna Caballero Hinostroza J. et al, 2015].

Results about the role of grain boundaries character show that HAGBs are more susceptible to IGSCC. For oxidation test to 20 H_2/kgH_2O at 360°C during 1000h, of 45 grain boundaries inspected, the maximum intergranular oxide penetration occurs in a HAGBs (Figure 6-4). The most of intergranular oxide penetration in HAGBs is in the range of 1300-1400 nm, this represents 5% of grain boundaries inspected.

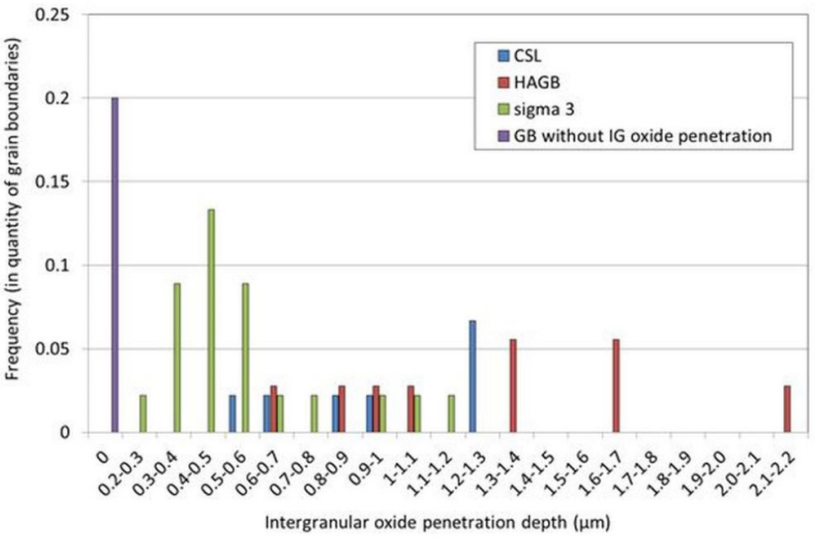

Figure 6-4: Intergranular oxide depth distribution as a function of thr grain boundary character [Giovanna Caballero Hinostroza J. et al, 2015].

Chromium carbides seem to be more reactive than the metal: a preferential oxidation at the alloy/carbide interfaces at the surface or in the bulk of the matrix is observed. In some case, oxidation bypasses the chromium carbide.

In order to improve the material SCC resistance thermally treated Alloy 600 was proposed as a possible replacement of 600MA. ln fact, thermally treated Alloy 600 has higher Intergranular Stress Corrosion Cracking resistance in PWR primary water environment than mill-annealed or solution-annealed Alloy 600. The main reason for this increased IGSCC resistance has been proven to be associated with the presence of grain boundary carbides, which are thought to delay crack initiation and decrease crack growth rate.

Considering that the mechanism responsible for IGSCC initiation is commonly accepted to be Preferential Intergranular Oxidation a semi-continuous network of intergranular carbides might delay or even stop intergranular oxidation. However, the mechanism by which intergranular carbides affect the oxidation and SCC initiation is still unclear and under debate and numerous possibility have been proposed in the past years. S. Bruemmer proposed that intergranular carbides promote crack blunting due to their effectiveness as dislocations sources, thus reducing crack growth rate and grain boundary sliding. Alternatively, carbides might create a more tortuous path for intergranular crack propagation and therefore reduce crack growth rate by mechanically interfering with crack propagation.

On the other hand, G. Was suggested that Intergranular Chromium carbides dissolution might result in the formation of a more stable and protective chromium-rich oxide at the crack tip hence reducing the intergranular oxidation rate and crack propagation. H. Dugdale also proposed that a denser and protective oxide is formed around intergranular carbides. Although several laboratories studied the intergranular carbides oxidation behaviour it is still not completely clear whether or not Cr carbides can be oxidized in PWR primary water.

More recently, G. Bertali confirmed the occurrence of solution-annealed Alloy 600 grain boundary migration during oxidation in high-temperature H_2-steam environment and suggested that this mechanism might play an important role in the IGSCC initiation phenomena. In the case of thermally-treated Alloy 600 the presence of such coarse intergranular carbides would make it difficult for a grain boundary to migrate, as these carbides would actually “pin” the grain boundaries.

The aim of the reference [Bertali G. et al, 2015] is to compare the initial stages of preferential intergranular oxidation for solution-annealed and thermally-treated Alloy 600 focusing mainly on the characterisation of carbides effect on localised grain boundary migration and grain boundary pinning carbides dissolution and grain boundary carbon content in solid solution.

Surface oxidation of solution-annealed and thermally-treated Alloy 600 in low pressure H_2-steam at 480°C was characterized by homogeneously distributed intragranular nodules (Figure 6-5) and a bulged/bowed grain boundary oxide structure (Figure 6-6).

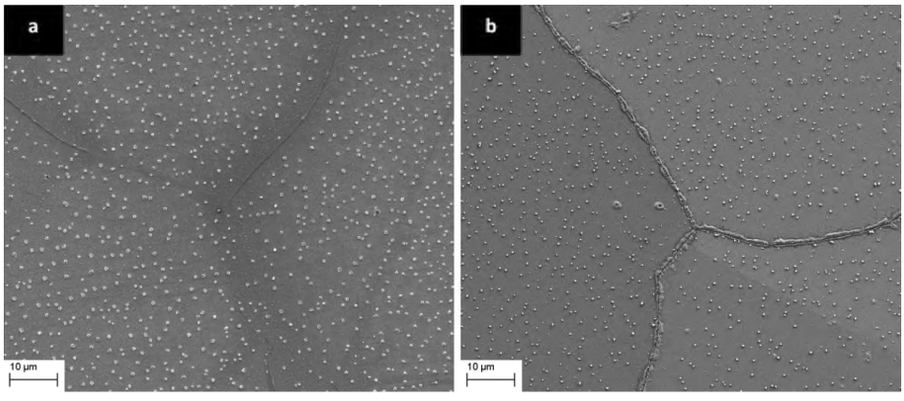

Figure 6-5: SEM SE images of the oxidized surface morphology of Alloy 600SA (a) and Alloy 600TT (b) specimen after H_2-steam exposure at 480°C [Bertali G. et al, 2015].

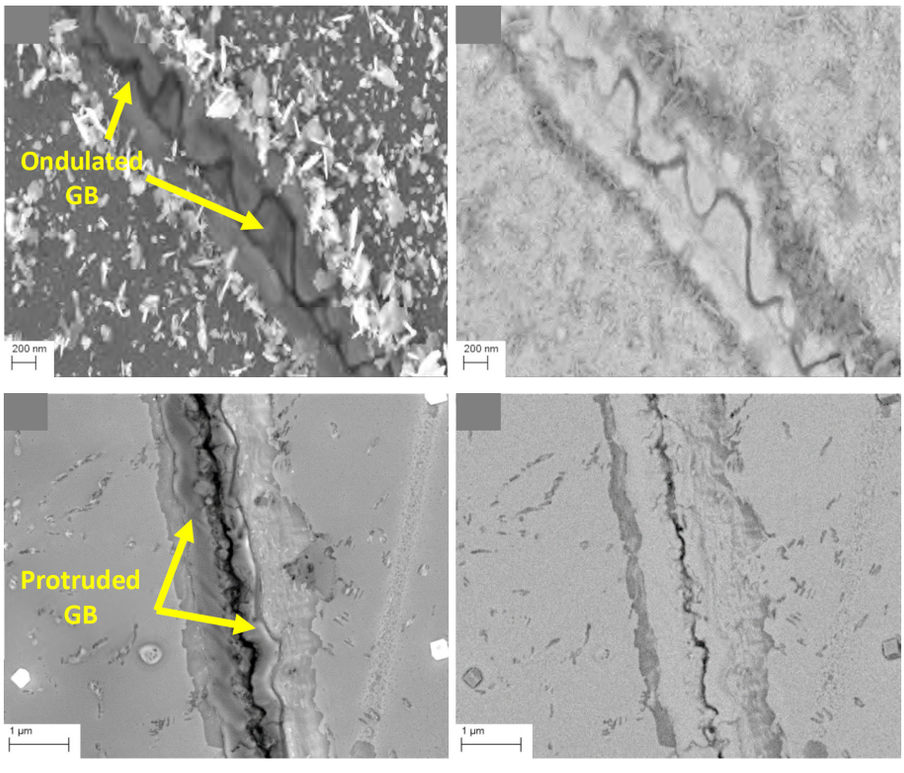

Figure 6-6: SE (left) and BSE (right) SEM images of Alloy 600SA (top) and Alloy 600TT (bottom) HAGB after the exposure showing the "bowed/bulged" grain boundary appearance [Bertali G. et al, 2015].

Alloy 600SA and Alloy 600TT specimens exposed in H_2-steam environment presented different preferential intergranular oxidation susceptibility with the solution-annealed material showing the highest susceptibility.

GB migration and the formation of the associated Cr- and Fe- depleted region occurred only on Alloy 600SA HAGB in the near-surface region, while Alloy 600TT appeared to be immune to this mechanism (Figure 6-7).

7 PWR Ni alloy SCC material factors

Alloy 690TT is an austenitic nickel-based alloy with annealing twins, precipitating almost exclusively Cr-rich $M_{23}C_6$ carbides and unavoidable large TiN particles. Solution annealing heat treatments dissolve most of the primary $M_{23}C_6$ carbides and low temperature heat treatments promote intergranular precipitation of secondary Cr-rich $M_{23}C_6$ carbides. Intergranular carbides are favored as they are widely considered to improve the intergranular SCC resistance of Alloy 690. However, Alloy 690 is not immune to IGSCC and crack propagation under primary PWR conditions is possible, once a crack is initiated. High cold work is reported to increase significantly the crack growth rate of PWSCC and to promote IGSCC of Alloy 690TT in PWR primary water. Especially, cold work creates localized deformation and strength increase, which are particularly high at the grain boundaries and promote intergranular cracking. Although typical Alloy 690 components are not highly cold-worked, high levels of strain can still be found in SG plugs, in the heat-affected zones of welds or after thermal ageing, raising concerns about the structural integrity of the components. In particular, thermal ageing of Alloy 690 promotes an ordering reaction, which leads to lattice contraction and localized plastic strains at GBs, as well as hardness increase and internal stresses. This exothermic reversible reaction is based on the formation of the ordered orthorhombic intermetallic Ni_2Cr phase below the composition-dependent critical temperature 550°C. It is a special concern, since Alloy 690 composition is close to the Ni_2Cr stoichiometry and favors the ordering reaction, especially for low Fe content. Two kinds of ordering are observed: short-range ordering is connected with the nearest neighbors of an atom, while long-range ordering is related to the formation of an ordered super-lattice. LRO forms following a nucleation and growth process and the kinetics are composition dependent and slow, typically requiring ageing times over 30,000 h. SRO, however, develops rapidly at the early stages of ageing and its kinetics are independent of the composition. A disordering reaction occurs above the critical temperature, although some levels of SRO can remain. In addition to changes in electrical and thermal characteristics, the main consequence of ordering is lattice contraction, with maximum effect at 475°C in Alloy 690. The contraction depends on the level of ordering. SRO causes contraction between 0.01 to 0.1% while LRO can lead to contractions up to 0.3% after 30,000 h. It leads to hardness increase, yield stress increase, a decrease of the elongation to fracture and a change of the fracture mode from ductile to brittle intergranular. Furthermore, ordering can promote heterogeneous planar slip, which produces widely spaced coarse slip steps and is a concern for environmentally assisted cracking resistance, as well as localized plastic strains in the vicinity of GBs, which are an internal factor contributing to localized corrosion and SCC. In fact, SRO is reported to cause contraction in the grains leading to tensile stress at the grain boundaries, and is therefore already seen by some as an internal mechanism promoting IG cracking of Alloy 600 at 360°C in primary PWR environment. LRO is unlikely to develop in a typical primary PWR environment. However, due to atomic movement at elevated temperatures, SRO is likely to occur readily during thermal ageing of Alloy 690 in modern PWRs, and is a concern for the SCC susceptibility, especially considering higher operating temperatures and longer service times. However, the parameters influencing the ordering reaction and especially the early stages of ordering are not well understood. The activation energy for Alloy 690 ordering reaction has been determined as 240 kJ/mol, and it generally ranges from the energy for vacancy migration in nickel (135 kJ/mol) to bulk diffusion of chromium in nickel (275 kJ/mol). Increasing iron content will effectively delay the initiation of LRO and carbon in solution appears to delay the establishment of SRO by trapping excess vacancies. Water-quenched materials show lower activation energy, which increases with furnace cooling and further with cold work. The explanation is that water-quenched materials retain a more disordered structure, from which SRO can quickly develop. On the contrary, slow furnace cooling from solution annealing temperature produces a rather advanced precipitation stage and some level of ordering, which makes further ordering reaction more difficult. In practice, however, furnace cooling effectively reduces the initiation time for ordering during ageing. Cold work after furnace cooling destroys the ordered structure. It makes the ordering reaction more difficult, and it increases the ordering initiation time back to the level of the water-quenched material. However, it also produces a large amount of lattice defects, which can promote SRO formation during re-heating and a few studies have pointed out that cold work promotes ordering. The aim of the reference [Mouginot R. et al, 2015] is to observe the influence of cold work and thermal treatment on the SRO of Alloy 690 aged for 3,000 and 10,000 h at the optimal ordering temperature of 475°C.

The four conditions of Alloy 690 of this study present very different microstructures that respond differently to the thermal ageing. With relatively short ageing times (3,000 and 10,000 h), all

conditions show evidence of SRO with lattice contraction in the range of 0.02-0.06% (Figure 7-1 left). For the SA and TT samples, which present more homogeneous structures, the lattice parameter and nanohardness measurements correlate well (Figure 7-1 right).

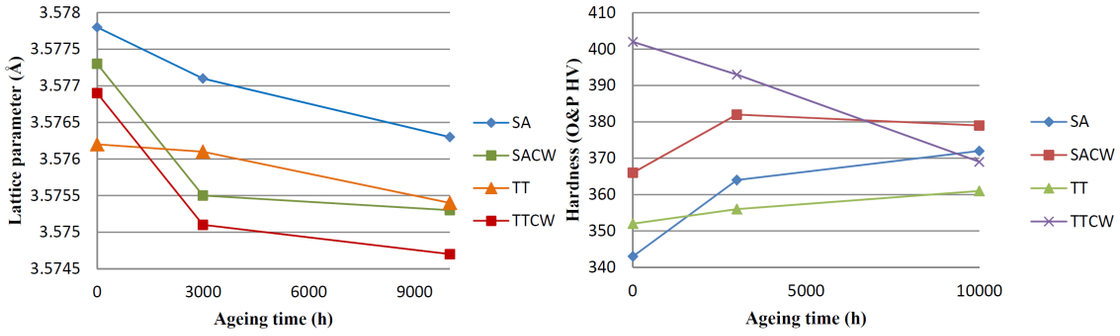

Figure 7-1: Left: lattice parameter before and after ageing at 475°C for 3,000 and 10,000 h for Alloy 690 SA, SACW, TT and TTCW conditions.
Right: nanohardness values before and after ageing at 475°C for 3,000 and 10,000 h for Alloy 690 SA, SA cold worked (SACW), TT and TT cold worked (TTCW) conditions [Mouginot R. et al, 2015].

Thermal treatment after solution annealing decreases the lattice parameter but reduces further lattice contraction during ageing and limits the hardness increase. The effect of ordering is seen in the SA condition through an increase of the local misorientation, which can be related to the strain level, while no apparent change is visible in the TT condition. Cold work nearly doubles the overall hardness of the material in both SA and TT conditions (Figure 7-2), but seems to limit the effect of ordering as the hardness increase is reduced in the SA cold worked and TT cold worked samples.

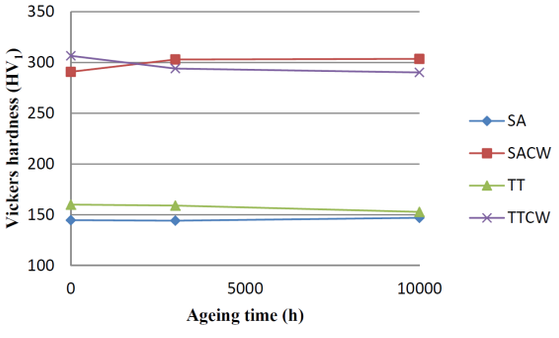

Figure 7-2: Microhardness values before and after ageing at 475°C for 3,000 and 10,000 h for Alloy 690 SA, SA cold worked (SACW), TT and TT cold worked (TTCW) conditions [Mouginot R. et al, 2015].

However, cold worked samples show the highest lattice contraction indicative of a higher level of ordering. In addition to SRO, thermal ageing precipitates IG carbides in the carbide-free SA and SA cold worked conditions. It coarsens the existing carbides in the TT and TT cold worked conditions, and produces large areas of cellular carbides growing from the grain boundaries (Figure 7-3).

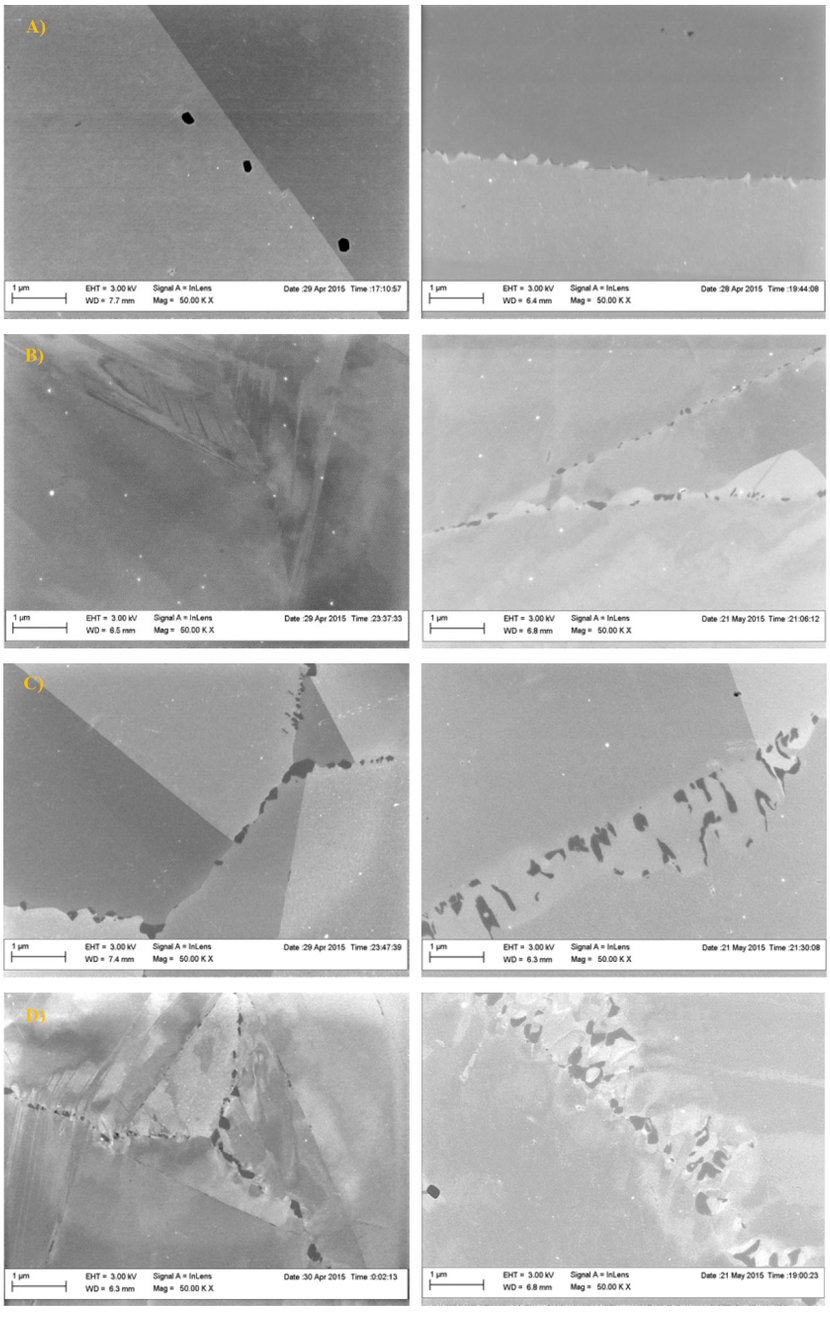

Figure 7-3: Carbide precipitation at GBs in the SA, SA cold worked (SACW), TT and TT cold worked (TTCW) conditions (A, B, C and D, respectively) before ageing (left) and after ageing at 475°C for 10,000 h (right) [Mouginot R. et al, 2015].

The study will be expanded further to consider the effect of carbide precipitation during ageing both on the strain localization and Cr depletion at GBs. In addition, the increase of internal strains observed in the SA condition is to be investigated further by observing the local misorientations as well as the nature of the XRD peaks obtained during the lattice parameter measurements. The aim of the research is to determine the influence of SRO on the localization of strain at the grain boundaries which, coupled to the intergranular precipitation, may prove to be an important mechanism for the IGSCC of Alloy 690 components of PWRs in the long term.

Many studies were conducted to determine the mechanism and establish numerical models of SCC. SCC is closely related and influenced by environment, microstructure and tensile stress, so studies were focused on those factors. Scott P. tested Alloy 600 in various environments to correlate intergranular SCC with oxidation phenomenon. He suggested that IGSCC is caused by internal oxidation, induced

8 PWR Stainless Steel SCC

Environmentally induced cracking, i.e. stress corrosion cracking, is an important issue for the nuclear industry and is therefore the focus of increasing research efforts within the nuclear community. Stainless steel alloys are often used for structural components in the primary circuit of fission reactors due to their outstanding performance in high-temperature, corrosive environments. Despite their generally excellent corrosion resistance, stainless steel alloys have proven to be susceptible to IGSCC after long service periods. Even though being the focus of many research efforts, the underlying SCC mechanisms are still poorly understood and there is no general model for the initiation and propagation of SCC yet.

The propagation of SCC in stainless steels is influenced by several inter-depending parameters such as water chemistry, temperature and matrix composition.

As of yet, many previous studies on SCC propagation have focused on gathering information about the formation of oxides and diffusion-based mechanisms at the crack front. In addition, changes in the local matrix composition and deformation in the matrix surrounding the crack have been studied using a variety of electron microscopy methods. They include scanning electron microscopy, auger electron spectroscopy, transmission electron microscopy as well as NanoSIMS. Despite these intense efforts, there is still limited information on the interaction of crystallographic features near the crack with the crack propagation process. Such information may include the misorientation of the grains on both sides of the crack, plastic deformation at the crack tip, ahead of it and at the crack flanks as well as the existence of slip, twinning and deformation bands.

One of the reasons for this deficit might be the absence of an appropriate technique that is capable of acquiring all these parameters within a reasonable time frame. The reference [Meisnar M. et al, 2015a] presents a novel study of crystallographic features in SCC specimens using a new method for high-resolution orientation mapping. With transmission Kikuchi diffraction, or sometimes also known as transmission-electron backscatter diffraction (t-EBSD), high-resolution crystallographic data can be easily and quickly (<1 hr) acquired. It shall be shown that it is possible that TKD may contribute to solving some remaining questions about the SCC crack propagation process.

Since the advent of the SEM in the 1960s, EBSD has been a popular tool for many materials scientist in order to obtain crystallographic data from their samples. Recent developments in the field of nanotechnology however, require resolutions up to a few nm, pushing the boundaries of conventional EBSD (with a resolution limit of ~50 nm, depending on the analyzed material).

Keller et al were the first to report of a new approach to perform high-resolution orientation mapping in 2012. It involves acquiring crystallographic data from an electron transparent TEM lamella with the SEM and a conventional EBSD detector, a method called transmission electron-backscatter diffraction, but also known as transmission Kikuchi diffraction. While there are no changes in the actual hardware used, the TKD setup differs from the EBSD setup in terms of specimen position and tilt angle towards the detector. In many systems, the EBSD software accounts for the altered geometry by adapting the Kikuchi pattern recognition algorithm. In specific, instead of the 70° tilt of the sample towards the camera in EBSD, TKD uses a near-horizontal (max. 10° tilt) mount of the TEM foil with respect to the incident electron beam. The TKD setup used in this study is shown in Figure 8-1.

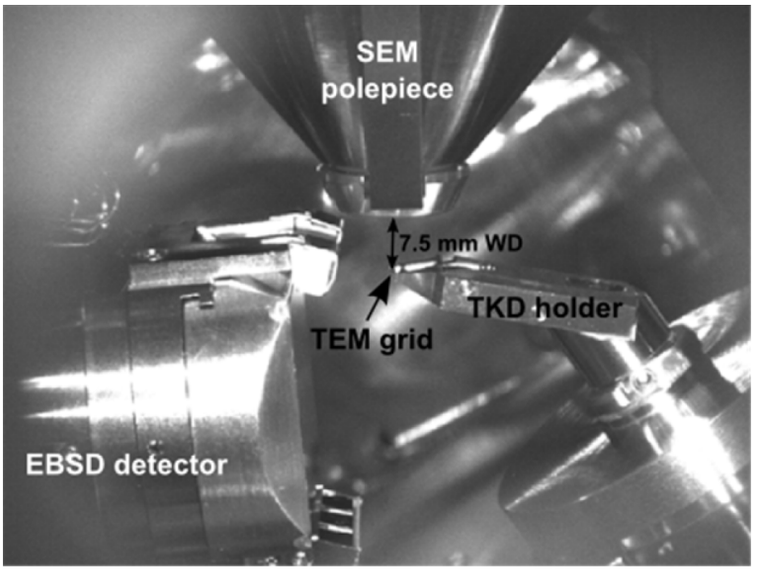

Figure 8-1: SEM chamber ready for TKD acquisition; top: electron pole piece, working distance (WD): 7.5 mm; right: TKD sample holder with TEM grid mounted, 10° tilt angle with respect to the horizontal; left: inserted EBSD detector (4° tilt from vertical) [Meisnar M. et al, 2015a].

The setup shown in Figure 8-1 was recommended by the manufacturer, Bruker. The EBSD detector has been inserted and is facing the sample (distance 12 mm) at a tilt angle of 4° with respect to the vertical. It is collecting incoming electrons from the bottom surface of the sample, which is tilted 10° upwards from the horizontal at a working distance of 7.5 mm. Due to this setup and the <100 nm thin TEM foil, the interaction volume is minimized in TKD. Monte Carlo simulations in Keller's publication have shown that in TKD, the lower specimen tilt of 10° (as opposed to 70° in EBSD) and the reduced thickness of the sample significantly decrease the interaction volume with the electron beam. Hence, the lateral resolution is considerably improved as reported by Keller et al and other researchers. In this study, good quality maps have been produced at sample thicknesses below 100 nm. Correspondingly, it has been reported that the thickness of the specimen has a strong effect on the achieved spatial resolution. Therefore, TEM sample preparation is important for the successful and reliable data acquisition via TKD.

This paper shows that TKD is a very quick and easy technique to gather high-resolution crystallographic information from TEM specimens, and is a useful complementary technique for studying the underlying mechanisms of SCC. With TKD, it is possible to acquire information such as the grain orientations around the SCC crack, the grain boundary misorientation and the plastic deformation in the sample (Figure 8-2).

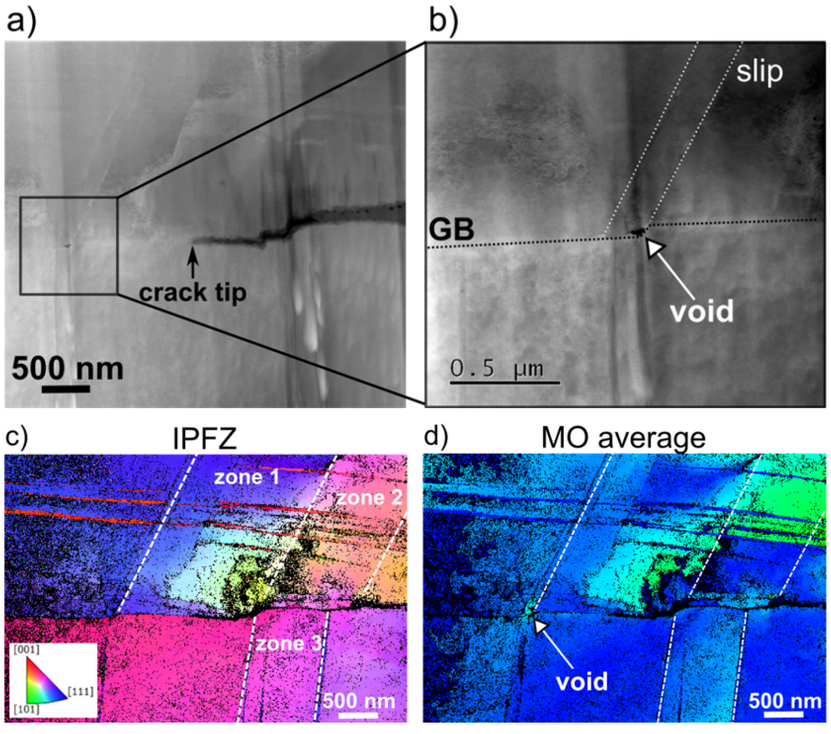

Figure 8-2: TEM and TKD measurements in SCC crack tip sample 3: a) HAADF image; b) close-up HAADF image of void located at GB (black dotted line), slip bands indicated (white dotted line); c) IPFZ map and legend, zones of slightly different crystallographic orientation indicated; d) average MO map indicating void and slip/deformation bands (colour temperature spectrum) [Meisnar M. et al, 2015a].

In particular, step-like crack propagation via TKD has been characterized. This cracking behaviour was previously studied with a range of analytical (high-resolution) techniques in order to investigate the crack morphology, oxide chemistry and the applicability of diffusion-based mechanisms responsible for the crack propagation. In this study however, mechanical response-based mechanisms were taken into account and, although being far from fully conclusive results, some suggestions towards the step-like SCC crack propagation were made. These are based on the conducted observations via TKD, a technique, which seems to have the potential to become significant for research of the underlying SCC mechanisms.

The process of SCC in PWR primary water strongly depends on the existence of a susceptible alloy microstructure, e.g. type 316 stainless steel, under stress and in contact with an aqueous environment. Likewise, SCC crack propagation depends on a number of parameters, such as test temperature, material composition and amount and type of pre-existing stress. In order to determine its overall influence, one variable needs to be studied individually and separate from all other factors. The reference [Meisnar M. et al, 2015b] discusses new insights into the influence of the test temperature on the propagation of SCC in SUS316 stainless steels. In general, it has been observed that the crack growth rate increases with increasing temperature between 250°C and 330°C. However, above ~330°C it seems that the CGRs are inhibited and there is a clear peak in the CGR between 320-340°C. Therefore, Arioka suggests that at least two rate-limiting processes must be involved in the SCC crack propagation process (for non-sensitized stainless steel 316), e.g. thermally activated diffusion or electrochemical reactions on the surface. Furthermore, the location of the peak in the CGR-T plot (shown below, Figure 8-3 blue line) depends on the sample's pre-existing cold-work level (the lower the cold-work level, the lower the temperature at which the peak occurs). Consequently, it appears that in addition to diffusion and electrochemical reactions, mechanical deformation within the material is another ratelimiting process that has to be considered as well.

9 PWR stainless steel SCC testing

The SCC of stainless steels has been an issue facing LWRs since 1965 when furnace sensitized components failed in the Dresden BWR. Numerous experimental efforts have been performed to characterize the SCC of stainless steels in LWRs in the last several decades and many of these efforts have been reported at each of the priors sixteen Environment Degradation of Materials conferences. The reference [Morton D.S. et al, 2015] further extends this stainless steel SCC research and specifically describes tests which were conducted to characterize SCC growth rates of cold worked 304SS as a function of temperature, coolant hydrogen concentration, sulfur content and sensitization.

Temperature effect testing has shown that cold worked non-sensitized 304SS SCC growth had an Arrhenius temperature functionality in deaerated water with crack growth rates increasing with elevated temperature. The measured thermal activation energy of 75 kJ/mol is consistent with results obtained by other researchers (Figure 9-1).

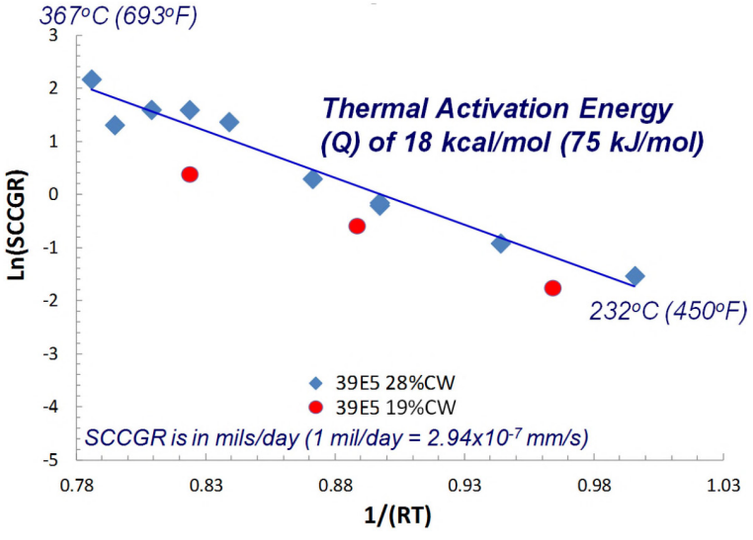

Figure 9-1: Effect of temperature on the SCCGR of 304SS in deaerated water; results show a thermal activation energy of 75 kJ/mol [Morton D.S. et al, 2015].

A departure from Arrhenius behavior (drop off in SCC propensity) may occur at elevated temperature (e.g., 338°C) for materials with moderate to low cold work levels (e.g., less than ~15% CW) due to some postulated crack tip relaxation phenomena (Figure 9-2).

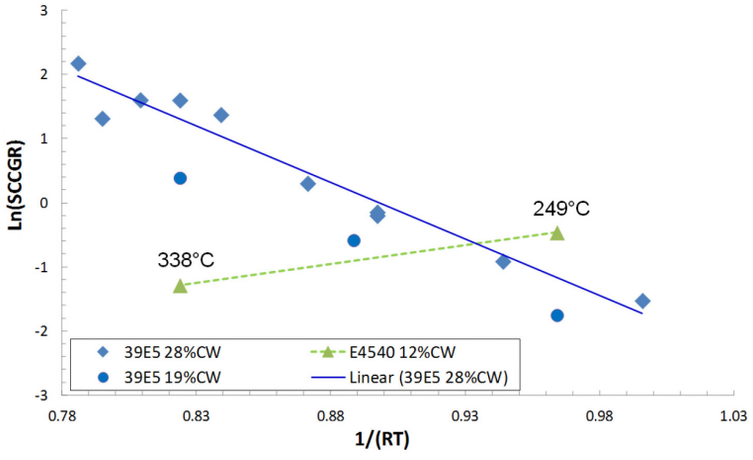

Figure 9-2: Effect of temperature on the SCCGR of CW 304SS in deaerated water; non-sensitized 12% CW heat E4540 shows a drop off in SCCGR at elevated temperature (338°C) [Morton D.S. et al, 2015].

304SS which has been sensitized prior to cold working showed a complex temperature functionality in deaerated water:

- Sensitization prior to cold working degrades the deaerated water SCCGR resistance of SS at 249°C;
- Sensitized and then cold worked materials, however, depart from Arrhenius temperature functionality more readily than non-sentized materials (i.e., drop off in SCC occurs at lower temperature and higher CW level than in non-sensitized material). Because of this greater propensity for Arrhenius temperature functionality departure sensitized 304SS SCCGRs are lower than non-sensitized growth rates at 338°C (Figure 9-3).

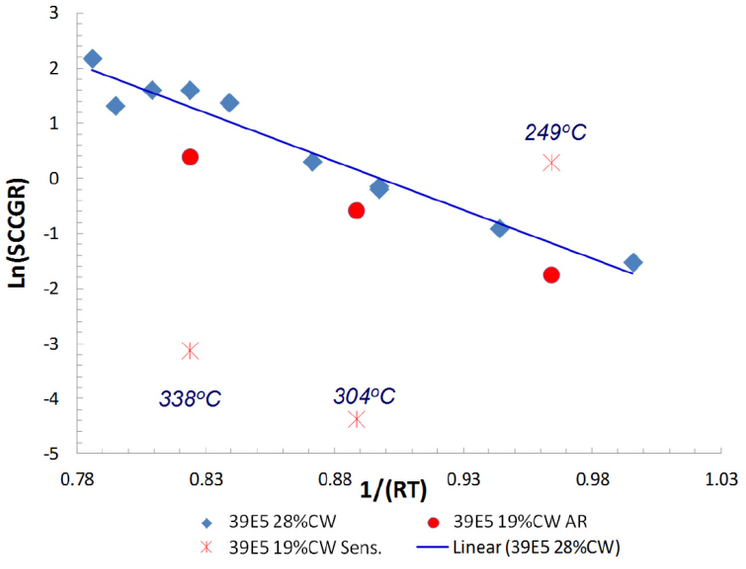

Figure 9-3: Effect of temperature and sensitization on the SCCGR of CW 304SS in deaerated water: non-sensitized 19 and 28% CW heat 39E5 data shows a thermal activation energy of ~18 kcal/mol. In contrast, sensitized 19% CW heat 39E5 data shows a drop off in SCCGR at temperatures above 249°C [Morton D.S. et al, 2015].

SCCGR testing of 304SS heats as a function of coolant hydrogen concentration showed no clear evidence of a coolant hydrogen dependence or any correlation related to the Ni/NiO phase transition (Figure 9-4). This is unlike Alloy 600 and other nickel based alloys which show a maximum in SCC susceptibility in proximity to the Ni/NiO phase transition.

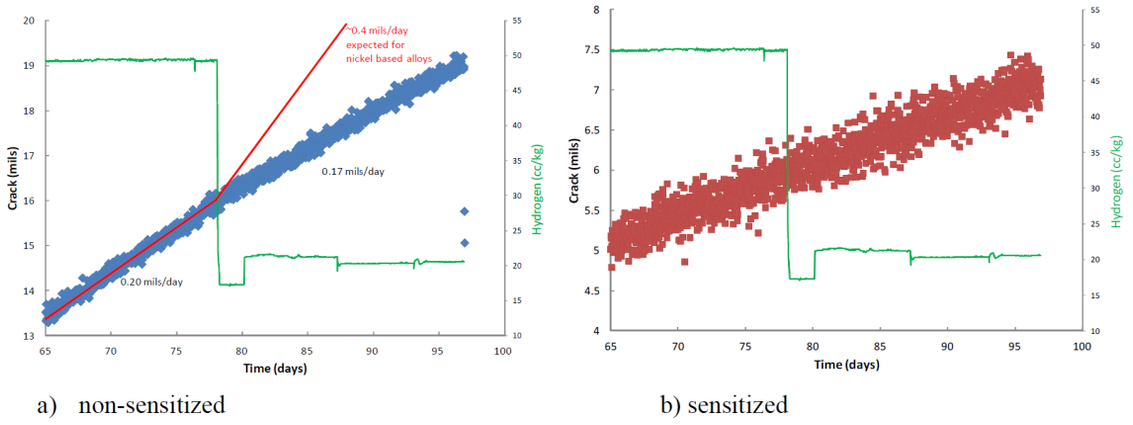

Figure 9-4: Effect of coolant hydrogen on the SCCGR of non-sensitized a) and sensitized b) CW 304SS heat E4540. Unlike nickel based alloys, SS SCCGR does not show a dependence upon coolant hydrogen concentration when changes are made in proximity of the Ni/NiO phase transition. The expected nickel based alloy coolant hydrogen SCCGR response to the 50 to 20 cc/kg hydrogen concentration change is depicted in red (12% cold worked heat E4540 at 338°C) [Morton D.S. et al, 2015].

Material and coolant sulfur addition improved the SCCGR performance of cold worked 304SS in deaerated water (Figure 9-5). AEM analysis of high sulfur level test materials and test specimens exposed to 200 ppb sulfate showed an enrichment of sulfur at the metal/metal oxide interface. In contrast, no sulphur incorporation was observed within low sulfur heat crack tip oxides.

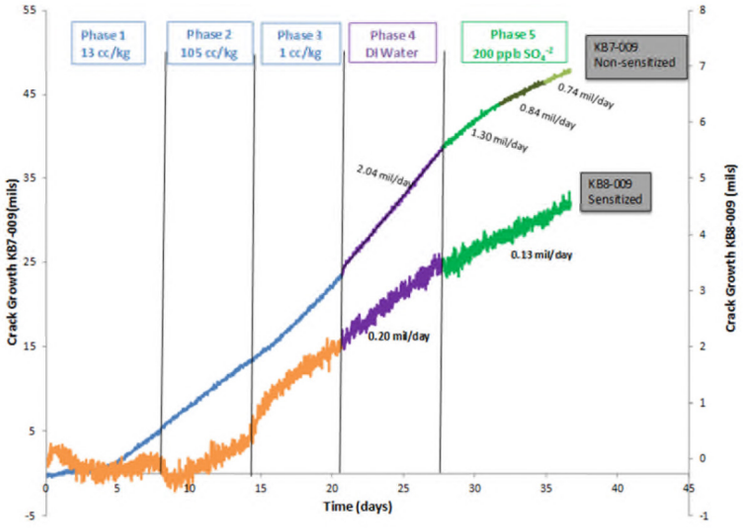

Figure 9-5: Effect of coolant sulfate addition on the SCCGR of CW SS in 338°C deaerated water. The results show that the addition of 200 ppb sulfate as H_2SO_4 mitigated the SCCGR of both the sensitized and non-sensitized 12% CW heat 39E5 specimens [Morton D.S. et al, 2015].

Austenitic stainless steel was found to be susceptible to SCC by both laboratory experiments and field experiences. The SCC is typically associated with off-normal water chemistry conditions and cold working of the steel. Dissolved oxygen and harmful anions such as Cl and SO_4^{2-}, promote the occurrence of SCC. In normal water chemistry with dissolved hydrogen at low electrochemical potential conditions, CW is a key factor leading to SCC of the steel. The promotion of SCC by CW is attributed to the damage of grain boundaries and the increase in hardness and yield stress. Studies have revealed that in the heat affected zone of a weld joint, residual strain as a result of weld shrinkage could increase the yield stress, lead to heterogeneous distribution of strain, and therefore, promote SCC as occurs in CW material. The SCC behavior in the fusion boundary region of a weld joint was also investigated. The investigation concluded that the FB could be a barrier for SCC propagation. For

10 PWR SCC Modeling

The purpose of the reference [Arioka K. et al, 2015] is to provide basis for quantitatively predicting the occurrence of SCC of cold worked Alloy TT690 in light water reactors; the ultimate aim of this work is to predict performance to at least 60 to 80 years. In particular, this work is focused on quantitative prediction of the initiation segment of SCC with Alloy TT690. Conditions considered here are: cold work, grain boundaries structures, temperatures in the range of 320°C to 465°C, and long testing times more than 20,000 h. Basically, the specimens used are of the “blunt notch” type. In addition, special designed compact tension type specimen with a shallow pre-crack of one grain size depth are used to examine the transition of SCC segments from initiation to growth. Crack initiation behaviors of Alloy MA600 was also studied in PWR water and in air to consider the similarities and dissimilarities with Allov TT690.

The aim here is to focus on atomic processes which can be quantified in terms of coalescence of vacancies which produce cavities at grain boundaries.

The work here is in the category of proactive research where the aim is to predict processes before major damage occurs. As Staehle and Gorman have pointed out, such proactive research is crucial to identifuing problems before they occur in operating plants. Staehle describes such "proactivity" as “serving to prepare for, intervene in, or control an expected occurrence or situation, especially, a negative one or a difficult one”.

To assess degradation caused by SCC after long times of operation in light water reactors, detailed knowledge of both initiation and growth over long times are necessary. Further, it is particularly difficult to predict long term initiation from conventional short terms accelerated experimental studies. Therefore, it is necessary to understand atomic identities and processes. Also. It is necessary to understand the underlined process by reasonably long term testing under simulated conditions in operating LWR's considering the possible change in material during long term operation beyond 60 years.

The specific purpose of the present research is to identify and quantify the underlying atomic processes of initiation that provide bases for predicting the occunence of SCC during very long term incubation periods in LWR environments. The main reasons for undertaking this study is related to the important applications of steam generator tubing and structural materials such as control rod drives as well as other components.

The excellent perfonnance of Alloy TT690 is now widely recognized in primary systems in operating PWRs. However, some researchers have reported that intergranular SCC growth occurs in Alloy TT690 in PWR primary water if the materials have been cold worked even though measured SCC growth rates were slower than mill annealed Alloy 600. However, there is little research on the SCC initiation precursors of these alloys in PWR environments that provides adequate information for predicting long term reliability.

Accordingly, Arioka examined the crack initiation and growth in cold-worked carbon steels in a hydrogenated pure water and in air to assess the reliability of piping during its life in LWRs. The clear evidence of cavity formation resulting from vacancy clusters was recognized at grain boundaries before crack initiation and growth both in the water and air. The cavities were assumed to weaken the grain boundary bonding strength. Arioka also reported that cavities, which resulted from vacancy coalescence, were formed more rapidly when material was exposed to water rather than to air environments at the same temperature. The main cause of this more rapid cavity formation is probably due to the effect of super abundant vacancies that result from absorbed hydrogen generated from the exposure to high temperature water. Regarding the mechanism of IGSCC of cold-worked materials in high temperature water, Arioka reported, on the basis of creep studies and crack tip analyses, that diffusion of vacancies, which were driven by stress gradients near grain boundaries, produced cavities.

Based on these results, cavities, especially in cold worked materials, might form prior to crack initiation especially in the case of a long term operation at LWR operating temperatures. Further, Arioka reported that it is necessary to take into account the possible change in bonding strength at grain boundaries caused by cavity formation during long term operations. Further, Bruemmer reported recently that SCC initiation occurred in CW TT690 at 360°C in PWR primary water under dynamic

loading conditions, and they also recognized cavities ahead of SCC-tip. However, there are no data on the initiation segment of Alloy TT690 in PWR water under static constant load condition. Furthermore, there are no mechanistic studies on the initiation segment of Alloy TT 690 in PWR environments; therefore, initiation of SCC, caused by the formation of cavities in cold worked Alloy TT 690 is a focus of this study.

lntergranular SCC advance occurred in 20% CW TT 690 from a shallow fatigue pre-crack of about one grain size depth after 20,653 h in 360°C PWR primary water. Also, intergranular cracking without oxide was observed ahead of the SCC-tip (Figure 10-1). The fracture surface was almost completely covered by cavities (Figure 10-2). This suggests that the observed intergranular cracking is formed as a crack embryo before SCC advance in 360°C PWR primary water during 20,653 h.

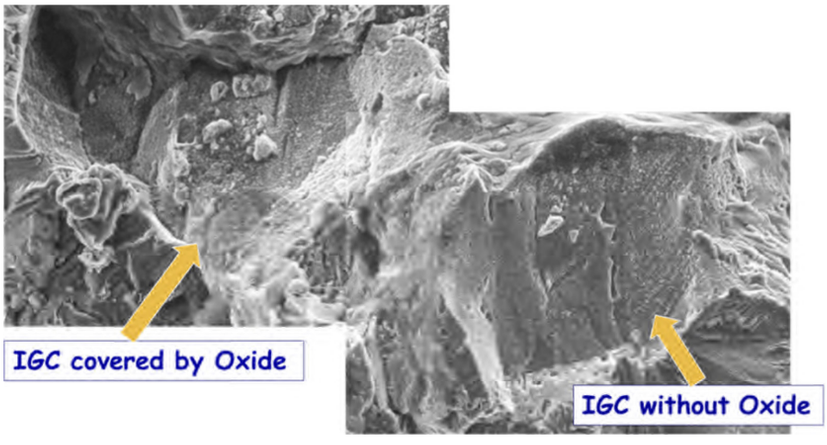

Figure 10-1: Fracture surface of 20% CW TT690 after test in PWR primary water (360°C for 20,653 h, pre-crack depth about 0.1 mm, K = 24 MPa.m$^{1/2}$) [Arioka K. et al, 2015].

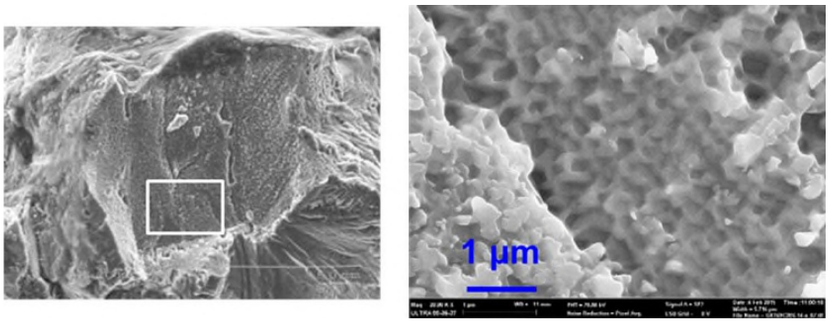

Figure 10-2: Fracture surface of 20% CW TT690 after test in PWR primary water (360°C for 20,653 h, pre-crack depth about 0.1 mm, K = 24 MPa.m$^{1/2}$) [Arioka K. et al, 2015].

A high density of cavities is observed at intergranular locations in 20% CW TT690 ahead of SCC tip after 20,653 h in 360°C PWR primary water (Figure 10-3). Cavities appear to be nucleated near carbides by the condensation of vacancies. This result suggests that diffusion of vacancies, which are driven by stress gradients, occurs during the incubation period even in 360°C PWR water. Eventually, the bonding strength of grain boundaries seem to weaken before cracks initiate.

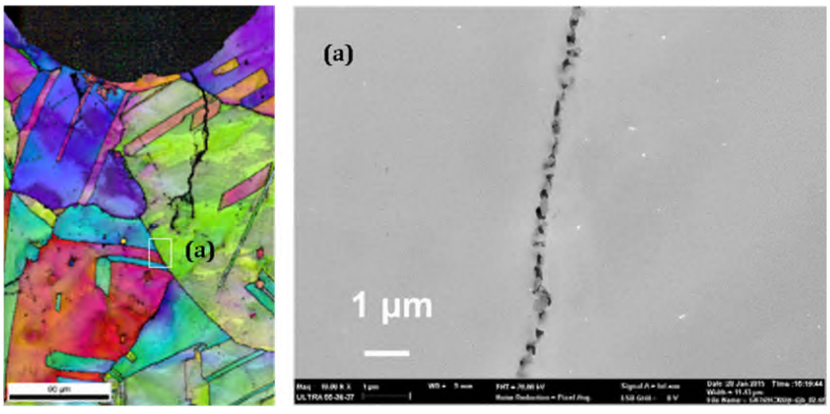

Figure 10-3: Cross sectional view of 20% CW TT690 after test in PWR primary water (360°C for 20,653 h, pre-crack depth about 0.1 mm, K = 24 MPa.m$^{1/2}$) [Arioka K. et al, 2015].

Clear evidence of cavities formation of 20% CW TT690 after 20,653 h in 360°C PWR primary water suggests that the rates of cavity formation might be enhanced in 360°C PWR primary water although further comprehensive studies are crucial (Figure 10-4).

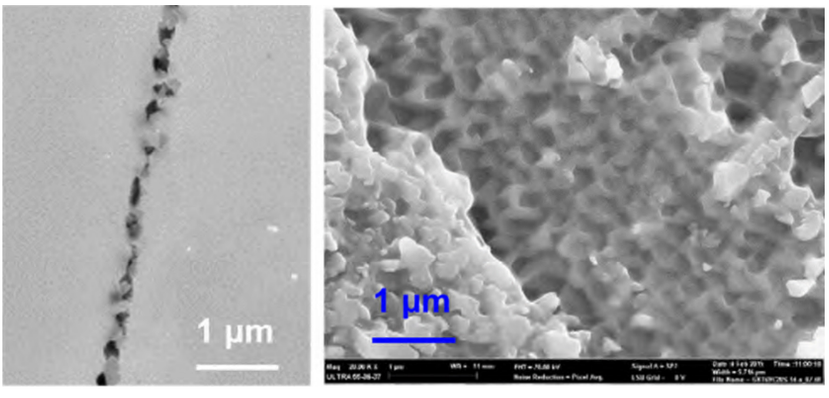

Figure 10-4: Comparison between fracture surface and cross sectional view after test in PWR primary water (20 % CW TT690, 360°C for 20,653 h, pre-crack depth about 0.1 mm, K = 24 MPa.m$^{1/2}$) [Arioka K. et al, 2015].

IGSCC of 20% CW MA600 seems to initiate mainly by localized intergranular corrosion from the surface in PWR primary water (Figure 10-5). The transition of SCC segments from initiation to growth seems to occur above about 0.2 to 0.3 mm depth of intergranular cracking at high stresses.

11 PWR stainless steel corrosion fatigue

Knowledge of the formation of oxide structures in the crack tip enclave of a growing fatigue crack is critical for developing a comprehensive understanding of the fundamental mechanisms responsible for environmentally enhanced and retarded crack growth observed in some heats of Type 304/304L stainless steel during corrosion fatigue testing in deaerated pressurized water at elevated temperatures. Crack growth during these tests is believed to be related to a combination of corrosion and mechanical processes. Depending on CF test conditions, such as temperature, hold time, or rise time, one of these processes may dominate and lead to instances where fatigue crack growth is enhanced or retarded. As will be described, identification of the similarities and difference in the microstructure and chemistry of the oxides formed during corrosion fatigue are a critical factor in determining the mechanism that is operating. This information can be used to guide the development of appropriate models for predicting crack growth behavior.

Analysis of CF test data and surface fractography led W.J. Mills to propose that environmentally enhanced crack growth observed in Type 304/304L SS during CF testing was attributable to enhanced planar slip resulting from the uptake of hydrogen, generated during the corrosion process, into the heavily strained region immediately ahead of the crack tip. Enhanced crack growth was expected to be prevalent at short rise times, short hold times, and low stress ratios during cyclic loading. Mills attributed environmentally retarded crack growth to an injected vacancy enhanced creep mechanism that operated during both long rise and hold times and at low values of ΔK. Under the IVEC process, vacancies generated in response to the corrosion process would diffuse to dislocations formed ahead ofthe crack tip and induce a climb process that would relax stresses at the crack tip and subsequently retard crack growth. Fractographic evidence to support the IVEC mechanism is in the form of the lack of cleavage-like facets on the fracture surface which is indicative of wavy slip (dislocation slip on multiple crystallographic slip planes).

Experimental work to directly test the validity of the IVEC mechanism by the direct observation of vacancies would be extremely challenging for several reasons. First, the direct observation of vacancies within the microstructure ahead of the crack tip would require high resolution electron microscopy and the preparation of very thin samples from the region immediately ahead of the crack tip using the focused ion beam technique. While both the FIB and HREM techniques are readily available, specimens would need to be very thin (on the order of a few atomic planes) in order to directly identify the presence of vacancies in high resolution images. High quality specimens of this type would be very difficult to produce using the FIB technique. Second, large numbers of vacancies in a material tend to cluster together and coalesce into dislocation loops. While observation of dislocation loops might provide indirect evidence of the presence of vacancies, ion damage imparted by the FIB ion beam during specimen preparation can also lead to the formation of dislocation loop structures. Thus, it would not be clear in the analysis if any observed dislocation loops were formed from coalescence of vacancy clusters or if the loops were a result of ion damage during specimen preparation. Third, individual vacancies are formed during interactions that occur between dislocations that are mobile on different slip planes. Thus, even with direct observation of vacancies in the region ahead of a propagating crack, there will be uncertainty in the analysis as to whether the vacancy was generated as a result of corrosion or from dislocation-dislocation interactions that occur in the high stress region immediately ahead of the propagating crack. As a consequence, experimental observations to test the IVEC mechanism will have to rely on indirect evidence of vacancy mechanisms. One potential characterization path for this is to examine the oxide structures formed by corrosion during testing to determine which elemental species contribute to potential vacancy mechanisms. These observations can then provide input for the development of models for predicting how vacancy injection mechanisms may influence crack growth rates.

The majority of observations of oxides formed in austenitic SS under nuclear plant operating environments reported in the open literature are from the study of stress corrosion cracking where the corrosion process strongly influences the cracking behavior of SS under constant load. A summary of the types of oxides was presented in a recent paper. In general, a two-layer oxide structure consisting of an outer oxide of magnetite (Fe_3O_4), with some incorporated Cr and Ni, and an inner Cr-rich spinel (typically a non-stoichiometric form of $(Fe, Cr)_2O_3$ or $FeCr_2O_4$) is most often observed in austenitic SS exposed to a simulated primary water environment.

A number of studies have also been performed to understand the oxide formation in a variety of water chemistries. These studies tend to focus on the use of coupons exposed to high temperature water chemistries in an autoclave. Based on the work of Stellwag, the outer (surface) oxide layer is thought to form due to Fe diffusion from the base metal and from dissolved Fe ions present in the water from the autoclave while the inner oxide layer is believed to form in parallel to the outer layer by a solid state growth process. Imperfections in the microstructure, due to grain boundaries, dislocation structures, etc., likely increase mass transport due to increased movement of ions along these structures. Recent work by Kuang et al., has proposed a different mechanism to describe the formation of both the outer and inner oxide layers. In the proposed model for oxide growth in this work, based on experimental observations of surface oxides formed on coupons of 304 SS exposed to water with dissolved oxygen content (3 ppm) at 290°C for times ranging from 1 hour to 1000 hours, both magnetite (Fe_3O_4) and hematite (Fe_2O_3) are observed in the outer oxide layer along with a thin inner (spinel) oxide. Based on these observations, and different from that proposed by Stellwag, it was proposed by Kuang et al., that a solid state reaction initiates the growth of the observed hematite (Fe_2O_3) which subsequently grows by a precipitation process driven by metallic ions present in the water environment of the autoclave. It should be noted that direct comparison of the oxides formed on coupons may be difficult due to differences in water chemistry in the crack tip enclave compared to that in the autoclave environment.

Composition of the inner oxide formed in primary water environments is found to vary due to the temperature and water chemistry (particularly the pH, conductivity, and oxygen content) under which the oxide forms. While the inner oxide retains a spinel crystal structure, the ratio of Fe and Cr may be nonstoichiometric and small amounts of Ni may be incorporated into the corrosion product. In some cases, elevated levels of Ni are observed at the interface between the inner oxide and the base metal. This is believed to result from the corrosion process; because Ni is more noble than Fe or Cr, it is rejected from the growing oxide layer and tends to be concentrated at the oxide/metal interface.

Formation of the oxides during corrosion fatigue appears to be a less studied topic. No open literature papers were found that focused on oxide structures developed during corrosion fatigue testing of austenitic SS in simulated primary water conditions. In comparison to the oxide structures formed during static (or nearly static) load imposed during SCC testing, oxide formation in fatigue testing, and its influence on the mechanisms responsible for crack growth, may differ depending on the test conditions (e.g., rise time, hold time, ΔK, etc.) used during corrosion fatigue testing. As mentioned earlier, crack growth during corrosion fatigue is likely influenced by a combination of corrosion and mechanical processes. For example, during test conditions promoting enhanced crack growth, the mechanical response may contribute more to the overall crack growth than the corrosion process.

In the reference [Miller B.D. and Paraventi D.J., 2015], a FIB system was used to extract specimens from the fracture surface of compact tension specimens and from the crack tip enclave from two different heats of Type 304/304L SS that had undergone corrosion fatigue testing that promoted enhanced and retarded crack growth. These two heats of material, A16830 and D2739, exhibited markedly different fracture surfaces and fatigue crack growth behavior. The former exhibited a heavy, thick corrosion product which obscured the fine structure of the fracture surface while the latter possessed a relatively light corrosion product. Analytical electron microscopy was used to characterize the corrosion product and the interface between the oxide and the base metal. The goal of this work was to identify similarities and differences between the oxides and the oxide/metal interfaces to understand how the corrosion processes may be different and affect the corrosion fatigue crack growth rate response to different loading conditions. Further, experimental observations of the oxide formation process will provide input to support ongoing modeling efforts related to corrosion and could provide information to indirectly test the validity of the IVEC mechanism.

In the high S heat, a two-layer oxide structure, consisting of an outer layer of Fe_3O_4 and an inner layer enriched in Fe and Cr, was observed in the crack tip enclave following corrosion fatigue testing under conditions known to promote retarded crack growth (Figure 11-1).

In low S heat, the inner Fe, Cr-rich oxide layer does not initially form in the crack tip enclave during corrosion fatigue testing known to promote enhanced crack growth; it likely forms sometime after the crack has advanced and the region is exposed to the environment for some period of time (Figure 11-2).

For both enhanced and retarded crack growth, Fe was identified as the predominant species associated with corrosion in both the high and low S heats of type 304/304L SS. Thus, vacancy injection may be supported by Fe diffusion out of the material.

Differences observed in the oxidation process in the crack tip enclave support the hypothesis that the outer layer of Fe_3O_4 forms by the diffusion of Fe ions out of the base metal and prior to the initiation of the solid state reaction which forms the inner Fe-, Cr-rich oxide layer in low S material. In the high S material, both oxidation processes occur concurrently.

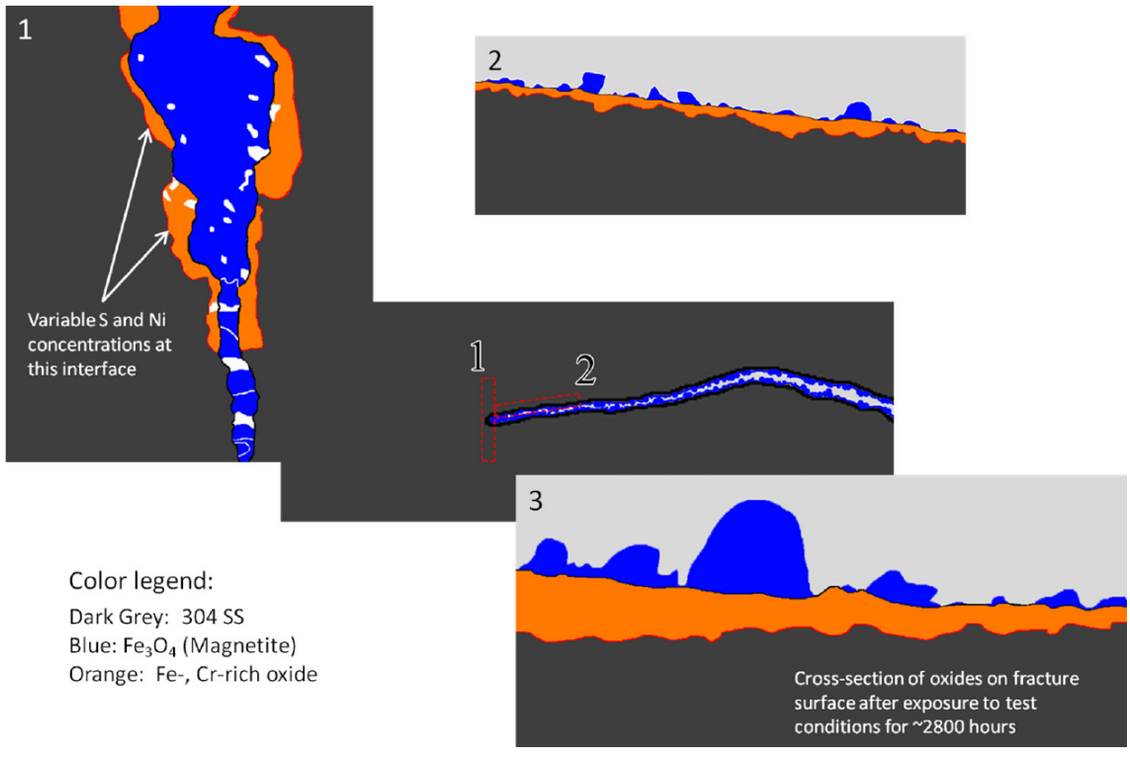

Figure 11-1: Evolution of oxide layers in high S material [Miller B.D. and Paraventi D.J., 2015].

12 PWR secondary side

Alloy 800 is the material of choice for steam generator tubing in CANDU reactors as well as in numerous European nuclear generating stations. Alloy 800 fills a niche between austenitic stainless steels and nickel-based alloys, both in terms of composition and corrosion behaviour. It offers the resistance to chloride-induced stress corrosion cracking of nickel-based alloys without being susceptible to primary water SCC. While the performance of Alloy 800 SG tubing has been exemplary for over 30 years[1], concerns exist about the susceptibility of Alloy 800 to SCC in certain high-temperature, aqueous environments containing sulphur species. Commonly, the ingress of sulphur species in the SG secondary side occurs at low levels from sources such as makeup water, condenser leaks, loss or leakage of ion-exchange resins, and the degradation of lubricants and seals. Since 2006, occurrences of SCC in SG secondary sides have been observed in European NGSs. Axially oriented intergranular attack and SCC was detected in German SGs within the deep tubesheet crevices in Biblis-A NGS and in the top-of-tubesheet region in Unterweser NGS. Circumferential SCC associated with denting was observed in the top-of-tubesheet region in the SGs of Almaraz NGS. The destructive examination of SG tubes from both Biblis and Almaraz revealed a significant presence of sulphur in the corrosion products found within the cracks. The susceptibility of Alloy 800 to SCC in sulphur-containing environments has been demonstrated in laboratory testing. Tapping et al. conducted constant extension rate tensile tests on Alloy 800 in acidic sulphate solutions of $pH_{320°C}$ 3 and 3.7 and reported evidence of SCC susceptibility. De Bouvier et al. observed an apparent threshold for cracking in Alloy 800 c-ring specimens exposed to 0.6 M sulphate solutions at 320°C for 3,000 hours. Cracking was observed in mildly acidic sulphate solutions with a $pH_{320°C}$ of 5.0 (neutral $pH_{320°C}$ is 5.5) but not at more alkaline pH (6-9.5). Model boiler studies of shot-peened Alloy 800 tubes in All Volatile Treatment secondary side water chemistry with injections of Na_2SO_4 and $FeSO_4$ (pH = 4) were carried out by Gómez-Briceno et al. Circumferential cracks were found in the roll transition zone of tubes after 9,500 hours of operation; however, it should be noted that, since the cracks were undetectable by eddy current inspection, the time of initiation and the rate of propagation were unknown. Intergranular SCC (>90% through-wall) was observed by Pierson et al. in expanded Alloy 800 tubes containing a solution of 0.75 M Na_2SO_4, 0.2 M $FeSO_4$ and 0.13 M SiO_2 after only 837 hours at 330°C. More recently, Persaud et al. have used electrochemical methods and c-ring testing to demonstrate the susceptibility of Alloy 800 to SCC in acidic sulphate solutions at a $pH_{315°C}$ of 4.3. Cracks in c-ring specimens to depths greater than 350 µm were observed after only 60 hours. Subsequent studies using focussed ion beam sectioning and analytical transmission electron microscopy identified sulphur in the crack tip oxides.

In the study [Smith J.M. et al, 2015], the relative effects of pH and alloy Cr content on the EAC of Alloy 800NG in high-temperature sulphate solutions were investigated by crack initiation testing on blunt notch specimens and electrochemical methods. Crack initiation testing revealed a clear trend in pH, whereby cracking could be initiated in the near-neutral to mildly acidic pH regime but no cracking occurred above the neutral point (Figure 12-1). The DCPD response suggested that cracking could be initiated within only a few stress cycles at pH values one unit below neutral. Under these conditions, a crack that was actively propagating under cyclic load continued to grow under constant load, albeit at a slow rate of <1 mm/yr. The observation of crack initiation on Alloy 800NG in the near-neutral to mildly acidic pH regime is accompanied by a marked increase in film thickness and change in film morphology (Figure 12-2). This surface film transition can be brought about by either lowering the pH through the neutral point at open-circuit potential or, in more alkaline solutions, by applying a sufficient anodic overpotential. An experimental variant of Alloy 800 containing an additional 3 wt% Cr demonstrated resistance to crack initiation under conditions shown to be aggressive to Alloy 800NG. While the benefit of additional chromium was clearly apparent in crack initiation tests, the polarization curves of higher-chromium variants were indistinguishable from that of Alloy 800NG.

[1] Does not include experience with general wastage and pitting attributed to aggressive conditions associated with phosphate water treatment and chloride ingress at Point Lepreau NGS in the 1980s.

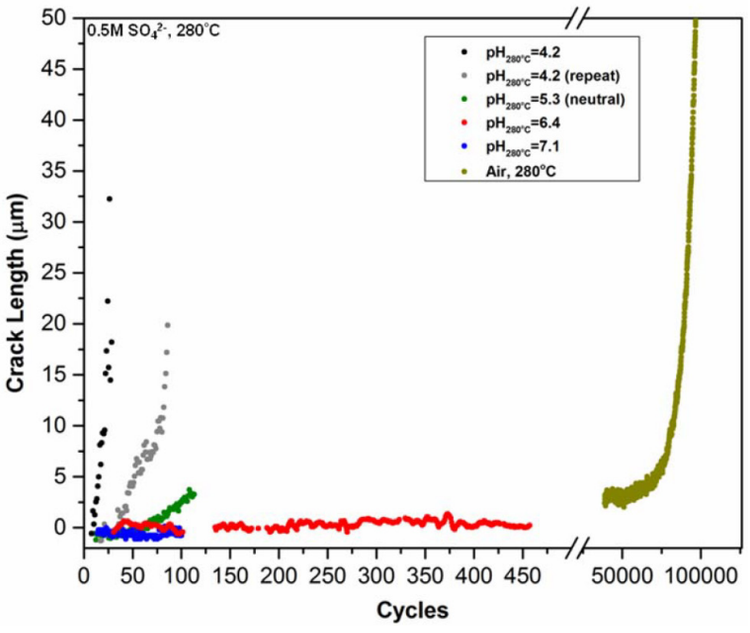

Figure 12-1: Crack initiation tests plotted as crack length (as determined by DCPD) versus stress cycles for Alloy 800NG (20% CW) in both air and sulphate solutions of varying pH [Smith J.M. et al, 2015].

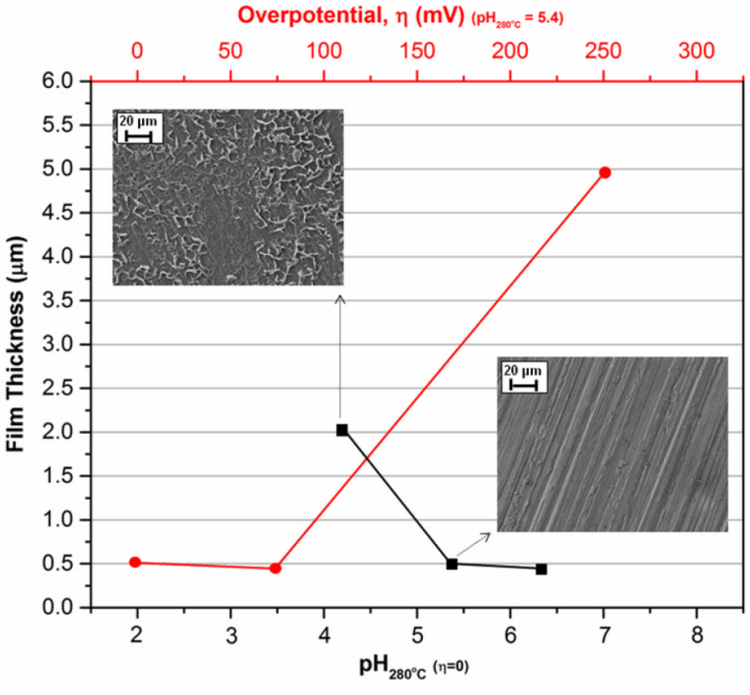

Figure 12-2: A plot showing the changes in surface film thickness and morphology with pH and anodic overpotential [Smith J.M. et al, 2015].

Due to severe SCC susceptibility in primary water, steam generators made with nickel-based Alloy 600 have been replaced with steam generators made with alternate materials such as Alloy 690, a higher chromium nickel based alloy, or Alloy 800, an iron based alloy. As CANDU stations have favoured Alloy 800 for steam generator replacement and refurbishment, a valid basis for long-term prediction of in-service performance of Alloy 800 SG tubing material under plausible CANDU secondary side conditions is required. In general, Alloy 800 has only been observed to crack under extreme conditions

in the laboratory, although recent field experience has indicated that degradation can occur in crevices particularly where the material is cold worked (scratched or otherwise deformed).

Much work has been done to characterize degradation mechanisms in Alloy 800 and Alloy 600 in various environments, including benign environments such as all-volatile treated water, primary water reactor environments and in simulated crevice environments using polarization studies, C-ring tests, and CERT tests. Several studies identified acid sulphate environments as particularly damaging. Polarization and C-ring tests in the simulated crevice environment were used to develop the concept of a safe operating zone of pH and electrochemical potential, where SCC is not expected to occur. However, these tests do not quantify the degradation observed, nor give quantitative assessment of how degradation rates change as the operating chemistry deviates from the normal operating condition as occurs in the event of a chemistry transient. Furthermore, it is unlikely that there is a distinct transition from no degradation to severe degradation as the boundary currently suggests, particularly as time is not considered. There is therefore, a need to develop a map of degradation rates as a function of pH and ECP. The relative effect of the crevice environment on degradation is presented to provide comparison to the performance in benign bulk secondary side AVT water environment. These results are the starting point in the development of an enhanced ECP-pH safe zone map in which degradation severity at different conditions is quantifiable.

The reference [Turi M.L. et al, 2015] presents final test results for interrupted CERT tests performed at 280°C, 300°C, and 320°C on Alloy 800 and Alloy 600 in an acidic crevice environment outside the safe pH-ECP safe zone. Interrupted CERT tests at various strains allow quantification of the degradation as a function of chemistry and deformation.

The surface morphology for the samples tested at 300°C are shown in Figure 12-3. Partial results for tests performed at 280°C and 320°C were previously reported. The complete set of results presented in this paper, concur with previous observations; in Alloy 800NG pitting and general corrosion (wastage) of the sample were the primary degradation mechanisms; Alloy 600MA samples had a heavier oxide, significant grain boundary attack, and a higher density of cracks on the surface than Alloy 800NG, indicative of its greater susceptibility to SCC.

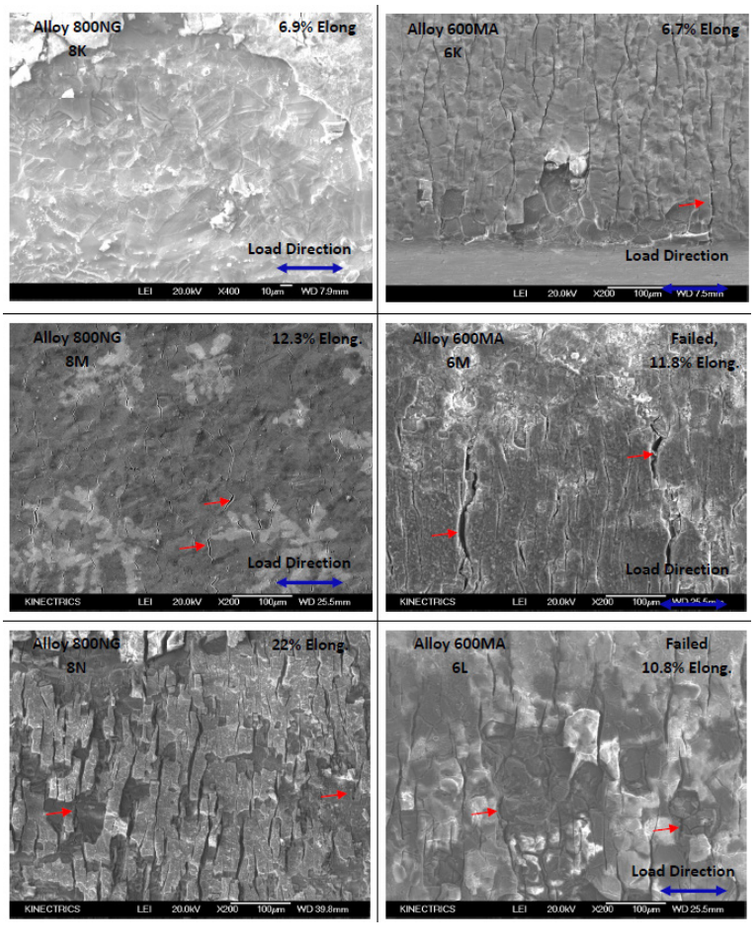

Figure 12-3: Surface characterization for Alloy 800NG and Alloy 600MA SSRT tests performed at a strain rate of $8x10^{-8}$ s^{-1} in an AC environment at 300°C [Turi M.L. et al, 2015].

Since initiation can be defined as the formation of stable, growing cracks, crack density and crack depth were expected to correlate to the initiation rate of SCC. Representative micrographs of the cross sections of the samples are shown in Figure 12-4. Because the elongation of the samples at which the test was interrupted could not be controlled to exactly 7%, crack depth and crack density were normalized by the strain.

13 PWR oxides and deposits

During periodic inspections of PWRs, inspectors are mainly exposed to radiation from ^{58}Co (a half-life of 71 days) and ^{60}Co (a half-life of approximately 5.3 years). ^{58}Co which is converted from Ni by neutron irradiation is the predominant radiation source at the beginning of the operation of the plant. Conversely, ^{60}Co, which is converted from ^{59}Co by neutron irradiation, contributes to the radiation source at the middle of the operation of the plant. To reduce radiation exposure at the beginning of the operation of the plant, it is effective to reduce Ni released from steam generator tubing because the wetted surface area of SG tubing is huge in PWR primary water system. SG tubing made of Alloy 690 is the main source of Ni release because Alloy 690 contains approximately 60% Ni. Thus, pre-filming technology which produces Cr-oxide on SG tubing surface made of Ni-based alloy containing Cr has been developed as one of the technologies to reduce Ni release from SG tubing. In the study of the reference [Momozono Y. et al, 2015], to clarify the effect of pre-film on Ni release and the Ni release behavior on pre-film, metal release test and physical analysis of pre-film were conducted.

It is not easy to evaluate the amount of Ni released from the surface of Alloy 690 into the simulated PWR primary water quantitatively because the amount of released Ni is small in such an environment. Thus there is no standardized way to evaluate the amount of released Ni. For example, some researchers sampled using a filter radionuclide released in nominal PWR coolant condition at the flow rate of 15 L/h from thermally treated Alloy 690 activated by neutrons. In their study, the release of elements was found linear with time. Others estimated the amount of released metal in simulated PWR primary water at a mass transfer coefficient of up to 1.5×10^{-3} m/s by the attenuation of radioactivity by using steam generator tubing whose surface is injected with radioactive ^{56}Co. In their study, the lower the pH was, the higher the release was. Other researchers directly analyzed cation release of Ni base alloys in primary chemistry conditions by connecting test tubing and inductively coupled plasma atomic emission to reach its long-term steady state value.

However, there are few studies treating the effect of high flow velocity on Ni release. The flow velocity in the actual plant is estimated at approximately 5.5 m/s. That is turbulent flow. Thus in this study, in order to simulate the actual plant environment, the amount of Ni released from pre-filmed Alloy 690 tubing was evaluated at high flow velocity, which is turbulent flow, with the new test system.

Figure 13-1 shows a schematic diagram of the recirculation type metal release test equipment. Under this test system, Ni released into the test solution is sampled with some filters, and analyzed by inductively coupled plasma mass spectrometry and atomic absorption spectrometry. Thus one of the characteristics of this test system is evaluating the amount of released Ni directly. This equipment consists of a test solution recirculation line and a test solution sampling line for analyzing released Ni. To prevent Ni released from the equipment except the test specimen, the components where test solution flows at high temperature are made of pure Ti. Thus the components where test solution flows at room temperature are made of resin. Additionally, before metal release tests, the solution lines are cleaned by 0.2% nitric acid at room temperature and deionized water at 325°C to reduce the concentration of Ni to < 0.01 ppb. The calculated flow velocity of the test solution is 1.7 m/s and the calculated Reynolds number is 22,000 because metal core made of Ti is inserted in the test specimen (Alloy 690 tubing). The dissolved oxygen was reduced to < 10 ppb by the bubbling of high purity Ar gas in the solution controlled tank. Next, the temperature of the test solution was controlled by the heater at the test temperature, and then dissolved hydrogen was controlled 2.6 ppm by pressurizing high-purity H_2 gas. Subsequently, metal release test was started by switching a valve. During the metal release test, the test solution is always recirculated at high temperature and high flow velocity.

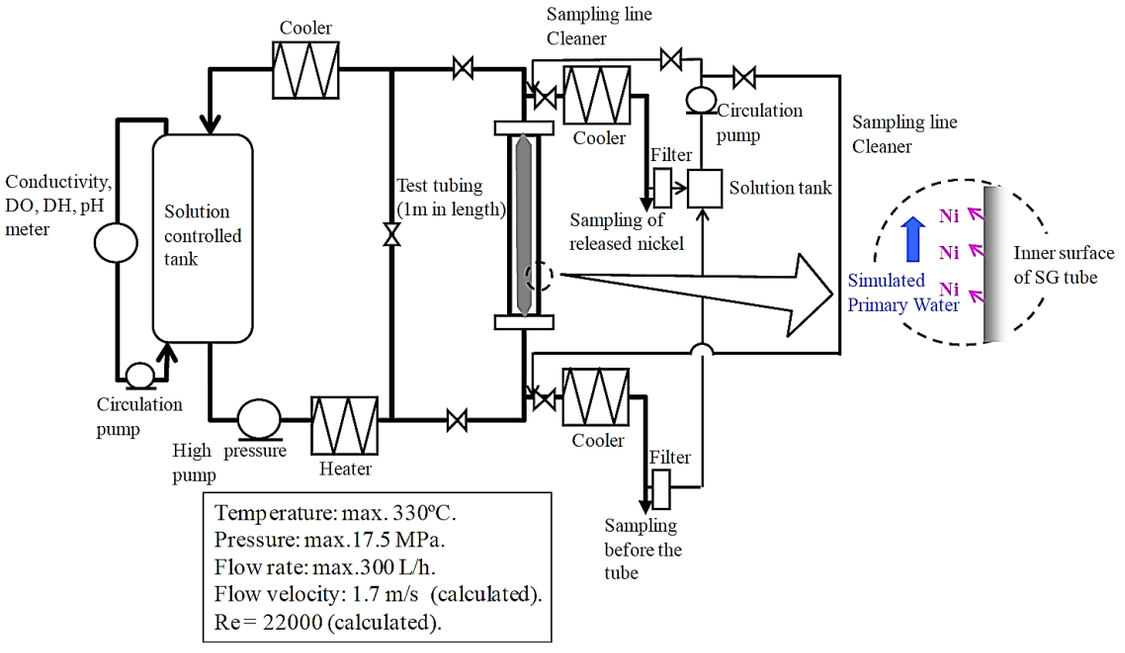

Figure 13-1: Schematic diagram of recirculation type metal release test equipment [Momozono Y. et al, 2015].

It has been demonstrated that the Ni release rate of pre-filmed Alloy 690 tubing was much lower than that of non pre-filmed Alloy 690 tubing. To reveal the mechanism of reducing Ni release by pre-filming, the reaction resistance of metal release was measured by an electrochemical method of anodic polarization resistance. The specimens were Alloy 690 sheets having 10 mm length, 10 mm width, and 1 mm thickness. These specimens were immersed in autoclaves filled with simulated PWR primary water for 100 h to compare the property of pre-filming with that of corrosion products on non pre-filmed specimen surface. Next, these specimens were connected to lead wires for electrochemical measurements. The contact point of the specimen and the lead wire was sealed with silicone. Figure 13-2 left shows the schematic diagram of the electrochemical measurement. The test solution was 0.5 M Na_2SO_4 bubbled with Ar gas. The temperature was controlled at 35°C. The potential was swept from open circuit potential to OCP + 10 mV. The sweeping rate of the potential was 2 mV/s. Figure 13-2 right shows the result of the anodic polarization resistance of pre-filmed Alloy 690 and non pre-filmed Alloy 690 after the immersion test in simulated PWR primary water for 100 h. ΔE represents the over voltage. I represents the current density. The anodic polarization resistances of pre-filmed Alloy 690 and non pre-filmed Alloy 690 calculated by Ohm's law are 8.1×10^{-1} and 3.3×10^{-2} $M\Omega \cdot cm^2$, respectively. The anodic polarization resistance of pre-filmed Alloy 690 was approximately 10 times higher than that of non pre-filmed Alloy 690 which was assumed to permit passivation during the immersion of 100 h. This result indicates that pre-filming is protective toward metal release.

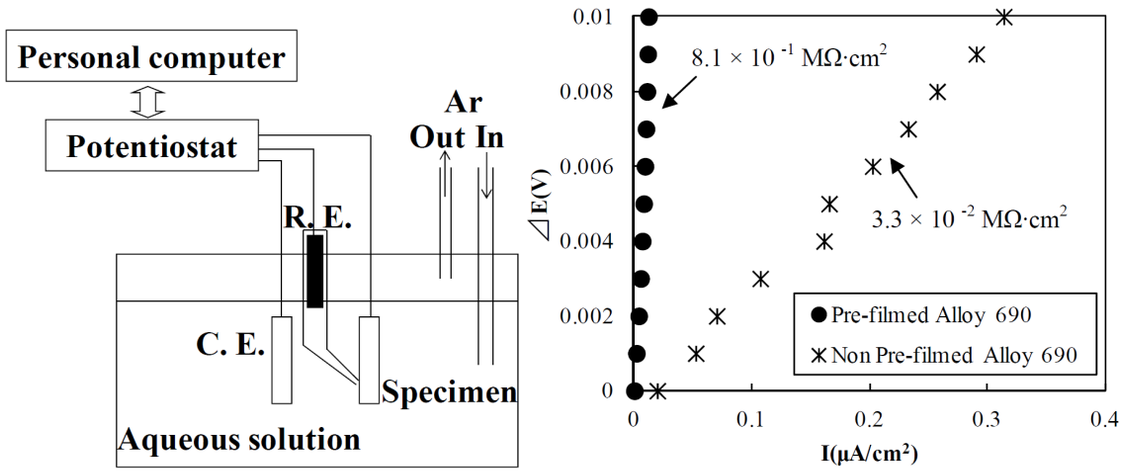

Figure 13-2: Left: schematic diagram of the electrochemical measurement.
Right: result of the anodic polarization resistances of pre-filmed Alloy 690 and non pre-filmed Alloy 690 in 0.5M Na_2SO_4 aq. at 35°C after immersion test in simulated PWR primary water for 100 h [Momozono Y. et al, 2015].

Since the pre-film consisting of Cr-oxide shows almost no change even after the metal release test and high anodic polarization resistance, Cr_2O_3 layer should be responsible for the high resistance of the prefilm for Ni release. However, an infinitesimal amount of Ni was released from pre-filmed Alloy 690 at the beginning of the metal release test. The source of the infinitesimal amount of Ni released from prefilmed Alloy 690 could be the surface layer of the pre-film. As shown in Figure 13-3, Ni and Mn decreased after the metal release test. It was clarified that the structure including Mn was $MnCr_2O_4$ by XRD. It is assumed that Ni in $MnCr_2O_4$ is released as shown in Figure 13-4. Ni could exist as $NiCr_2O_4$ with $MnCr_2O_4$ thermodynamically. However, there is another possibility that Ni is released through the defects of the pre-film from Alloy 690 matrix. To clarify the details of Ni release behavior on the pre-film, further investigation is required.

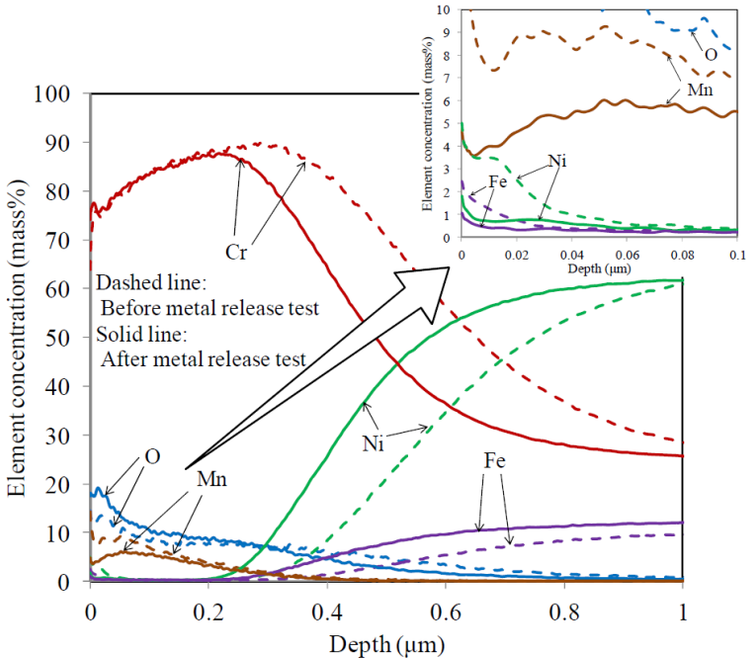

Figure 13-3: GDS depth profile of pre-filmed Alloy 690 tubing before and after recirculation type metal release test [Momozono Y. et al, 2015].

14 Welds and weld metals

The reference [Moss T. et al, 2015] reports results from two SCC crack growth rate tests of high chromium nickel based alloys (one Alloy 690 and one EN52i test). The goal of this testing was to quantify the temperature dependence of SCC growth in Alloy 690. A second goal of this testing was to better understand why prior EN52i testing reported by [Morton D.S. et al, 2013] has suggested a weaker temperature dependency than other nickel based alloys. A periodic partial unload bias and difficulties in measuring accurate SCC growth rates in the SCC resistant EN52i are possible reasons for this weaker than expected temperature functionality.

Cold worked Alloy 690 SCCGR test results in this study and by other investigators suggest that Alloy 690 has a similar temperature functionality to other nickel based alloys like Alloy 600 (i.e., Figure 14-1 shows a SCC thermal activation energy of 113±18 kJ/mol).

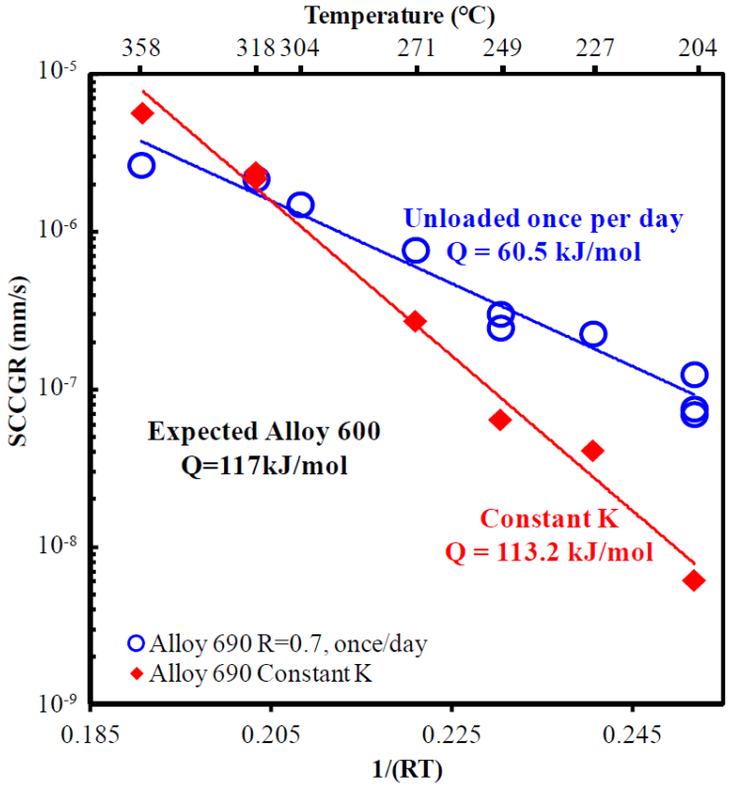

Figure 14-1: Temperature dependence of Alloy 690 SCCGR plotted as a function of 1/RT (R = 8.314x10^{-3} kJ/mol·K). Results suggest that Alloy 690 SCCGR follows an Arrhenius temperature functionality with a similar thermal activation energy to Alloy 600 (113.2±18 kJ/mol vs. 117 kJ/mol) when loaded under constant K conditions, shown in filled diamonds. Shallower temperature dependence (60.5±10 kJ/mol) was observed for conditions where the sample was unloaded once per day, shown in hollow circles [Moss T. et al, 2015].

Cold worked EN52i indicated measurable SCC at 327°C whereas the SCCGR at 254°C was below the detection limit of the test. This result suggests that EN52i weld metal tested under constant K condition has a SCC activation energy larger than that previously measured in experiments conducted with once per day unloads. Analysis indicates this temperature dependence is > 83 kJ/mol.

Alloy 690 testing has demonstrated that periodic partial unloads can appreciably accelerate SCCGRs. In reduced temperature test phases, once a day periodic partial unloading enhanced the measured constant load SCCGR (e.g., at 204°C the constant K SCCGR of 6.2x10^{-9} mm/s was increased by over 10X under once a day periodic partial unloading). Periodic partial unloads enhance SCCGRs at reduced temperature and significantly lowered the measured thermal activation energy. This bias in the temperature dependence must be accounted for efforts to model Alloy 690 SCC growth.

Alloy 690 SCCGR is a function of coolant hydrogen concentration and is generally consistent with that observed in Alloy 600 (i.e., Alloy 690 SCCGRs are approximately 2.5x faster under coolant hydrogen concentrations that drive electrochemical potentials closer to the Ni/NiO phase transition (ΔECP=0)).

The excellent SCC growth rate performance of Alloy 690 and EN52i can be significantly degraded if the material is cold worked. Alloy 690 SCCGRs measured in this study were the fastest SCCGRs that have been measured for Alloy 690 in primary water. The cold rolled EN52i had an average crack growth rate of $1.5x10^{-7}$ mm/s at 327°C, also one of the fasted growth rates observed.

An international review performed in 2007 revealed an increased occurrence of defects in nickel based alloys used in DMW since the 90's. The Alloy 82 is used in connection to reactor pressure vessel between safe end (stainless steel) and vessel nozzle (low alloy steel), or in steam generator nozzle and tubes. In those localizations, the Alloy 82 is present in cladding, buttering and welding modes. In France, all welds are stress relieved because of base metals. The Alloy 82 is also present in welds repair, initially in Alloy 182, but after the repair the Alloy 82 is not stress-relieved. The majority of the 300 DMW crack cases listed in this report concerns Alloy182 and only 3 cases concern Alloy 82. In literature, initiation times, times to failure and crack growth rates on nickel-based alloy welds, and particularly on Alloy 82, can be found. Nevertheless, a significant scattering of these values is observed. This scattering could be explained, among other things, by the grain size of the nickel-based alloy weld which is millimetric even centimetric and by the mechanical behavior induced by this microstructure. Furthermore, crack front, from crack propagation test, is fingered with a SCC extent that depends on the considered area. These observations lead to the hypothesis that the crack path depends on the grain boundary properties.

In this context, the study referenced [Chaumun E. et al, 2015] is carried out to better understand the initiation of SCC cracks in Alloy 82. In order to accelerate testing time, SCC tests were performed in hydrogenated steam at 400°C instead of primary water at 360°C. In the literature, some authors noticed that the time to failures decreased when the test environment is in hydrogenated steam compare to simulated primary water. Economy et al. tested reverse U-bend in hydrogenated steam and observed that the initiation mechanism in hydrogenated steam is similar to the simulated primary water. The composition of the oxide layer in hydrogenated steam was observed by Chaumun et al. The authors concluded that the oxide layer is similar to the one formed in simulated primary water, excepted to the chromium oxide form. In hydrogenated steam, the chromium oxide is a continuous layer in the inner layer compared to the primary water condition where the chromium oxide is in spinel form inside the inner layer. The microstructural and mechanical characterizations carried out in this study aim to identify a critical parameter governing the SCC crack initiation in Alloy 82. In this framework, 26 U-bend specimens were tested. SEM images of cracks were correlated with both the microstructure characterized by EBSD analysis and the surface strain fields obtained by DIC. This paper focuses on results concerning initiation tests through the correlation between initiation sites, the microstructure and the local mechanical behavior of specimens. To complete the mechanical analysis, numerical simulations have been carried out to estimate the stress fields along cracked and uncracked grain boundaries.

Crack initiation tests showed intergranular SCC cracks perpendicular to the loading direction. Crack initiation times ranged between 500 and 1,500 hours for U-bend specimens from as-welded welds (A and B), and ranged between 1,500 and 2,500 hours for U-bend specimens from the heat-treated weld A (only one U-bend specimen with one SCC crack). Difference in SCC susceptibility between the as-welded welds cannot only be assigned to the difference of chromium and carbon contents as the welding processes were also different (GTAW for the weld A and FCAW for the weld B). The good SCC behavior of the heat-treated weld A may be attributed to the formation of chromium carbides along grain boundaries.

The correlation between initiation sites images and EBSD maps of the microstructure confirmed the localization of SCC cracks on high angle grain boundaries perpendicular to the loading direction (Figure 14-2). No preferential crystal orientation of adjacent grains next to the cracked grain boundary has been identified. Nevertheless, in most cases of U-bend specimens with TL orientation, SCC cracks were localized in small grain size zones. Strain fields measured on the surface of U-bend specimens showed heterogeneous deformations at macroscopic and microscopic scales. The correlation between

strain fields and SCC cracks has led to the conclusion that a high level of deformation was not sufficient to initiate SCC cracks.

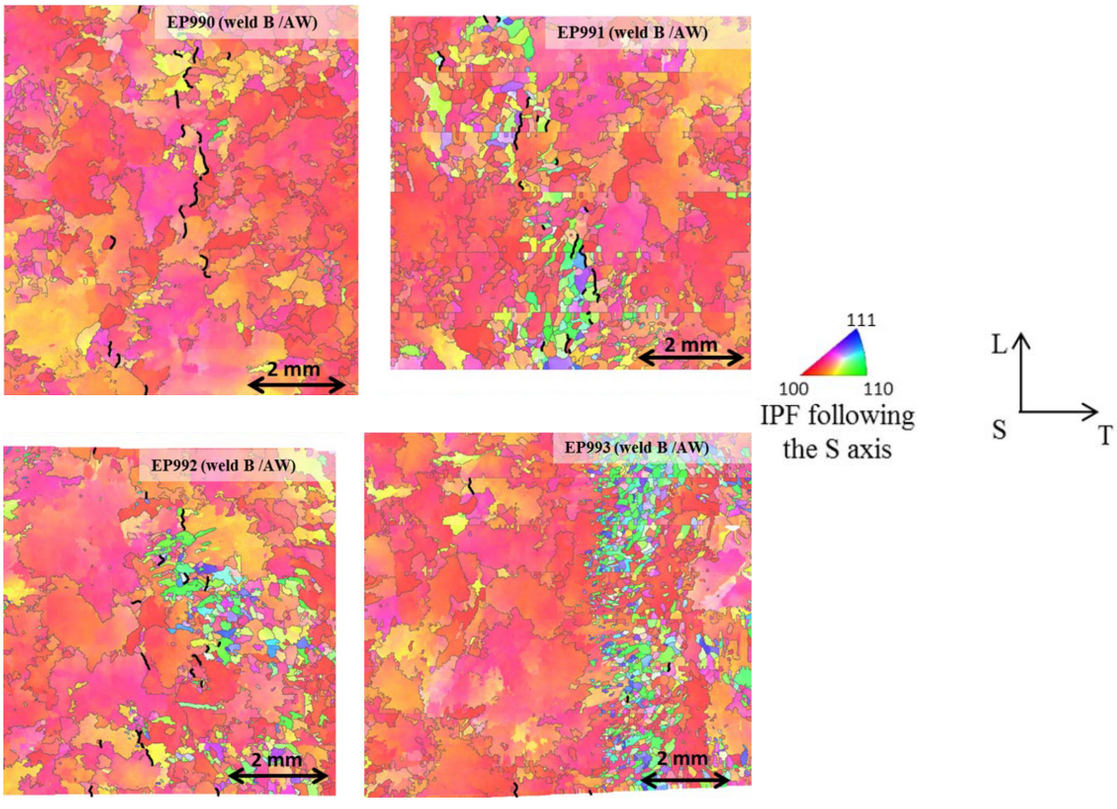

Figure 14-2: Correlation between initiation sites (black lines) and EBSD analysis of EP990, EP991, EP992 and EP993 from the as-welded weld B, with TL orientation, indexed with IPF coloring along S axis. On EP991 sample strain fields along loading direction are superposed [Chaumun E. et al, 2015].

Numerical simulations were performed to investigate the stress fields around cracked and uncracked grain boundaries. ExBC simulations showed a critical normal stress which could separate cases of cracked and uncracked grain boundaries cases. Moreover, it has been observed that cracked grain boundaries had greater $\Delta\varepsilon_{gb}$ than uncracked ones (Figure 14-3). In order to approach the real behavior of the grain boundaries, simulations can be expanded to include more grains around the grain boundary and could take into account the orientation of the grain boundary plane with respect to the loading direction.

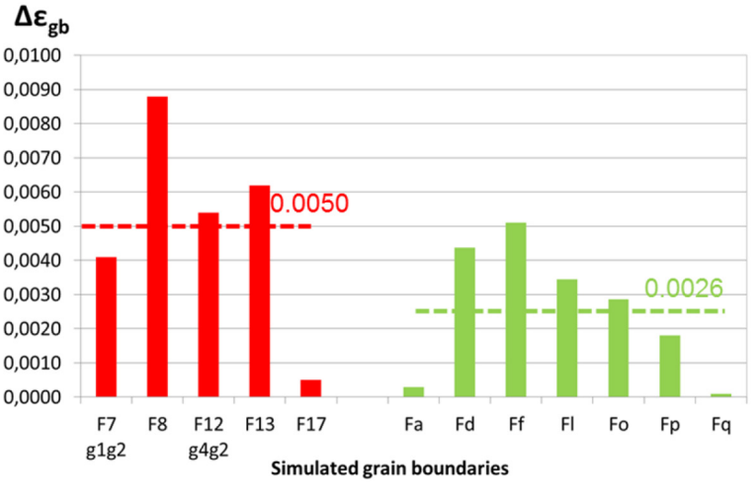

Figure 14-3: $\Delta\varepsilon_{gb}$ for cases of cracked (red) and uncracked (green) grain boundaries and averages values for each case with the ExBC imposed on the outline of the bi-crystal [Chaumun E. et al, 2015].

The small grain size zones can also be explored. In fact, it has been observed that small grains zones are mainly localized in the bottom of welding passes. This observation raises the question of the chemical composition homogeneity over the welding passes. Electron Probe MicroAnalyzer and Secondary Ion Mass Spectrometry analyses are in progress to detect potential grain boundary precipitations or segregations.

There is no field experience of Alloy 690 PWSCC failures in operating plants dating back to 1989. Furthermore, laboratory PWSCC initiation tests with accelerated temperature condition at 360°C have showed no PWSCC with as much as 100,000 hours of exposure with stress level of 300 to 550MPa. However, it has been reported that crack growth of Alloy 690 and weld metals has occurred in carefully designed laboratory tests. Crack growth has been reported as result of testing in simulated PWR primary water environment under periodic unloading condition followed by constant loading. Now a considerable amount of data for crack growth of Alloy 690 TT in simulated PWR primary conditions have been reported especially for cold worked material. A critical issue that remains is PWSCC initiation and data is needed to verify long-term reliability for Alloy 690. The Japanese PWR Utilities & MHI have been conducting uni-axial constant load PWSCC initiation tests for Alloy 690 ([Sakima K. et al, 2015]).

PWSCC initiation test results are shown in Figure 14-4 to Figure 14-7, including results from Alloy 600 MA SG tube PWSCC initiation test results that were previously obtained. No PWSCC initiation was observed for any of the Alloy 690/52/152 specimens. The test environment was well maintained. The water quality of simulated PWR primary conditions during the test period, and regular monitoring showed that the measured chemistry values matched the planned values.

- Alloy 690 TT CRDM Nozzle: No PWSCC initiation for more than 110,925 hours.
- Alloy 690 TT BMI Nozzle: No PWSCC initiation for more than 95,965 hours.
- Alloy 152 (SMAW) weld metal: No PWSCC initiation for more than 122,726 hours.
- Alloy 52 (TIG) weld metal: No PWSCC initiation for more than 122,535 hours.
- Alloy 52/316 SS dissimilar joint: No PWSCC initiation for more than 30,166 hours.
- Alloy 690/52/152 with cold-worked surface layer: No PWSCC initiation for more than 26,796 hours.
- Alloy 690 TT mechanical plug mock-up: No PWSCC initiation for more than 8,958 hours.

15 Welds, assessments and modeling

Primary Water Stress Corrosion Cracking is considered as a possible cracking mechanism for Dissimilar Metal Welds in outlet feeders at some CANDU plants. These DMWs join SA-106 carbon steel piping with Alloy 600 flow element and are fabricated using Gas Tungsten Arc Welding with filler metal Alloy 82 or Alloy 182. Based on the effective degradation years method, DMWs at some CANDU plants with flow elements in the outlet feeders are currently in the high range prior to reaching end of life. These DMW welds shall be subject to periodic inspection as per the CSA N285.4-05 requirements because of the susceptibility to PWSCC. Due to the consideration of high radiological dose and the inherent difficulty of Non-Destructive Examination technique associated with the feeder DMW inspection, a technical approach based on Risk-Informed Leak-Before-Break is being developed to support a request for inspection exemption of these outlet feeder DMWs. The reference [Duan X. et al, 2015] describes the key elements of this approach.

A three-tier LBB approach has been developed to assess the risk of not perform cracking inspections of feeder DMWs.

Level 1: Deterministic LBB assessment. This is the simplest assessment. The uncertainties in the inputs such as idealized crack morphology, surface roughness and WRS are implicitly addressed through the use of large safety factors. On top of the conventional LBB requirements, the current Canadian practice also adds the requirements to establish the consequential leakage and the time from incipient leakage to pipe rupture.

Level 2: AFEA flaw evaluation. This method provides justification for the postulated crack size adopted in the deterministic LBB assessment. The critical inputs to this evaluation include WRS, crack growth rate and physical parameters for the leak rate calculations. Given the uncertainty in WRS and the associated cost for the implementation, AFEA flaw evaluation is used to supplement the deterministic LBB assessment, which does not consider WRS. WRS is explicitly accounted for in the AFEA flaw evaluation which simulates natural crack growth behaviour. The predicted leakage using the complex crack shape is the best and most accurate method currently available.

Level 3: Probabilistic LBB assessment. This method uses inputs with statistical distributions covering the entire range of possibilities. The propagation of uncertainties in inputs is treated by probabilistic software and are reflected in the distribution of leak, break and rupture probabilities. The output of this assessment is a probability number quantifying the likelihood that a weld meets the LBB criteria for a specified confidence level. Probabilistic LBB assessments could be used to replace deterministic LBB assessments. However, given the lack of accepted acceptance standards and the on-going debate on the validation of probabilistic fracture mechanics software, probabilistic LBB assessment is adopted to supplement the deterministic LBB assessment. Risk-informed insights from extensive sensitivity studies provide the designer, utility and regulator unique insights of the risks associated with different degradation management strategies, for example relaxation of the requirements for inspection of DMWs.

The afore mentioned three levels of assessment demonstrate the robustness of the proposed RI-LBB approach and the independence of the key elements. The successful demonstration of each assessment level, on its own, ensures significant margins against pipe rupture. Each of these assessment levels is independent from the others, in that there is no commonality of the underlying physical phenomena or analytical approaches. Moreover, when applied in combination, the residual uncertainties in one level are mitigated by the strengths of the others. The use of multiple, complementary and reinforcing assessments in the proposed RI-LBB approach effectively provides a form of defence-in-depth with respect to the confidence in the overall results.

The Electric Power Research Institute and the US Nuclear Regulatory Commission are developing a modular based, comprehensive probabilistic piping system assessment methodology known as xLPR. xLPR Version 1 was an initial pilot study and demonstrated a strong influence of pressurized water stress corrosion cracking crack initiation modeling on the analysis results. Thus, extensive efforts were made to determine the most appropriate PWSCC crack initiation models for nickel-based weld metals Alloy 82, Alloy 182 and Alloy 132 for use in xLPR Version 2. Three model forms were made available in xLPR, termed Direct Model 1, Direct Model 2 and the Weibull model. The three models share an

Arrhenius temperature dependency (Equation 1). Direct Model 1 and the Weibull model share a stress power-law and a stress threshold (Equation 2).

Eq. 15-1: $\text{Crack Initiation Time} \propto \exp(-Q / R*T)$

where,

Q = Activation Energy

R = Universal Gas Constant

T = Temperature

Eq. 15-2: If stress > stress threshold, then: $\text{Crack Initiation Time} \propto \text{stress}^{-n}$

where n = Stress Exponent

The reference [Troyer G. et al, 2015] describes efforts to compile Alloy 82, Alloy 182 and Alloy 132 laboratory data to estimate the following parameters common to these three models: the thermal activation energy, Q, the stress exponent, n, and stress threshold. A companion paper presented at this conference ([Schmitt K.P. et al, 2015]) describes the integration of these efforts with field experience to calibrate the three crack initiation models to a common operating experience database.

PWSCC crack initiation testing of Alloys 82/182/132 has been performed in laboratory settings for about 25 years. The scope of this literature search was limited to constant load crack initiation specimens exposed to simulated primary water conditions. Slow strain rate tensile or constant elongation rate tensile specimens were excluded from the literature review. While a large volume of bent beam type specimen results was compiled in this review, constant load tensile specimens and pressurized capsule specimens are judged to provide a better means of estimating the effect of near surface stresses on crack initiation times than bent beam type specimens. Thus, data from bent beam type specimens are not further addressed in this paper. The pressurized capsules discussed in this report are formed by machining cylinders from an Alloy 182 butt weld with the longitudinal axis of the capsule transverse to the weld. Alloy 600 plugs were welded into each end of the tubes. Crack initiation time was identified by loss of pressure in the capsule and subsequent confirmation of cracking in the Alloy 182 weld material via visual examination.

In summary, this paper presents a detailed review of laboratory PWSCC initiation testing of nickel-based weld Alloys 82, 182 and 132 to estimate stress and temperature effects. Analysis of an assortment of laboratory data shows a best estimate stress exponent of n = 5 (Figure 15-1). There is insufficient information to conclusively confirm or refute the concept of a stress threshold, below which PWSCC initiation is not expected to occur. Limited information is available regarding thermal activation energy – a best estimate of 185 kJ/mol is recommended.

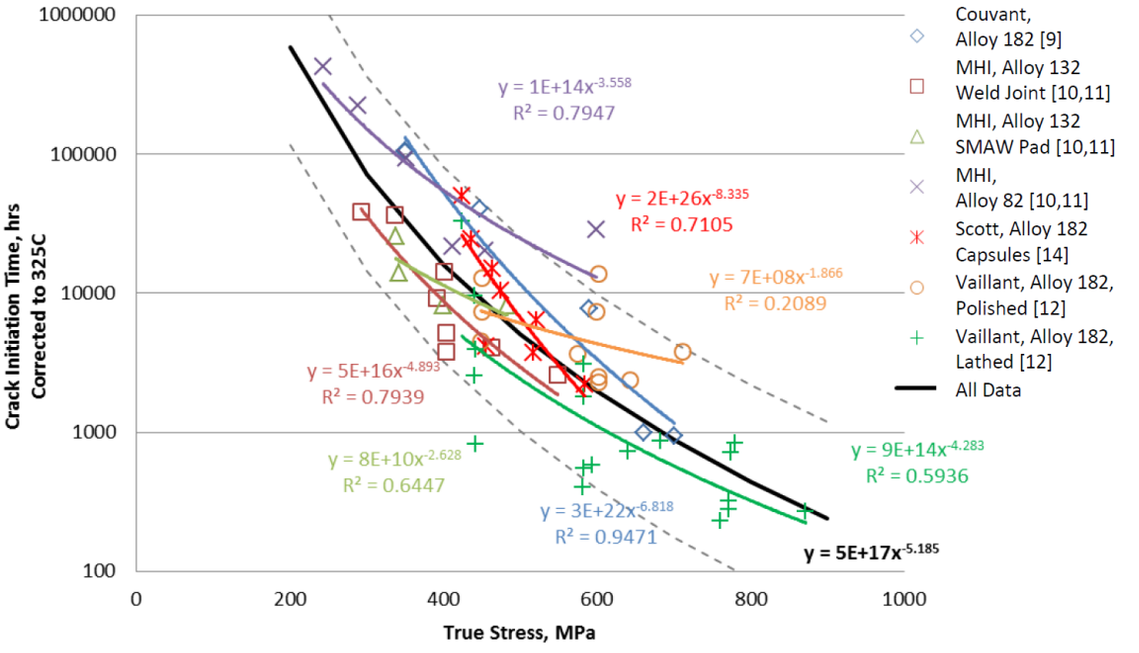

Figure 15-1: Power law fit for stress exponent for specimens with PWSCC initiation [Troyer G. et al, 2015].

The xLPR project deliverable is an integrated software tool that may be used to demonstrate quantitative compliance with 10 CFR 50 Appendix A, General Design Criteria 4 required for approving reactor coolant system lines for leak-before-break exemptions. An immediate focus of the xLPR project is leakage and rupture risk prediction for Alloy 82/182/132 dissimilar metal piping butt welds—e.g., pressurizer safety relief nozzles, reactor pressure vessel outlet nozzles—where PWSCC degradation is active. To support the xLPR project, a rigorous effort is being conducted to ensure that the PWSCC initiation models consistently reflect current laboratory and operating experience for Alloy 82/182/132 weld materials.

Key PWSCC susceptibility differences related to material processing, fabrication, and welding are difficult in practice to quantify for plant components and therefore difficult to recreate in a laboratory setting; thus, PWSCC initiation predictions for pressurized water reactor components are often based on the most relevant set of field experience. In such approaches, the model used to predict the time to PWSCC initiation is calibrated to the relevant set of plant experience with adjustments for differences in temperature and stress modeled on the basis of laboratory testing results. Predictions based solely on laboratory results have historically under-predicted initiation times observed through field data (e.g., flaw detection data) as laboratory testing often is performed for aggressive material conditions (e.g., plastically strained samples, highly susceptible microstructures) and aggressive surface conditions (e.g., abusive grinding) to initiate flaws in reasonable test periods.

The reference [Schmitt K.P. et al, 2015] presents a generalized statistical framework for the integration of laboratory and field data in the development of a probabilistic model for the prediction of the PWSCC initiation time of a flaw of engineering scale. Section 2 provides an overview of the xLPR software and the model forms available for PWSCC initiation simulation; Section 3 introduces the general approach for integrating laboratory and field data; Section 4 details the statistical framework used for failure time model parameter estimation, addressing a number of practical issues encountered in applying classical techniques to field detection data. Section 5 provides illustrative results. However, since the primary objective of this paper is to convey and discuss modeling methodology, the results provided herein are based on preliminary efforts completed to date and are not intended to be comprehensive.

In summary, this paper presents a versatile generalized statistical framework that may be applied to develop parameter estimates for PWSCC initiation model forms to be utilized as part of the xLPR program, incorporating both laboratory and field experience. Beyond xLPR, many aspects of this framework are appropriate for general accelerated failure time models. Challenges addressed that are

16 Ferritic steel SCC & corrosion fatigue

Structural integrity of the reactor pressure vessel of light water reactors is of utmost importance with regard to safety of operation and service lifetime. In addition to the known life limiting degradation processes (irradiation embrittlement, environmentally assisted cracking and thermomechanical fatigue, concerns due to detrimental environmental effects remain that can be attributed to hydrogen uptake from coolant and/or corrosion reactions. Direct contact of RPV steel and coolant occurs via cracks in the protective austenitic stainless steel cladding formed during fabrication, or during reactor operation. Furthermore, the presence of open, incipient, cracks has always to be assumed in safety analysis. The RPV steel picks up hydrogen from the LWR coolant (hydrogen from radiolysis and intentional additions) and corrosion reactions and reaches equilibrium bulk concentrations of up to a very few ppm within a few weeks or months at 300°C, which is high enough to affect their mechanical and fracture properties. Detriment in mechanical properties of base metal and heat affected zone of RPV steels have been reported at hydrogen concentrations (2.5-3.5 ppm) similar to that picked up in the same material, after exposure to primary water in a nuclear reactor (1-5.8 ppm). Furthermore, crevices/cracks with aggressive occluded crevice chemistry will result in even higher concentrations of absorbed hydrogen, irrespective of bulk coolant chemistry. There is now growing experimental evidence that the mechanical properties of most structural materials might be degraded by exposure to reactor coolant (hydrogen effects) in the LWR operating regime. Though calculations indicated hydrogen in RPV to be benign at reactor operating temperatures, there is experimental evidence indicating the contrary.

Hydrogen effects on tensile behaviour of low alloy steel are strongly influenced by temperature, microstructure, and strain rate. Most of the reported studies were done at room temperature, or below, where the effects are most significant. There are a limited number of test results reported indicating embrittling effects of hydrogen at temperatures in the range of 250-288°C. The weld HAZ, specifically the high hardness, coarse grain HAZ, is highly susceptible to hydrogen effects. Hydrogen effects on EAC behaviour of LAS in high temperature water, and synergistic (or competitive) effects with dynamic strain aging, are well recognised. These synergistic effects can have a greater significance for weld HAZ material.

A few earlier studies have reported detrimental effects on the fracture of LAS due to exposure to 288°C water. Environmental effects in water at 288°C were reported to be manifested as occurrence of a greater number of pop-in events attributed to synergy between corrosion generated hydrogen and DSA, but without changing the initiation fracture toughness. In another study, a trend of reduction in fracture toughness and crack growth resistance as extension rates were decreased was noted for tests in 288°C water and this was attributed to the high sulphur content of the steel. Elongation rates used for the fracture toughness tests were low and the measured toughness and crack growth resistance reduced with reducing extension rates. This is an indication of possible apparent reduction in toughness due to a significant role of EAC at the test extension rates. Moreover, there are no reported fractograph after fracture toughness tests using LAS in water at 288°C.

In the reference [Roychowdhury S. et al, 2015], the effect of hydrogen and high-temperature water on tensile and fracture properties of low-alloy RPV steels at different temperatures, strain rates and microstructures was investigated. Detailed post-test characterisation was done to understand the influence of high-temperature water and hydrogen on tensile and fracture properties at elevated temperatures. The present paper summarises the first results from an on-going project which aims to identify critical combinations of microstructure (including simulating weld HAZ microstructures), environmental factors (hydrogen level, temperature) and loading conditions (strain rate), that result in significant high-temperature water and hydrogen effects in the LWR temperature regime. The present paper is an update of a previous publication. It is stressed that effects of high-temperature water on fracture toughness were massively overestimated in that publication due to a systematic error in the evaluation procedure of the EPFM tests and were not confirmed after proper evaluation.

All the tests were followed by detailed fractographic analysis to establish the mode of fracture; from the results the following conclusions can be made:

Hydrogen in the range of 2 to 5 ppm in the RPV steel resulted in embrittlement in tensile tests in air, both at 25°C (room temperature) and at 288°C and the embrittling effects was more significant at 25°C, at higher hydrogen contents in the steel and in the CGHAZ material with higher yield stress.

Maximum embrittling effects were observed at strain rates of 10^{-5}-10^{-4} s^{-1} and 10^{-3}-10^{-2} s^{-1} at 25 and 288°C, respectively that were related to the matching of dislocation mobility and hydrogen diffusivity.

In the investigated loading rate range (0.25 to 0.35 mm·min^{-1}), "severe" hydrogen pre-charging, resulted in sudden unstable brittle crack extension without prior stable ductile crack growth at 25°C, while at 288°C stable ductile crack extension occurred for the same "severe" hydrogen charging conditions (Figure 16-1). No reduction of initiation toughness and tearing resistance was observed at 288°C after severe hydrogen pre-charging, although a clear change in fracture morphology was observed.

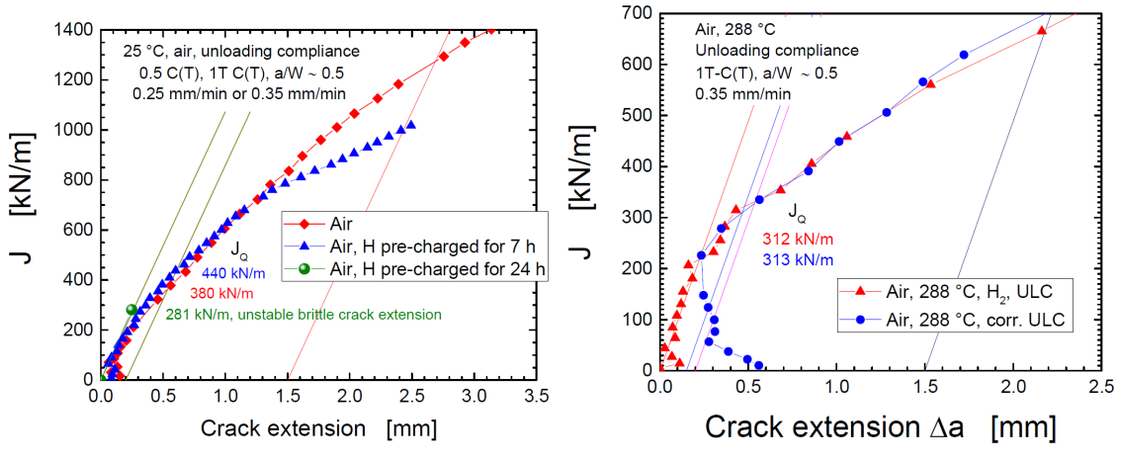

Figure 16-1: J-Δa plots in air at 25°C (left) and 288°C (right) in the as-received condition (0 ppm) and after hydrogen pre-charging. Unstable brittle fracture surface after "severe" hydrogen charging at 25°C [Roychowdhury S. et al, 2015].

At the same loading rate, exposure to high temperature water containing dissolved hydrogen (BWR/HWC, PWR), dissolved oxygen (BWR/NWC) or with additional electrochemical in-situ hydrogen charging (PWR) for 12 days (up to 32 days) did not reduce the initiation toughness and tearing resistance with respect to corresponding air tests. A clear change in fracture morphology and deformation structures was observed that was very similar to that in EPFM and tensile tests in air with hydrogen pre-charging. The type of environment and period of pre-oxidation and type of loading during the pre-oxidation did not affect the toughness values.

Detailed fractographic analysis revealed that embrittlement in tensile tests in air and the change of fracture morphology are related to (hydrogen-induced) extensive localization of plastic deformation (due to micro-void coalescence) and not to a microscopically brittle process (Figure 16-2). Besides micro-void coalescence, various amounts of quasi-cleavage and secondary cracking as well as macro-void (> 100 µm) formation were observed in case of hydrogen pre-charging or in high-temperature water which were manifestations of localization of plasticity.

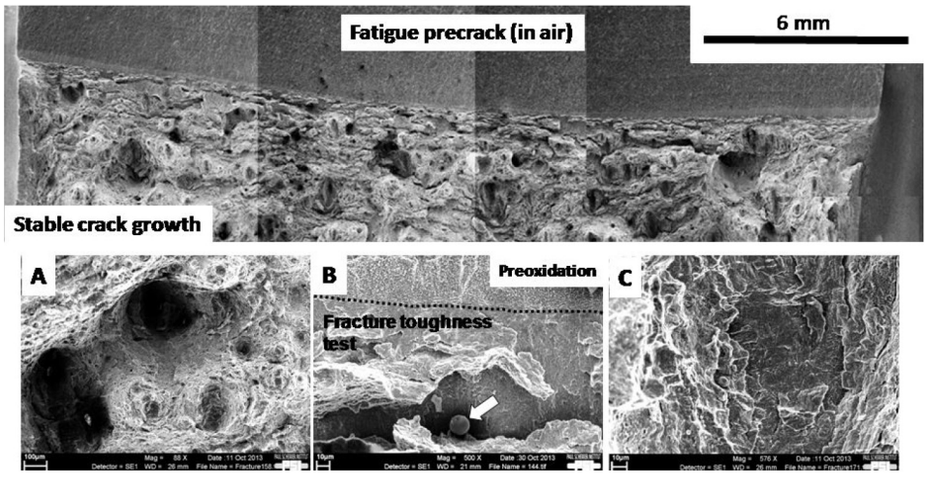

(a)

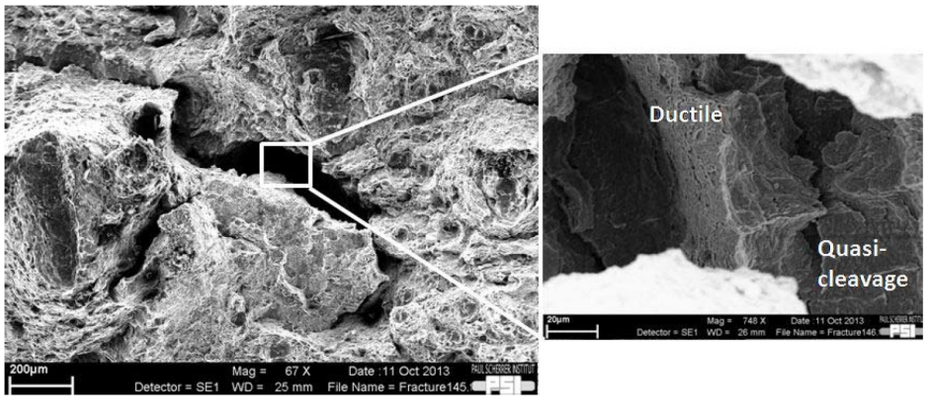

(b)

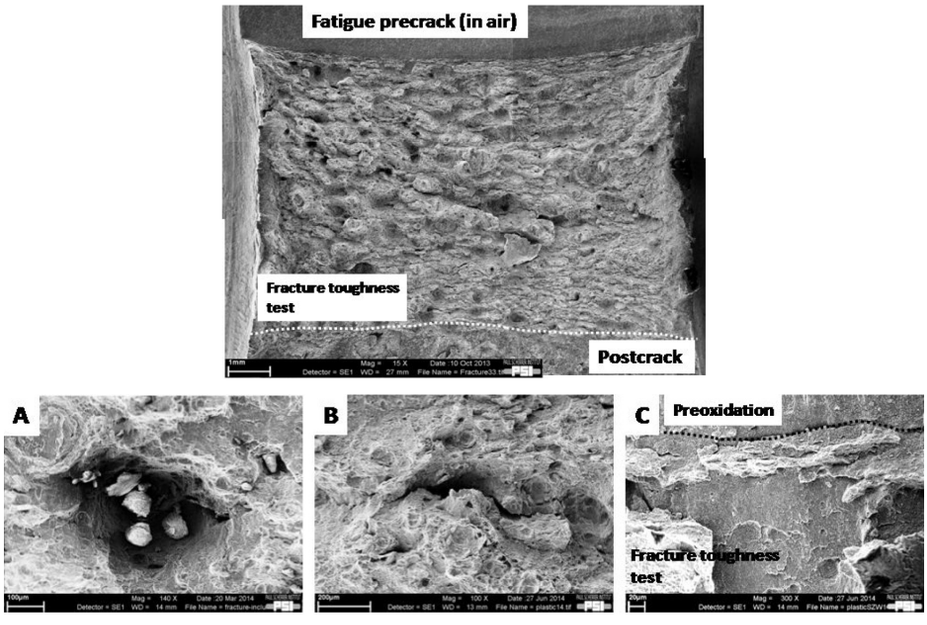

(c)

Figure 16-2: a) typical fracture surface of a 1T-C(T) specimen after a test in BWR simulated conditions. Macrovoids (inset A), quasi cleavage fracture regions associated with inclusions (inset B) and localised flat quasi-cleavage facets (inset C) can be seen, b) ductile secondary cracks and c) typical fracture surface of a 0.5T-C(T) specimen tested in PWR simulated conditions showing macrovoids (inset A), secondary cracks (inset B) and quasi-cleavage (inset C) [Roychowdhury S. et al, 2015].

17 Ferritic steel FAC and other corrosion

Primary water in pressurized water reactors contains boric acid (H_3BO_3) and lithium hydroxide (LiOH). Boric acid corrosion at many PWRs plants has been a concern of utilities for many years because of the large number of potential leakage sources—flanged joints, valve packing, mechanical seals, and fittings. In nuclear power plants, some components such as reactor pressure vessels, piping, valves, pumps, threaded fasteners and other structural parts are constructed with carbon steels and low alloy steels. Such materials are usually not in direct contact with primary water, but could be exposed to primary water when stainless steel or nickel-based alloy corrosion resistant layers fail or as a result of small leaks in valves, fittings, etc. that can cause primary water to come in contact with the external surfaces of carbon and low-alloy steel components. Leakage from piping and pressure vessels has resulted in varying degrees of external corrosion of PWR components. There have been many cases of corrosion of reactor pressure vessel materials by the leaking primary water. EPRI reported some boric acid corrosion issues found in nuclear power plants, summarized the results of previous industry boric acid testing programs, and included a bibliography of related literature. One instance was the discovery of a corrosion cavity (about 127 mm width, about 178 mm long and through the low-alloy steel RPV head up to the stainless steel cladding) in the vessel head at Davis-Besse in March 2002.

A533B and A508III LASs are often used as RPV materials and other key components in nuclear power plants. Several investigators have conducted research studies and presented experimental data on corrosion rates of carbon and low alloy steels in boric acid solutions of varying concentrations and temperatures, aerated or deaerated, and some other test conditions. Argonne National Laboratory measured the electrochemical potential and corrosion rates of RPV A533 steel and A508 steel in boric acid solutions under different operating conditions at temperatures of 95-316°C. The ECPs of all alloys generally decreased with an increase in temperature. The ECP of A533 Gr-B steel increased slightly as the concentration of boric acid in the solution was increased from 3,500 ppm to 36,000 ppm at 95°C. For A533 Gr-B steel, average corrosion rate was ≈40 mm/y in aerated saturated solution of boric acid at 97.5°C and ambient pressure. The corrosion rate in aerated half-saturated solution was ≈2 times lower than that in saturated solution. The rates in deaerated solution were ≈40% lower than that in aerated solution. The effects of boron concentration in conjunction with temperature and aeration on corrosion rates were investigated by Xu H.Q. and Fyfitch S. They found that the corrosion rates of LAS in concentrated boric acid solutions increased sharply with increasing temperature in the range of temperatures tested (21°C to 100°C). The corrosion rate of A533B low alloy steel varied between a few millimeters to tens of millimeters per year at about 97.5°C.

In the reference [Xiao Q. et al, 2015], the effects of solution composition, temperature and dissolved oxygen on corrosion and electrochemical behavior of A508III LAS in boric acid solutions at temperatures from 25 to 95°C were studied by weight loss measurements, electrochemical measurements and surface observations. Studying the corrosion and electrochemical behaviors of low alloy steel in boric acid solutions would be helpful for understanding the fundamental factors and mechanism affecting the corrosion.

The potential-pH (E-pH) diagrams of Fe-H_2O system can be used to analyze the corrosion and electrochemical behavior of A508III steel in the test solutions. The E-pH diagrams of Fe-H_2O system were drawn at 25, 70 and 95°C. The experimental data of solution pH and E_{corr} in aerated solutions were marked at each temperature, as shown in Figure 17-1 to Figure 17-3. The measured E_{corr} values were converted to values against standard hydrogen electrode in the E-pH diagrams. Line (a) was the H^+/H_2 equilibrium line and line (b) was the O_2/H_2O equilibrium line. Oxygen reduction reaction could occur when the potential was located under line (b), and hydrogen evolution reaction could occur when the potential was located under line (a). The position of the boundary line changed with the changing of substances contained in the actual system such as dissolved hydrogen, dissolved oxygen and partial pressure of oxygen or hydrogen. In this study, A508III steel in aerated solutions were mainly located in the zone A for active dissolution and zone C for passivation. For A508III steel in concentrated solutions at 25-95°C, E_{corr} was located in zone A, showing primary active anodic dissolution with hydrogen evolution reaction as the main cathodic reaction. For A508III steel in 1,200 ppm B + 2 ppm Li solution at 25 and 70°C, E_{corr} was located in zone C, showing passivity state. For A508III steel in 1200 ppm B + 2 ppm Li solution at 95°C, E_{corr} was mainly located in Zone C, but occasionally in Zone A. This behavior is an indication of an unstable state of A508III specimen surfaces. This is most probably due to a lower dissolved oxygen concentration at 95°C than those at

25 and 70°C. A low dissolved oxygen concentration decreased the oxide stability, thus made E_{corr} move to zone A in the E-pH diagram for active dissolution. Corrosion rates at each temperature can be explained by E-pH diagram analysis. Increasing the concentration from 1,200 ppm B + 2 ppm Li to 6,000 ppm B + 10 ppm Li shifted the open circuit state from passivity state to active dissolution state, which resulted in the increase in corrosion rates. Increasing the concentration from 6,000 ppm B + 10 ppm Li to 12,000 ppm B + 20 ppm Li caused the acceleration of hydrogen evolution reaction on the electrode surface due to a lower pH, which significant increased the corrosion rates. The emergence of zero-current potentials in the cathodic polarization curves was mainly controlled by multiple elemental electrode reactions. From the E-pH diagrams, E1, in the passive zone, presented a balance between the formation and dissolution of oxidized iron surface. The oxygen reduction reaction on the A508III steel surface as a cathodic process coupled with the anodic dissolution of bare metal gives the second zero-current potential (E2), which could be affected by the dissolved oxygen and temperature. The hydrogen evolution reaction from H+ to H_2 on the base metal surface due to cathodic activation and the active anodic dissolution of iron give the third zero-current potential (E3).

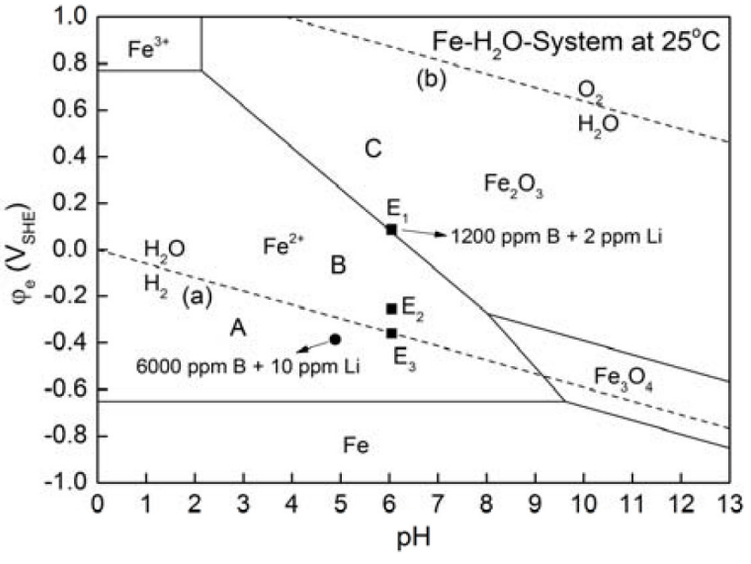

Figure 17-1: The E-pH diagram of Fe-H_2O system and E_{corr} values in aerated solutions at 25°C [Xiao Q. et al, 2015].

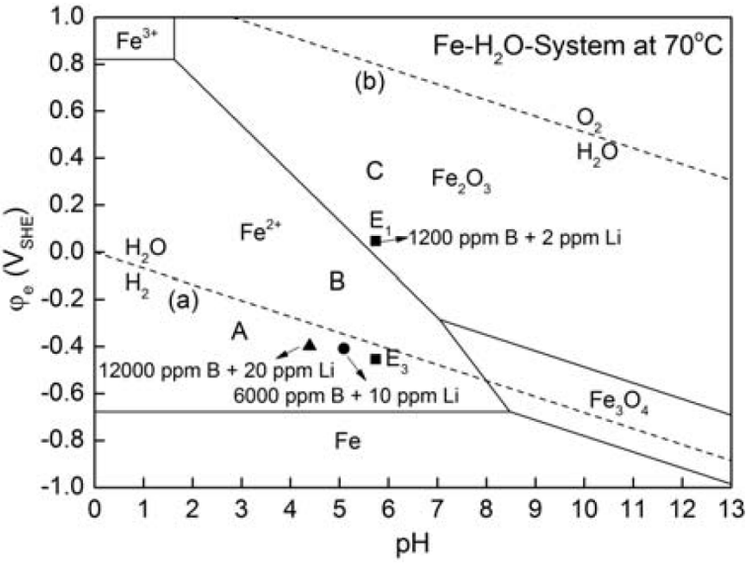

Figure 17-2: The E-pH diagram of Fe-H_2O system and E_{corr} values in aerated solutions at 70°C [Xiao Q. et al, 2015].

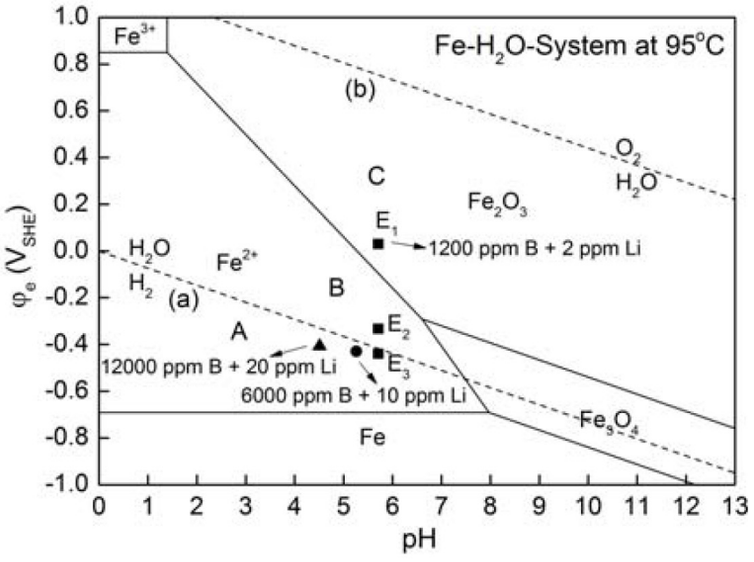

Figure 17-3: The E-pH diagram of Fe-H_2O system and E_{corr} values in aerated solutions at 95°C [Xiao Q. et al, 2015].

In deaerated solutions, increasing temperature effectively accelerated the anodic and cathodic reaction rates, which resulted in an increase of corrosion rate. In aerated solutions, when temperature was lower than 75°C, anodic and cathodic reaction rates as well as corrosion rates all increased with increasing temperature. When temperature exceeded 75°C and continued to rise, dissolved oxygen concentration had a great influence on the protectiveness of the formed surface films. The protective film would mitigate the further corrosion of the base metal therefore reduced the corrosion rates. As shown in Figure 17-4, the corrosion product films formed in aerated solution were compact and uniformly distributed. In deaerated solution, the corrosion products were easily detached therefore led to more severe corrosion of the base metal.

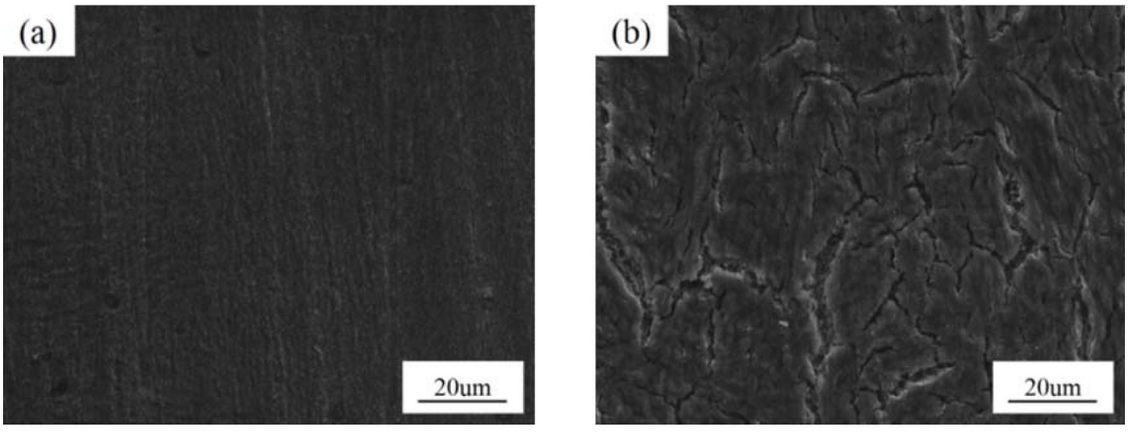

Figure 17-4: SEM micrograph of the corrosion product films formed on A508III steel after immersion in 12,000 ppm B + 20 ppm Li solutions for 24 h at 95°C, (a) aerated, (b) deaerated [Xiao Q. et al, 2015].

During the 2011 refuelling outage at a PWR that had operated since 1987, visual inspection of the channel head of one of the three steam generators revealed defects in the type-308L stainless-steel cladding and apparent attack of the underlying low-alloy steel. The visible degradation comprised six perforations in the cladding on the cold-leg side of the channel head, in the vicinity of the drain line and the "mouse-hole" at the bottom of the divider plate. The configuration of the channel head is shown in Figure 17-5. The largest defect measured 7.5 mm by 14.4 mm, and the total defect area was estimated to be 116 mm^2. Ultrasonic examination of the channel head from the outside indicated extensive wastage of the LAS below the defects. There was a single, irregularly-shaped cavity of maximum depth 28 mm and area 7,350 mm^2. The cause of the cladding defects was not known, but

18 Plant operating experience

There are five key drivers for the aging management of the RV internals: regulatory and licensing (including license renewal and power uprates), reliability and maintenance, inspections, research and development, and component-specific aging management and examination cost reduction. The Code of Federal Regulations, Title 10, Part 54 (10 CFR 54) governs the issuance of renewed operating and combined licenses and requires the demonstration of effective aging management of certain systems, structures, and components so the intended functions will be maintained consistent with the current licensing basis for the period of extended operation. The Code of Federal Regulations, Title 10, Part 50.65 (10 CFR 50.65) provides requirements for monitoring performance or condition of certain SSCs in a manner sufficient to provide reasonable assurance that the SSCs are capable of fulfilling their intended function.

The U.S. PWR industry has proactively developed generic inspection requirements and standards for reactor vessel internals. MRP-227, Rev. 0 was developed after roughly a decade's worth of assessment and predecessor document development and revision 1 of the associated Safety Evaluation Report was completed in December 2011 by the U. S. Nuclear Regulatory Commission. The inspection and evaluation guidelines contained in MRP-227-A consider eight age-related degradation mechanisms: stress corrosion cracking, irradiation-assisted stress corrosion cracking, wear, fatigue, thermal aging embrittlement, irradiation embrittlement, void swelling and irradiation growth, and thermal and irradiation-enhanced stress relaxation or irradiation-enhanced creep. These age-related degradation mechanisms cause aging degradation effects, such as cracking, loss of material, or loss of mechanical closure integrity, for which the program monitors. Component items are grouped as primary, expansion, existing programs, or no additional measures for each nuclear steam supply system design with the appropriate examination method/frequency and examination coverage specified.

For the Babcock and Wilcox designed NSSS RV internals component items requiring augmented examination, 14 are primary component items and 12 are expansion component items. The primary component items are to be inspected according to the examination method/frequency, and coverage requirements described in MRP-227-A. The schedule for expansion component item examination depends on the results of the primary component item examinations; however, the method/frequency and coverage once the onset of examination is required is described in MRP-227-A.

The completed MRP-227-A document contains implementation requirements, including a needed requirement that each commercial U.S. PWR implement the MRP-227-A tables for the applicable design within 24 months following issuance of MRP-227-A. There are two additional needed requirements from this document pertaining to implementation. The first is that examination results that do not meet the examination acceptance criteria defined in Section 5 of the guidelines be recorded and entered in the plant corrective action program and dispositioned. The second is for each U.S. PWR to provide a summary report of all inspections and monitoring, items requiring evaluation, and new repairs to the MRP Program Manager within 120 days of the completion of an outage during which PWR internals within the scope of MRP-227 are examined.

The reference [Davidsaver S.B. et al, 2015] gives the following summary of the MRP-227-A examination results at ONS-3 requiring evaluation, repair, or replacement.

- Three Lower Core Barrel (LCB) bolts with UT indication located in the bolt head-to-shank region.

  Three lower core barrel bolts were found with a UT indication. These same results were identified in an examination performed in 1987. The structural adequacy of the remaining bolts was analyzed based on the stress limits for structural fasteners given in subsection NG of the ASME B&PV Code. The results indicate sufficient margin exists such that the functionality of the LCB and flow distributor assemblies is not impacted and the assemblies are acceptable as-is for continued operation in this condition for the next 10-year inspection interval. A loose parts analysis was also performed to evaluate the effect of the bolt heads of the three LCB bolts with UT indications and their corresponding locking devices becoming loose parts within the RCS and other systems.

- One Flow Distributor bolt with UT indications located in the bolt head-to-shank region.

One flow distributor bolt was found with a UT indication. This same result was identified in an examination performed in 1987. The structural adequacy of the remaining bolts was analyzed based on the stress limits for structural fasteners given in subsection NG of the ASME B&PV Code. The results indicate sufficient margin exists such that the functionality of the LCB and FD assemblies is not impacted and the assemblies are acceptable as-is for continued operation in this condition for the next 10-year inspection interval. A loose parts analysis was also performed to evaluate the effect of the bolt head of the FD bolt with a UT indication and its corresponding locking device becoming loose parts within the RCS and other systems.

- One baffle-to-former bolt with a UT indication located in the bolt head-to-shank region and one uninspectable BF bolt.

  One baffle-to-former bolt was found with a UT indication and one BF bolt was found to be uninspectable due to incorrect seating of the UT probe. The structural adequacy of the remaining acceptable BF bolts, assuming the uninspectable bolt was failed, was analyzed based on the stress limits for structural fasteners given in subsection NG of the ASME B&PV Code. The results indicate sufficient margin exists such that the structural integrity of the core barrel assembly is not impacted and the assembly is acceptable as-is for one fuel cycle. A loose parts evaluation was performed for both BF bolts to evaluate the effect of the bolt heads attached to the locking bar and the locking bars alone becoming loose parts within the RCS and other systems.

- Crack-like indication in the IMI guide tube spider casting leg.

  A crack-like indication was located in one leg of an IMI guide tube spider casting, extending from the top of the casting at the weld toe downward into the casting (see Figure 18-1 for a typical IMI guide tube spider configuration). The structural adequacy of the remaining intact portions of this IMI guide tube spider casting was analyzed based on the stress limits for other than threaded structural fasteners given in subsection NG of the ASME B&PV Code. The results indicate sufficient margin exists such that the functionality of the IMI guide tube spider assembly is not impacted and the assembly is acceptable as-is for continued operation in this condition for the next 10-year inspection interval. A loose parts evaluation was performed for the IMI guide tube spider casting leg to evaluate the effect of the leg becoming a loose part within the RCS and other systems.

- Crack-like indication in the lower grid rib section.

  Although the lower grid rib section is not an MRP-227-A designated component item, the IMI guide tube spider casting leg is attached to the lower grid rib section by welds. As a result, during the examinations of an IMI guide tube spider casting (separate from the above-mentioned spider casting), a crack-like indication was observed in the base metal of the lower grid rib section just below the vertical weld toe (see Figure 18-1 for an example lower grid rib section-to-IMI guide tube spider casting weld). After discovery of this indication, the affected area was brushed using a rotary brush and reexamination took place, however, the indication was still present. Therefore, a fracture mechanics evaluation of the indication, to substantiate acceptability for one fuel cycle, was performed. In this evaluation, the maximum stress intensity factor was calculated and found to be less than half of the lower bound fracture toughness value.

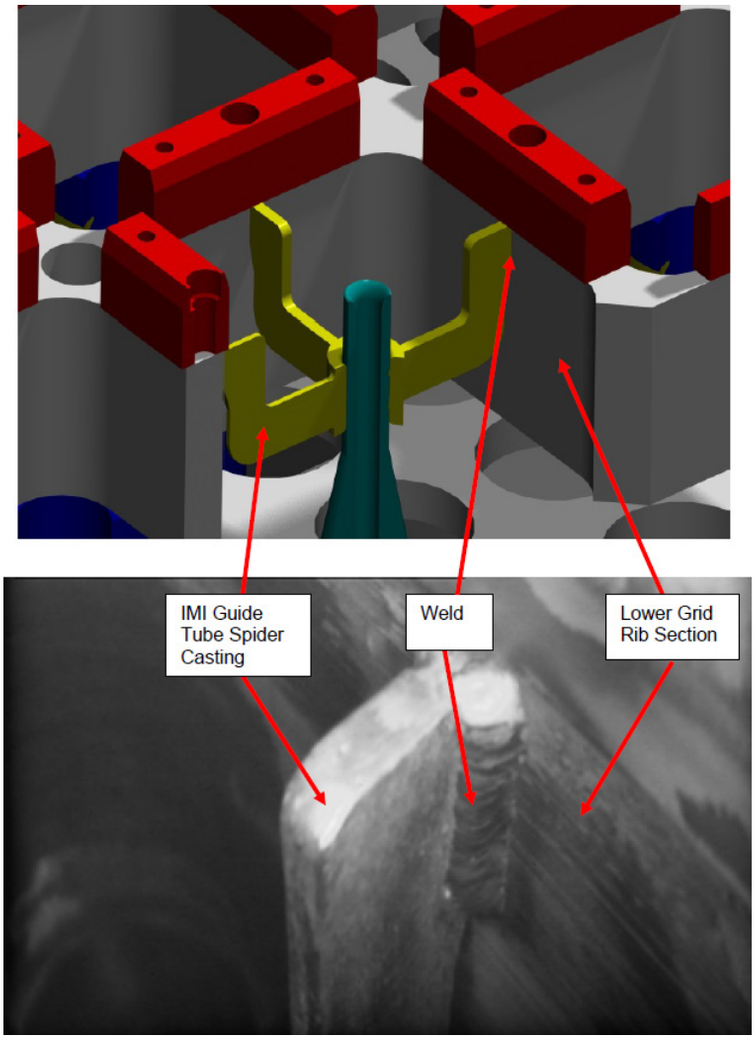

Figure 18-1: Typical lower grid rib section and IMI guide tube spider configuration for B&W-designed PWRs (top), typical lower grid rib-section-to-IMI guide tube spider casting weld (bottom) [Davidsaver S.B. et al, 2015].

- Two core support shield vent valve bodies with gouging.

  Two core support shield vent valve bodies had evidence of new and older gouging at various locations (see Figure 18-2 for a typical vent valve configuration and an example vent valve body guide block). The observed damage is not expected to affect the valve operability since no signs of vent valve asymmetry due to the gouging were seen and therefore, the vent valves were left as-is.

- Core support shield vent valve jackscrew locking crimp cups had crack-like indications on two vent valves.

  Two core support shield vent valve jackscrew locking cups had crack-like indications (see Figure 18-2 for a typical vent valve configuration and an example vent valve locking device). The observed damage is not expected to affect the function of the locking cups or valve operability and therefore, the vent valves were left as-is.

- One core support shield vent valve with a rotated jackscrew pushing locking cup crimps outward and a tilted threaded bushing.

  One core support shield vent valve jackscrew shows evidence of slight rotation pushing the locking cup crimps outward (see Figure 18-2 for a typical vent valve configuration and an example vent valve locking device) and the bushing was found tilted. The observed damage is

not expected to affect the function of the locking devices or valve operability and therefore, the vent valve was left as-is.

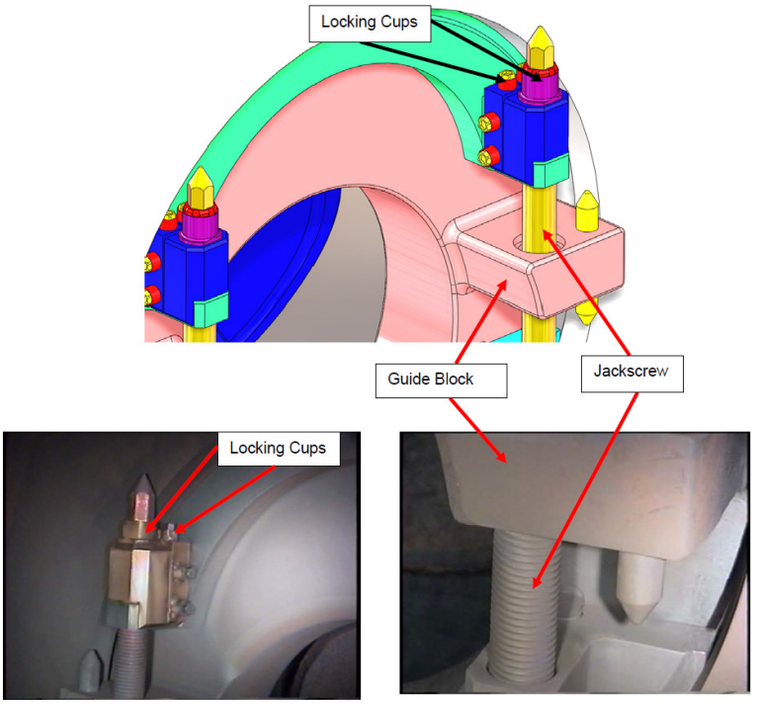

Figure 18-2: Typical vent valve configuration for B&W-designed PWRs (inside view, top), typical vent valve locking devices (bottom left), typical vent valve body guide block and jackscrew (bottom right) [Davidsaver S.B. et al, 2015].

- One core support shield vent valve with incorrect locking device engagement.

  One core support shield vent valve was found to have evidence of incorrect locking device engagement. The jackscrews were verified to be engaged properly and thus the observed damage is not expected to affect the valve operability; therefore, the vent valve was left as-is.

In addition to the details listed above, during performance of the ASME B-N-3 inspections, there were several relevant indications noted. Examples of these indications include foreign material between rows of control rod guide tubes on the plenum cover surfaces, scuffing and gouging on various RV internals surfaces, and a bent control rod guide sector in the control rod guide tube assembly. These relevant indications were dispositioned under the respective examination program at ONS.

During inspections of Babcock & Wilcox 177 type pressurized water reactor units in 2007 and 2009, damaged fuel assembly hold down springs were observed in inspections following two cycle exposures (> 45 MWd/mtU burn-up). The extent of damage varied in each assembly from broken leaf arms to cracked arms with no remaining preload. An example of one of the damaged arms is shown in Figure 18-3. Not all arms in a given HDS assembly were found damaged. Arms in the outermost (top and bottom leaf arms) stacking positions displaying the most extreme damage with little or no damage for subsequent arms near the center of the spring assembly. During the same timeframe, HDS arms from other materials fabrication batches were found to be damage free following PWR operations to two cycles. Two HDS assemblies that displayed damage were retrieved from a PWR spent fuel pool at the end of 2012, and shipped to Oak Ridge National Laboratory. Hot cell examinations of the leaf assemblies were performed followed by disassembly and further inspection of the individual components.

Regions of interest from the leaf springs displaying cracks were sectioned into smaller sample components manageable for examination in the Low Activation Materials Development and Analysis lab for further characterization of mechanical and microstructural properties. Fabricated leaf arms archived (non-irradiated) from the damaged batch (batch A) and from a batch of HDS that exhibited

19 BWR SCC and water chemistry

Thermal aging embrittlement of cast and welded "Austenitic" Stainless Steels for nuclear power plant applications has been extensively studied during the 80´s and early 90´s. The thermal aging leads to an increase in hardness and tensile strength, and a decrease in ductility, impact strength, and fracture toughness. A renewed interest has arisen in recent years for these issues driven by life extension programs and a difficulty in predicting the behavior and microstructure after 60-80 years at reactor temperatures. Cast stainless steels have a duplex solidification microstructure consisting of austenite and δ–ferrite phases. The main aging phenomenon is the thermal diffusion driven decomposition of the ferrite into iron-rich α-phase and chromium-rich α´-phase due to the miscibility gap in the Fe-Cr phase diagram. A maximum rate of decomposition occurs at 475°C, hence the name 475°C-embrittlement. The thermal aging phenomenon of ferritic grades from spinodal decomposition in high temperature applications of 280-500°C is widely known. Research has focused on investigating both binary alloys and commercial grades used in NPPs. An additional contribution to embrittlement comes from the precipitation of G-phase, rich in Ni, Si, Mn, Mo and Ti (ideally $Ni_{16}Ti_6Si_7$), in the δ–ferrite and precipitation and preferential growth of carbides and nitrides at the ferrite/austenite interface. These effects change the material's mechanical properties and to some extent the corrosion behavior, though consensus has not been reached on the magnitude and interaction with mechanical properties.

Studies on cast alloys have revealed that the phase boundary carbides play a significant role in thermal embrittlement at temperatures greater than 400°C, but have insignificant effect on the embrittlement at exposure temperatures below 400°C. Also, aging at 400°C results in spinodal decomposition of the ferrite phase which strengthens the ferrite phase and increases e.g. cyclic hardening. Thermal aging at 465°C results in the nucleation and growth of large α' particles and other phases such as sigma phase, which do not change the tensile or cyclic hardening properties of the material.

The [Bjurman M. et al, 2015] study was conducted on two in-service aged large casting CF8M elbows exposed for 72 kh at 291°C and 325°C, respectively, followed by 22 kh at a reduced service temperature. Atom Probe Tomography was used to characterize the decomposition of the ferrite for both aging states.

The APT analyses of the hot-leg showed clearly the phase separation into α and α' phase, as well as the formation of G-phase precipitates. In the crossover-leg, the microstructural changes are much weaker. The two materials are compared using the radial distribution function, see curves in Figure 19-1. The RDFs represent radial concentration profiles evaluated starting from each detected atom of the specific element. Plots are given as the bulk normalized probability density of finding an atom of the chosen type at radial distance r from each equal atom respectively.

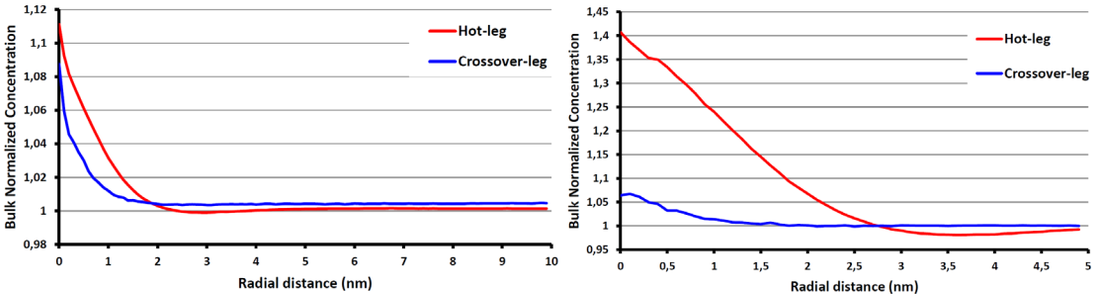

Figure 19-1: Left: Radial density functions of Cr of hot and crossover-legs respectively.
Right: Radial density functions of Ni of hot and crossover-legs respectively [Bjurman M. et al, 2015].

The composition of the three phases was determined for the hot-leg using iso-concentration surfaces. Hence, each volume fulfilling certain compositional criteria is identified and iso-concentration surfaces enclosing these volumes are created. An iso-concentration plot of the hot-leg is presented in Figure 19-2, where a box (37×34×34 nm^3) within the analyzed volume is plotted with red α-, blue α'-, and green G-phase. Atomic maps of projected volumes (20×20×5 nm^3 slices) for the hot-leg and crossover-leg are presented in Figure 19-3 and Figure 19-4, respectively. From Cr-concentrations maps, it is seen

that spinodal decomposition occurs in both hot- and crossover-leg, but substantially less in the crossover leg.

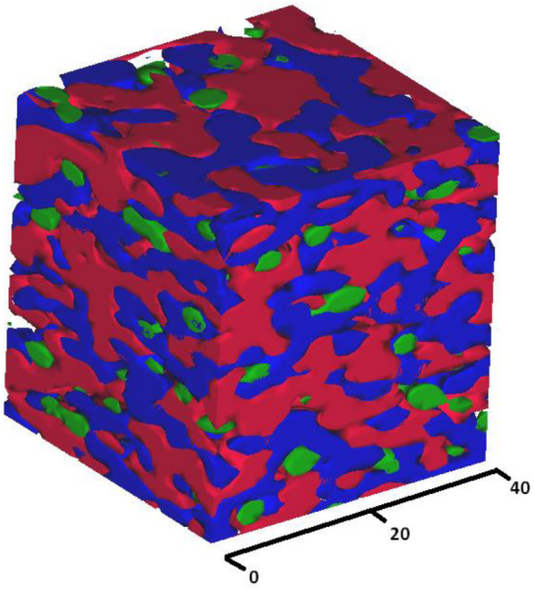

Figure 19-2: ISO-concentration plot of hot-leg with red α-, blue α'-, and green G-phase. The size of the box is 34×34×37 nm^3 [Bjurman M. et al, 2015].

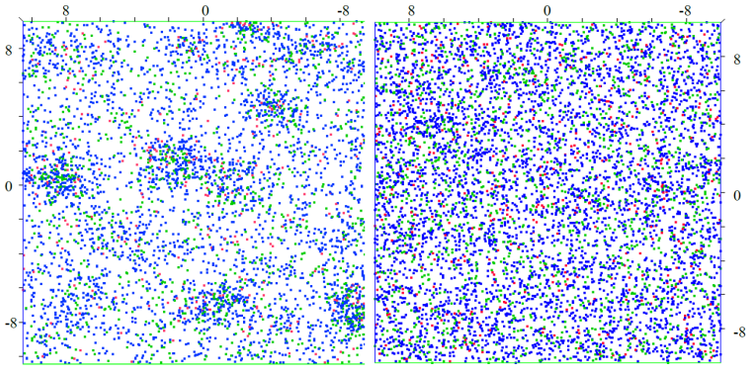

Figure 19-3: Atomic maps of projected volumes (20x20x5 nm slices), left hot-leg and right crossover-leg. Ni (blue), Mn (red), Si (green) [Bjurman M. et al, 2015].

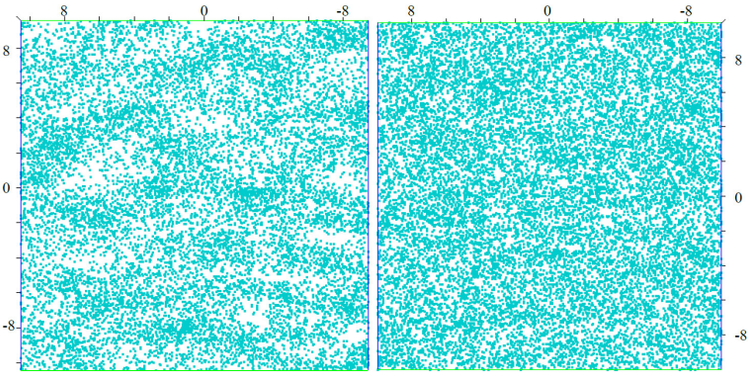

Figure 19-4: Atomic maps of projected volumes (20x20x5 nm slices) of Cr-concentration, left hot-leg and right crossover-leg [Bjurman M. et al, 2015].

The wavelength of the spinodal decomposition of the hot-leg was determined from the Cr RDF curve to 6.8 ± 0.2 nm. The wavelength of crossover-leg is due to the limited decomposition more difficult to quantify, but is estimated to be 4 ± 1 nm. Also the amplitude of the spinodal decomposition was determined to 10.7 at.% for the hot-leg and 8.1 at.% for the crossover-leg, respectively.

The number density of G-phase precipitates in the hot-leg was determined to be $(3.9 \pm 0.5) \times 10^{24}$ m^{-3}. From this value the characteristic distance between precipitates can be estimated as one over the cubic root giving a length of 6.4 nm, which is close to the wavelength of 6.8 nm of the spinodal decomposition. The average diameter of the G-phase precipitates was estimated to about 3.2 nm, and the volume fraction was about 6%. It should be noted that the measurement of average size and volume fraction using APT is less accurate than the measurement of number density, as there is a large influence of the threshold used. In this case the threshold used was Ni+Si+Mn >15 at.%.

From the crossover-leg Ni-Si- and Ni-Mn-RDFs, presented in Figure 19-5, there is a clear positive interaction. In order to estimate the number density, size and composition of clusters in the crossover-leg, an established cluster algorithm was applied. The clustering of Ni, Si and Mn was evaluated using the parameters $d_{max} = d_{envelope} = d_{erosion} = 0.40$ nm and Nmin = 10. The number density of clusters in the experimental dataset was 1.5×10^{25} m^{-3}, compared to the number density of 9.5×10^{24} m^{-3} in a randomized dataset, giving a difference of 5.6×10^{24} m^{-3}. The average cluster contained only 21 atoms, with a maximum of 102 atoms.

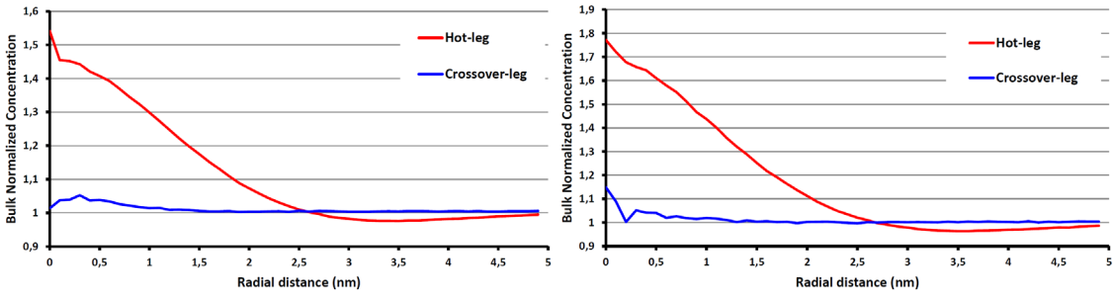

Figure 19-5: Left: radial density functions of Si with respect to Ni as reference point.
Right: radial density functions of Mn with respect to Ni as reference point [Bjurman M. et al, 2015].

The current trend among many operators of Nuclear Power Plants is to operate the plants beyond the originally designed lifetime. The extended service time makes it increasingly important to understand the ageing processes of materials in for instance LWR conditions. IG-SCC plays an important role as one of the most commonly recognized degradation phenomena. IG-SCC is well-known and has been researched for a long time but due to its complicated nature the damage mechanism behind it is still not completely understood. In particular, a coupled fracture mechanic and corrosion model is still not complete, but there exist some models regarding the subject. A model by T. Couvant et al., involving coupling between fracture mechanics and diffusion of oxide. There also exists a model with crack tip mechanics and oxidation kinetics at crack tip by T. Shoji et al. Earlier research on IG-SCC in LWR conditions mostly focused on identifying the material and corrosion behavior trough experiments and parameter fitting equations. The reference [Sedlak M. et al, 2015] is based on a multi-physics model, created to emulate the slip-oxidation mechanisms of IGSCC in LWR conditions, introduced by Ford and Andresen in many of their publications. The assumed mechanism is that exposure to water allows the ions to penetrate along grain boundaries. The rate of penetration is governed by strain, time and ion concentration. The ions are adsorbed at virgin material creating an oxide that weakens the grain boundaries mechanical strength. The boundaries will eventually crack due to the applied stress leaving new virgin material exposed. This process will repeat itself and cracks will grow continuously. The key physical assumptions for the model are:

1. Longer travel distances and smaller gap size makes it more difficult for the ions to reach the crack tip, than for shorter cracks with larger gap size.

2. The oxidation process is non-reversible, ions that are absorbed by the oxide can not go back into the solution.

20 BWR crack growth testing

From the viewpoint of assessing the structural integrity of nuclear power plant components, it is important to prepare crack growth rate reference curves based on reliable SCC growth rate data. There are several standards or guidelines pertaining to the specimens and methods for SCC growth tests, e.g., ISO 7539-6. However, there is no standard explicitly for SCC growth tests in a high temperature water environment such as the primary water system of light water reactors, and the precautions for testing in such an environment are not described. In response to this need, the nuclear subcommittee of the Japan Society of Corrosion Engineering has developed a standard of the test method for measuring the SCC growth rate in high temperature water that simulates the primary water environment of light water reactors. In the course of developing the standard, some items have been prescribed based on the test data analysis with technical discussion while related standards and guidelines have been referenced and accepted. This standard applies to austenitic steels and alloys (including weld metals, heat-affected zones, cold-worked materials and precipitation-hardening steels and alloys). Basic items, such as the specimen, test equipment, test procedure, and evaluation method, are specified in the text of the standard. Several items have been discussed based on experimental data and actual conditions experienced in the primary water systems of light water reactors. For example, the water chemistry conditions at the testing for BWR and PWR are set up precisely taking into consideration the primary water environments of actual nuclear power plants. Also, the crack growth rate is determined according to several criteria, such as crack engagement, crack extension in the tested environment and ratio of maximum crack length to average crack length. Supplementary items, such as the guideline for crack length measurement by potential drop method, basic specifications of test equipment and environmental precrack introduction, are specified in the appendices of the standard. The reference [Itow M. et al, 2015] presents an outline of the standard.

The paper contains:

- Terms and definitions;
- Scope of the standard;
- Principle of test;
- Specimen for test (specimen position and direction, specimen geometry, size requirement of specimen, specimen finish and dimensional measurement, stress intensity factor K_I, precrack introduction);
- Test equipment;
- Test method (installation of specimen, terminals for crack length measurement, and electrodes for corrosion potential measurement, adjustment of test water chemistry, introduction of environmental precrack, test load (basic procedure, optional procedures));
- Crack growth test;
- Evaluation of the test results (crack length measurement and evaluation, crack growth rate determination, K_I determination, validity criteria of crack growth rate);
- Other items.

In the course of developing the standard, some items have been prescribed based on the test data analysis with technical discussion while related standards and guidelines have been referenced and accepted. Basic items such as test equipment, test procedures and evaluation method are specified in the appendices. Also, the standard is accompanied by an explanatory document describing the background and technical basis, etc. The standard is going to be published in the near future. This standard will be revised based on technological progress and improved knowledge.

Specimen thickness requirement is one of major technical issues in establishing the standard test method for measuring SCC growth rate for no-irradiated austenitic alloys and steels in high temperature water environment of light water reactors (BWR and PWR). The working group for SCC

growth test studied the specimen size effect on SCC growth rate to define a specimen size requirement in the standard. Stress-strain conditions near the crack tip of SCC in actual components such as nozzles, pipes and core shrouds are supposed to be small scale yielding with plain-strain conditions. Stress-strain conditions near the crack tip in CT specimen depend on specimen thickness, crack length, ligament length, load and yield stress of material.

A specimen size requirement for plain strain condition is defined in the ASTM standard of E399 for plain-strain fracture toughness test as follows;

Eq. 20-1:
$$B, a > \beta \left(K/\sigma_y \right)^2$$

Where;

B : specimen thickness (m)

a : crack length (m), K : stress intensity factor ($MPam^{0.5}$).

σ_y : yield stress at test temperature (MPa).

β : factor relating to specimen thickness and crack length, $\beta = 2.5$ is defined in the ASTM E399.

Crack length range is defined as $0.45 \leq a/W \leq 0.55$ in the E399. Where, W is specimen width. Specimen ligament length, b is ligament length defined as W-a, thus, b is also defined in the Eq. (1) indirectly.

A specimen size requirement for small scale yielding condition for ligament area is defined in the ASTM standard of E647 for fatigue crack growth rate measurement as follows;

Eq. 20-2:
$$b \geq 4/\pi \left(K_{max}/\sigma_y \right)^2$$

Where, K_{max}: maximum value of stress intensity factor in loading cycles ($MPam^{0.5}$).

Ligament size requirements corresponding to stress-strain condition in ligament area are defined in the ASTM E647 and E399. The requirement in the ASMT E647 is for growing crack, while the requirement in ASTM E399 is for crack initiation for cleavage crack. The requirement in the ASTM E647 is seemed to be suitable for SCC growth test. Working group of SCC growth test adopted the requirement in the ASTM E647 and defined the requirement for small scale yielding condition as follows;

Eq. 20-3:
$$b \geq 4/\pi \left(K/\sigma_y \right)^2$$

The specimen thickness requirement of ASTM E399 described in Eq. (1) is often applied for SCC growth test conveniently. Flow stress, σ_f is usually used instead of σ_y for the strain-hardening materials such as stainless steels and Ni base alloys. And effective thickness, B_{eff} defined as following equation is usually used instead of B for side-grooved specimen.

Eq. 20-4:
$$B_{eff} = \sqrt{B \cdot B_{net}}$$

Where, B_{net}: specimen thickness at the bottom of side grooves.

Andresen investigated K and specimen size effect on crack growth rate of irradiated, cold worked and unirradiated stainless steels and concluded as follows. There is little fundamental justification for using the criteria in ASTM E647 in Eq. (2) for SCC test. There is a sound basis for using σ_f in conjunction with the E399 criteria in Eq. (1). The use of flow stress in not justified for cold worked materials. His investigation backs up the use of σ_f in conjunction with the E399 criteria. Criteria for irradiated stainless steel were proposed in his paper. But no criteria for unirradiated materials was proposed. Richey et al. investigated the specimen thickness effect on SCC growth rate of alloy 600 in PWR primary water environment. The SCC growth rate data of Alloy 600 obtained at 561 to 633K with 1

to 150 cc-STP/kg-H_2O was used in the study. The SCC rates were normalized to those at 611K with 40 cc-STP/kg-H_2O. Then the relationship between normalized crack growth rates and parameter relating to crack tip constraint of $(K / \sigma_y)^2/B_{eff}$ was investigated. The parameter of of $(K / \sigma_y)^2/B_{eff}$ is equivalent to reverse number of β in Eq. (1). Crack growth rates were not affected by $1/\beta$ when $1/\beta$ was not greater than 2. Acceleration of normalized crack growth rate were observed at $1/\beta$ greater than 2. Therefore, they proposed that β in Eq. (1) can be decreased to 0.5. The working group of SCC growth test in JSCE investigated effect of $1/\beta$ on SCC growth rates by a similar way in the Richey 's study for stainless steels, Ni base alloy base metal and weld metals in BWR and PWR water environment to define the β in JSCE standard. The reference [Arai T. et al, 2015] describes the study of this working group defining the specimen thickness requirement.

Upper bound values of $1/\beta$ with no $1/\beta$ dependency of da/dt_{normal} and corresponding β of each material/environment combination are summarized in Table 20-1. The values of β for all of the material/environment combinations were smaller than 0.5 in Richey's study except 182 weld metal, Alloy 600 HAZ in BWR condition and cold worked stainless steels in PWR primary water condition. The values β of 182 weld metal in BWR environment and cold worked 304 and 316 stainless steels in PWR primary water environment were larger than 0.5, although the values these material/environments were smaller than $\beta = 2.5$ in the ASTM E399 validity condition. The value of β of Alloy 600 HAZ in BWR was little greater than 0.5. Applicability of $\beta = 0.5$ to 182 weld metal in BWR environment and cold worked 304 and 316 stainless steels in PWR primary water environment could not be confirmed due to lack of the crack growth rate data at the β range between 0.5 and the values in the Table 20-1. The σ_y of cold worked stainless steel is usually enough large to satisfy the $\beta = 2.5$ in the ASTM E399 validity condition with 0.5TCT or 1TCT specimen. The relaxation of validity condition does not seem to be important issue for this material practically. While, the applicability of $\beta = 0.5$ to 182 weld metal in BWR environment remains as an open item. The working group of SCC growth test will evaluate again if the new data was obtained.

Table 20-1: Upper bound values of $1/\beta$ with no $1/\beta$ dependency of da/dt_{normal} and corresponding β of each material/environment combination [Arai T. et al, 2015].

Environment	Material	$1/\beta$	β
BWR	Sensitized type 304	3.1	0.32
	Type 316L	3.1	0.32
	Alloy 600 HAZ	0.7	1.43
	Alloy 182	1.9	0.53
PWR	Alloy 132 and Alloy 182	2.4	0.42
	Alloy 600MA	2.9	0.34
	Cold worked type 304 and 316	1.4	0.71

In SCC growth calculations to determine inspection intervals or to evaluate the structural integrity of plant components with known cracks, the crack propagation only during full power operation period is considered referring SCC growth rate disposition curves in codes and standards. In other words, the crack propagation during shutdown period is usually considered to be negligible. This common assumption seems based largely on the extensive investigations conducted in late 70s on cracking issues in BWR pipes made of austenitic stainless steels. Summarizing the survey of plant experiences, NUREG-1061 vol. 1 concludes that "All BWR Types 304 and 316 piping systems operating at temperatures over 93°C have shown susceptibility to IGSCC", implying that SCC susceptibility is practically low at temperature below 93°C.

NUREG-0313 rev.2 specifies that Ni-base alloys should be evaluated "on an individual case". However, investigations of plant experiences to date is not necessarily sufficient to reasonably demonstrate that Ni-base alloys have little susceptibility to SCC at lower temperature. Although some laboratory evaluations of temperature effect on SCC have been conducted mainly using Alloy 600 base metal, the majority of those evaluations focus on higher temperature range of >100°C. Limited numbers of data obtained at lower temperature below 100°C show noticeable crack growth rate,

21 Low temperature corrosion and waste storage

Nuclear power plants continue to replace above-ground carbon steel pipe (bare or lined) with more corrosion resistant alloys for various reasons. Galvanic coupling of the carbon steel and CRA piping, even after an insulating flange has been installed between the two metals, continues to be an issue. One plant example involved a design modification to remediate cavitation after a throttling valve. The modification replaced a short section of carbon steel pipe that contained a flow control orifice plate upstream of a butterfly valve with a similarly configured 6% molybdenum stainless steel (6% Mo) pipe to avoid that metal loss. The above-ground 10-inch fresh water service water system piping provides emergency diesel generator cooling. Both the carbon steel portions and stainless steel portions of the line have multiple pipe hangers attached to the concrete walls, ceiling, and floor.

A second plant example involved replacing all above-ground SWS piping, cement lined carbon steel from original construction, with 6%Mo stainless steel for improved corrosion resistance. The below ground pipe will remain cement lined carbon steel with no modifications.

In most cases, like the examples described above, plants connect the dissimilar metals (i.e., the original carbon steel and the new erosion or corrosion resistant material) using flanges and insulating kits (Figure 21-1) to avoid galvanic corrosion at the point of connection and into the original carbon steel piping. In piping systems that are electrically isolated, such an approach works well. However, in nuclear plants, where all buried piping, structures, etc. are commonly grounded, the common grounding can "defeat" the insulating kit, merely changing the shortest electrically conductive path from the shortest distance between the carbon steel and the corrosion resistant alloy to a path through the plant grounding grid.

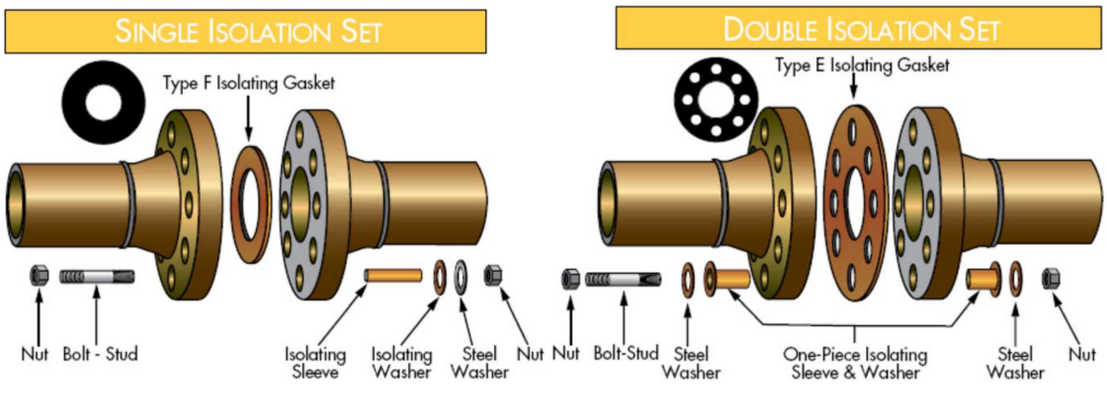

Figure 21-1: Examples of Flange Isolating Kits [Licina G.J. and Jackson H.F., 2015].

The unique design features of nuclear plant piping, including buried piping, has produced galvanic corrosion in above-ground dissimilar metal piping systems despite the installation of insulating kits. The purpose of the guideline ([Licina G.J. and Jackson H.F., 2015]) is to provide examples of designs and design modifications that may be susceptible to galvanic corrosion and that can benefit from installation of appropriate hardware and to provide guidance on selection of insulation or isolation approaches, installation of hardware to avoid galvanic corrosion, and testing and maintenance of those systems.

Insulation kits have their own issues including fragility concerns with the insulators and sealing ability of such flanges.

Power plant experience to date has shown that testing during installation of insulating flanges has been sporadic and that regular testing of resistance values after insulation has been nil.

Unique features of the nuclear plant such as common grounding of all systems and structures can defeat even well installed insulating kits. Alternatives to insulating kits include:

- Completely insulated spool pieces (requires two insulating flanges and no electrical connections between the spool piece and the plant), a length of approximately four diameters;
- Isolation that addresses the ion path rather than the electron path via:
  - Long uncoated metal separators, insulated on both ends;
  - ID coated metal separators (may or may not be electrically insulated on both ends);
  - Coating applied to the ID of the more noble pipe;
  - Lengths of separation provided by the insert pieces will range from two diameters or more in fresh water, with a range from 8 diameters to 60 diameters in seawater; where the required length is driven by the specific dissimilar metal pair and whether the corrosion on the more active metal is general (a shorter length is required) or is localized.

Specific recommendations, shown in decreasing order of preference are:

1. Coated or non-conductive insert (Figure 21-2). The noble member in the galvanic couple (e.g., stainless steel, 6% Mo stainless steel) should be coated: the more active member (carbon steel, coated carbon steel, etc.) should not serve as the coated insert. No insulating flange is required.

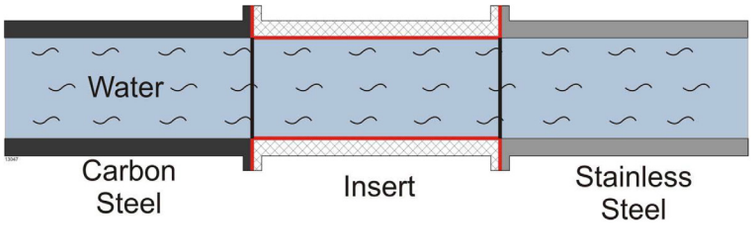

Figure 21-2: Dissimilar metal joint with coated insert spool [Licina G.J. and Jackson H.F., 2015].

2. A spool that is electrically isolated with a properly installed insulating kit on both ends and that has no hangers or other supports to the building (Figure 21-3).

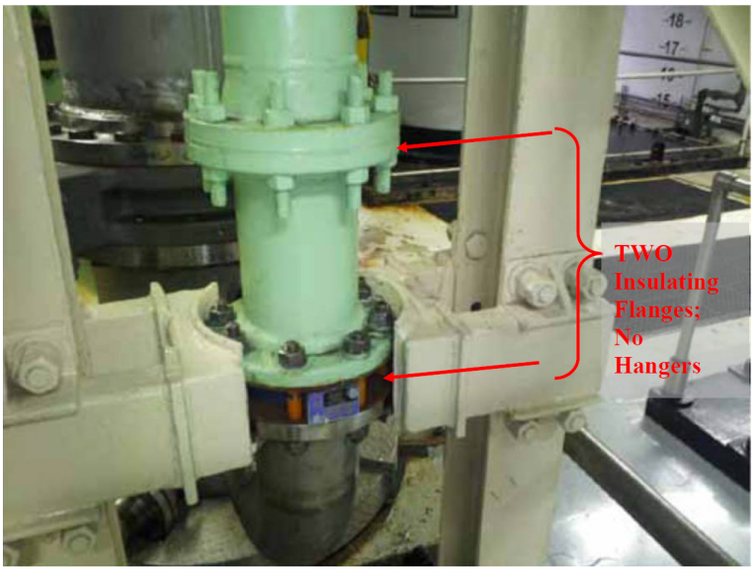

Figure 21-3: Carbon steel/AL6XN dissimilar metal joint: two insulating flanges (carbon steel/carbon steel spool and spool/AL6XN) and no other connections [Licina G.J. and Jackson H.F., 2015].

3. Monolithic isolation joint (Figure 21-4). The required connections to the system will be similar metal welds and no on-site assembly and installation of insulating flanges will be required. However, the monolithic isolation joint will have the exact same susceptibility to being defeated by the common grounding that insulating flanges do. It is also possible to install two monolithic isolation joints (one CS/CS; the other SS/SS); a combination of items 2 and 3.

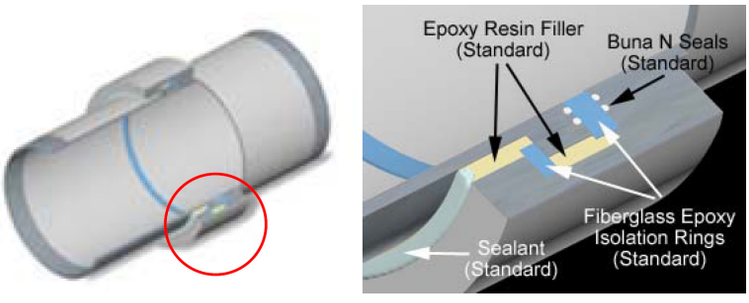

Figure 21-4: Monolithic isolation joint (from www.gptindustries.com).

4. Insulating kits. While this is the legacy approach, difficulties with insulating kits, both with sealing and with achievement or maintenance of high electrical resistance, have been stated regularly by site personnel. Such kits can be difficult to install, are often installed incorrectly, and they can and often will be defeated by the common plant ground.

Beginning in the 1980s, a number of operating and decommissioned reactor sites in the U.S., as well as some other facilities, began to place spent nuclear fuel in dry cask storage systems (Figure 21-5). The U.S. Nuclear Regulatory Commission licenses dry storage of SNF under Title 10 of the Code of Federal Regulations, Part 72 "Licensing Requirements for the Independent Storage of Spent Nuclear Fuel, High-Level Radioactive Waste, and Reactor-Related Greater than Class C Waste." Under the provisions of 10 CFR, Part 72, licenses for specific facilities or Certificates of Compliance for cask systems are typically issued for an initial term of 20 years, after which they may be renewed for additional terms of up to 40 years. When DCSS were initially placed into service in the 1980s, it was anticipated that a permanent geological repository would be available within 20 to 40 years. To date, however, a permanent disposal facility has not been licensed and spent fuel is likely to remain in dry storage longer than was expected. As such, the industry and NRC are addressing issues related to renewal of specific licenses and CoCs, and at the same time, identifying technical information needed to ensure that SNF can be safely stored and transported for extended timeframes.

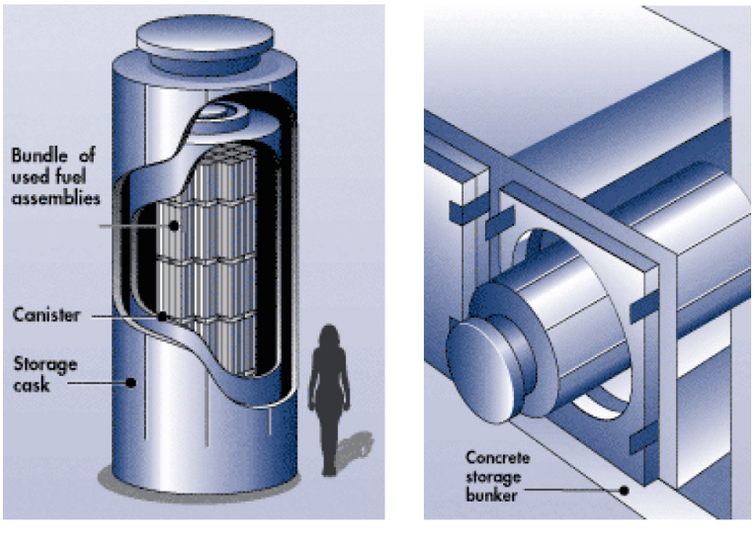

Figure 21-5: Illustrations of vertically oriented (left) and horizontally oriented (right) spent nuclear fuel dry cask storage systems [Oberson G. et al, 2015].

22 Zirconium and fuel cladding

In CANDU power reactors, pressure tubes (Figure 22-1) are manufactured from Zr-2.5Nb and contain the fuel bundles and coolant within the reactor. Each reactor contains 380-480 pressure tubes, arranged horizontally within the reactor (Figure 22-1).

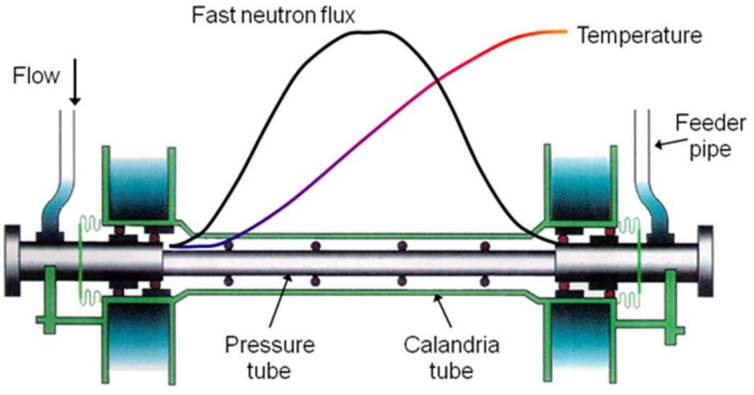

Figure 22-1: Schematic diagram of a pressure tube showing how the neutron flux and the temperature varies along the length of the tube. The inlet temperature is ~250°C and outlet is 310°C. The neutron flux peaks at $4x10^{17}$ n/m^2/s [Nordin H.M. et al, 2015].

Heavy water coolant passes through the tubes at a pressure of 10-11 MPa, temperatures between 250-312°C and a fast neutron flux up to ~$4x10^{17}$ n/m^2/s. These pressure tubes form the primary pressure boundary in the core. A pressure tube is 6 m long, has a diameter of 10 cm and a wall thickness of 4.2 mm. This component is expected to have an operating lifetime of at least 25 years. As part of the Canadian Standards Association fitness-for-service requirements for pressure tubes, flaws or stress risers that potentially lead to cracks can not exist in pressure tubes in operating reactors. Flaws may include: fuel bundle scratches, crevice corrosion marks, fuel bundle bearing pad fretting flaws and debris fretting flaws. These flaws may be a precursor to cracking and must be mitigated or the tube removed if the flaw cannot be suitably dispositioned. This provides protection against pressure tube failure from delayed hydride cracking, and fracture initiation.

A limited amount of fatigue data exists for zirconium alloys. The data in the literature concentrate on fatigue life or crack growth rate tests. Often the effects of environment (such as irradiation and hydrogen content) during these tests are unclear.

The reference [Nordin H.M. et al, 2015] presents the results from the development of a fatigue crack initiation test program on Zr-2.5Nb specimens conducted in heavy water at high temperatures representative of pressurized water reactor operating conditions. Issues encountered during the development and resolution are discussed.

A test facility to perform corrosion fatigue testing on zirconium alloys was developed. Initial testing showed crack initiation could be detected using the PD method. These tests indicated conditions can be reached where there is an interaction between fatigue and hydride cracking. However, the high hydrogen ingress that led to delayed hydride cracking was greater than expected for the corrosion process for a short term exposure under the test conditions. The cause of the high hydrogen ingress was traced to the materials selected as contacts between the MI cables and the zirconium specimen. Due to the high hydrogen permeability of the contacts, they acted as a window for hydrogen absorption into the zirconium specimen. The contacts were changed to TZM as it was an effective hydrogen barrier and was relatively easily spot welded to the specimens. Hydrogen ingress was shown to be greatly reduced using the modified contacts. Corrosion fatigue tests were then conducted at a maximum load of 750 N with R = 0.2 and a load rise time of 1800 s. The results indicated that crack initiation occurred at a reduced number of cycles when compared to the tests conducted in air (Figure 22-2).

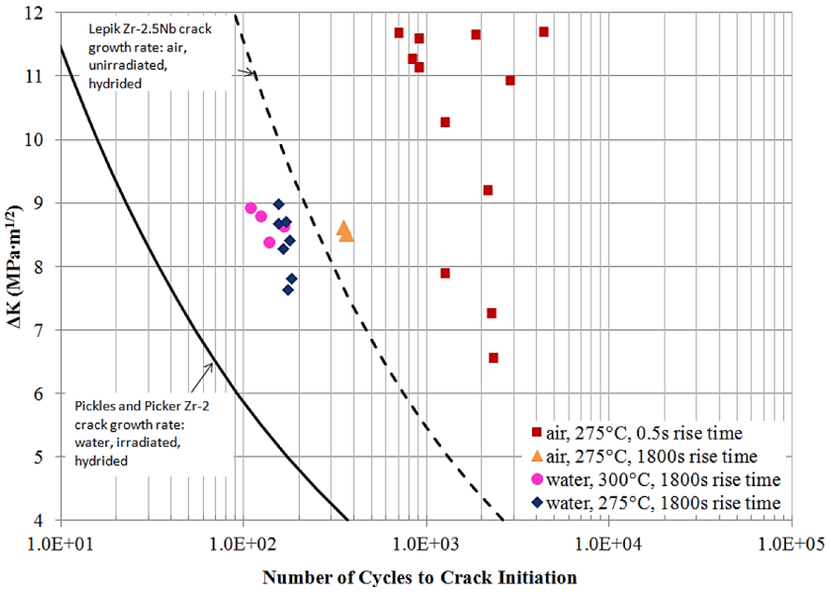

Figure 22-2: Stress intensity versus the number of cycles to crack initiation (15 μm long crack). The graph indicates how results obtained in air fatigue tests compare to the results obtained in high temperature heavy water conditions. The plot also shows crack growth rate curves obtained from tests on unirradiated Zr-2.5Nb in air at 300°C and on irradiated Zircaloy-2 in steam generating heavy water reactor environment conditions at 260°C [Nordin H.M. et al, 2015].

Numerous studies in the last decades were performed to elucidate the particular oxidation kinetic behavior of zirconium alloys. Current trends towards extending bumup, increased outlet temperatures and plant life extension in nuclear power facilities require a better mechanistic understanding of the corrosion behaviour under irradiation. The life limiting factors for Zircaloy-4 in a reactor are normally corrosion and hydrogen embrittlement. Since essentially all of the hydrogen absorbed into the metal was created during the corrosion process, it is critical to understand the role of irradiation on corrosion.

Studies based on in-pile and out-of-pile weight gain data suggest that neutron radiation has a large impact on the corrosion fate of zirconium alloys during in-core service. Garzarolli et al., showed a significant increase in corrosion rate after 5-cycles ofin-core life when comparing in-pile corrosion data to out-of-reactor autoclave test results. Bradhurst et al. observed in-reactor corrosion rates that were ten times greater than those conducted out-of-reactor and attributed the effect of increased corrosion rate to greater permeability of the oxide formed in-reactor. Furthermore, Johnson and Irvin published some data on reactor-exposed Zircaloy-2, showing an increase in the oxide weight gain of 40-fold, with a strong linear dependence on neutron flux. These previous data suggest that displacement damage to the solid during corrosion produces a significantly larger effect than that due to water radiolysis alone. However, the true driving force for such enhanced corrosion remains unclear.

Cheng et al., demonstrated that post-iradiation autoclave exposures of neutron-iradiated Zircaloy-4 shows no significant increase of corrosion rate. By comparing post-irradiation exposure experiment to in-reactor exposure, two major differences can be deduced. First, the displacement damage created in the solid during irradiation can be quickly removed by thermal annealing during autoclave exposure at high temperature. This is very unlike a reactor environment, where damage in the solid can be sustained and accumulated over time as long as the neutron bombardment continues. Secondly, no radiolysis products were generated during autoclave exposure whereas in a nuclear reactor, water radiolysis products are continuously present. Clearly in order io study the irradiation-accelerated corrosion, the two effects, displacement damage and radiolysis, have to be present simultaneously.

The study of the reference [Wang P. et al, 2015] focusses on the characterization of the oxide film formed on Zircaloy-4 that has been exposed to the PWR primary loop environment (without B and Li addition) during proton and electron iradiation. In the proton irradiation study, the material will experience the combined effects of displacement damage, radiolysis of water and electron and hole pair production. However, the electron irradiation will only produce the effects of water radiolysis and

electron and hole pair production. By comparing the two irradiations, the effect of displacement damage can then be isolated.

The following conclusion has been obtained:

Corrosion kinetics of the proton irradiated Zircaloy-4 was strongly affected by irradiation in-situ in 320°C water containing 3 ppm of H_2. Displacement damage caused by higher dose rate proton irradiation produced an oxide l0 times thicker compared to in-pile corrosion rate under PWR dose rate (Figure 22-3).

From observations of the electron irradiated sample and the unirradiated areas of the proton irradiated sample, there is no direct effect of radiolytic radical species on corrosion rate, under the assumption that radiation dose in the water in both cases were similar.

Oxide morphology under proton irradiated exhibited a smaller equiaxed monoclinic ZrO_2 grain structure, while electron irradiated and all the unirradiated oxide maintained its columnar monoclinic ZrO_2 grain structure.

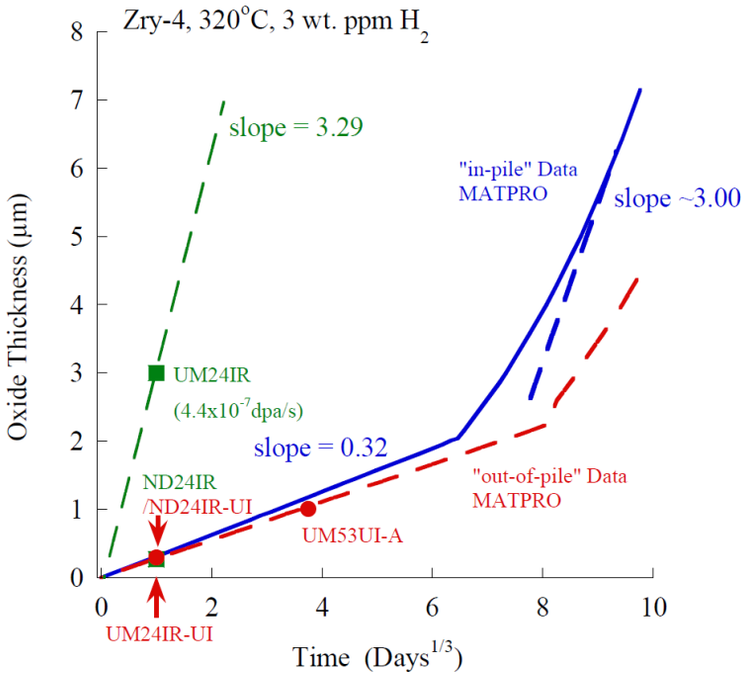

Figure 22-3: Plot of oxide thickness as a function of corrosion time for in-pile and out of pile data and in-situ proton irradiation-corrosion data [Wang P. et al, 2015].

Under accident conditions, such as at Fukushima in 2011, Zr alloys will react rapidly with steam to produce large quantity of exothermal energy and hydrogen at temperatures > 700-800°C, and explosive reaction with oxygen at the fuel cladding surface.

In order to enhance tolerance of fuel to accident conditions, EPRI has developed the conceptual design of an innovative fuel cladding (Figure 22-4). Mo or its alloys have been proposed as an alternate candidate fuel cladding material that may provide several advantages over the current Zr alloys. Mo has been studied for potential nuclear core applications, such as liquid metal cooled fast reactors for several decades because of its high melting point, excellent high temperature strength, good thermal conductivity, and resistance to irradiation-induced swelling. Mo resists oxidation in air at low temperatures, but above ~400°C, Mo oxide may become volatile, causing gradual metal loss. Thus, a protective coating of Zr alloys or Al containing advanced steel alloys (e.g., FeCrAl) has been proposed to protect Mo in water and high temperature steam. Such a thin protective coating of Zr alloy or advanced steel can be formed by physical vapor deposition.

23 Fukushima

Because of the great east Japan earthquake on 11th, March, 2011, Fukushima Daiichi nuclear power plants (1F) were damaged by unprecedented severe accident which included station blackout and core cooling function decline. As an emergency countermeasure for core cooling, seawater was injected. Then, temperature and chloride ion concentration have been decreasing after injection of freshwater and purified water. Although, the RPV and PCV were not supposed to be exposed to dilute seawater, the RPV and PCV have been exposed to such environment. Since such conditions are considered to be continued for more than 15 years before fuel removal, it is required that the structural integrity of the RPV and PCV (Figure 23-1) should be ensured.

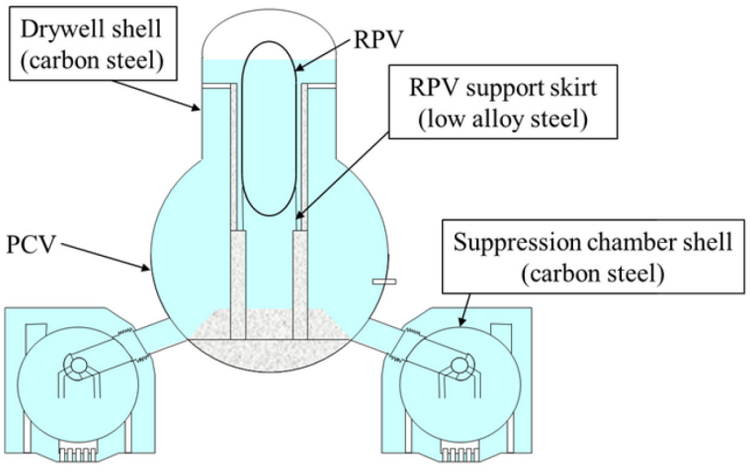

Figure 23-1: Subject equipment for integrity assessment [Kaneko T. et al, 2015].

There are many reports about the corrosion behavior of low alloy steel and carbon steel in neutral environment including chloride ion such as seawater. Kado and Watanabe have reported the influence of temperature on the corrosion of steel in seawater containing dissolved oxygen. According to this report, corrosion rate increases with temperature up to about 353K in an open container, but corrosion rate is going to decrease to a very low value near the boiling point. This may be due to increase in reaction rate with increasing temperature and significant decrease in oxygen solubility at a time. Whitman et al. reported the effects of pH and temperature on the corrosion of carbon steel in water. Corrosion rate of carbon steel shows almost constant in the range of pH4-10. Corrosion rate of carbon steel is increased in acidic range, and is decreased in alkaline range due to passivation. In addition, there is a tendency that the corrosion rate increases with temperature when compared at the same pH. Miyasaka reported the influence of NaCl concentration on the corrosion of cast iron. In this paper, the influence of NaCl concentration on the corrosion rate of carbon steel is small. Honda et al. reported the effect of dissolved oxygen concentration on the average corrosion rate of carbon steel. The corrosion rate is increased with dissolved oxygen concentration. Thus, the individual factors to affect corrosion of steels have been studied to some extent and may be roughly used for corrosion evaluation of components made of steels. However, since the corrosion data have large variation and synergetic effects of such factors on corrosion behaviors of steels are not well known, it is difficult to evaluate corrosion loss of the RPV and PCV in 1F specific condition with sufficient accuracy under the actual condition from the present knowledge. Therefore, in order to evaluate the structural integrity of the RPV and PCV in consideration of corrosion loss in the core cooling water environment in 1F, it is necessary to evaluate the corrosion behaviors of related materials in a simulated actual environment.

The purposes of the reference [Kaneko T. et al, 2015] are to investigate corrosion behaviors of low alloy steel and carbon steel in the 1F cooling water simulated environment. In addition, preliminary attempt evaluation of structural integrity of the RPV and PCV equipment in 1F is performed in consideration of corrosion behavior of these materials.

The results of the surface observation on the low alloy steel and carbon steel specimens in the medium-term condition (1000 ppm Cl^-, 353K) for before test and after 500 h are shown in Figure 23-2. As

shown in Figure 23-2 (c) and (d), the entire specimen surface of each low alloy steel and carbon steel was covered with corrosion products. The difference in the surface condition of each material was little. It was considered that corrosion form of low alloy steel and carbon steel was general corrosion.

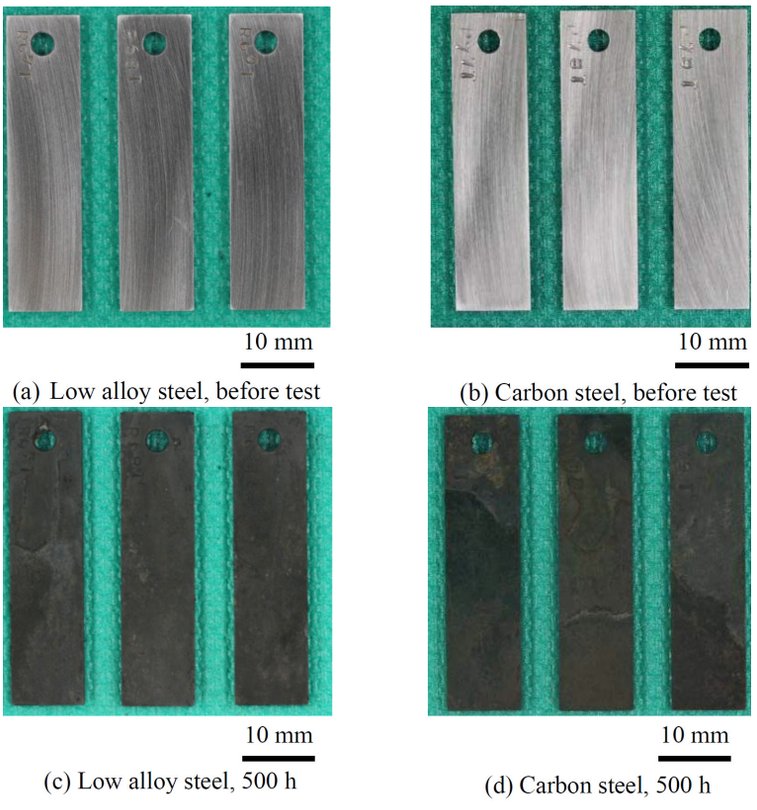

Figure 23-2: Result of appearance observation before and after immersion corrosion test in 1000 ppm Cl^-, 353K (medium-term) [Kaneko T. et al, 2015].

Figure 23-3 shows the relationship between mass loss and testing time in the medium-term condition (1000 ppm Cl^-, 353K) and the long-term condition (100 ppm Cl^-, 323K). The mass loss due to general corrosion of low alloy steel and carbon steel was increased with time. In addition, the mass loss of long-term condition was reduced when compared to the medium-term condition. Therefore, the reduction of corrosion rate is expected by mainly performing the cooling of the RPV and PCV in 1F. Although 1F is an irradiated environment, the immersion corrosion tests in this study were carried out on non-irradiated condition.

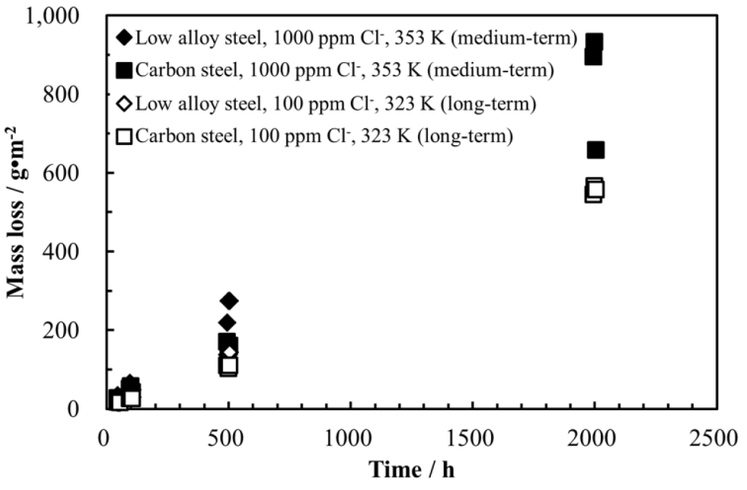

Figure 23-3: Immersion corrosion test results of low alloy steel and carbon steel in medium-term and long-term condition [Kaneko T. et al, 2015].

Nakano et al. reported the weight loss in the steels with a 200 Gy/h dose rate were comparable with those without irradiation. In addition, the result of dose measurement inside of PCV at 1F-2 was up to 72.9 Gy/h. The influence of radiation on the corrosion behavior of low alloy steel and carbon steel is mainly attributed to generation of the hydrogen peroxide accompanying the radiolytic decomposition of water. Since the test solution was aerated, it is considered that corrosion behavior of low alloy steel and carbon steel under non-irradiation environment is similar to that under irradiation environment.

For recriticality prevention, injection of borate such as $Na_2B_{10}O_{16}$ and H_3BO_3 was performed after the accident in 1F. Therefore, in order to evaluate the influence of borate on corrosion behavior, corrosion tests with borate were performed under the medium-term condition. The influence of borate on the corrosion behavior of low alloy steel and carbon steel is shown in Figure 23-4. As compared with the medium-term condition without borate, the mass loss increased about 3-4 times with H_3BO_3 addition, and it was considered that general corrosion occurred from the surface morphology of specimen. On the other hand, when $Na_2B_{10}O_{16}$ was added, the mass loss of low alloy steel and carbon steel decreased about one half. From the result of surface observation, it was considered that the specimen surface was passivated and localized corrosion was occurred. Thus, it was considered that the reduction of mass loss with $Na_2B_{10}O_{16}$ addition due to surface passivation. In the neutral borate solution, it is known that carbon steel is passivated easily. Ohba et al. reported that passive region was observed from the result of anodic polarization measurement in boric-borate buffer solution of pH 8.45. Nishimura and Sato reported that boron was presented in the precipitation film which formed at neutral pH borate solution, and the passive film exhibited anion permeability. Also, Tokunaga reported that the precipitation film consisted of complex of ferric iron such as $Fe(OH)(BO_2)_2$ and $FeOHB_4O_7$. Generally, it is known that breakdown of passive film caused by chloride ion occurred easily in the case of the anion permeable film rather than the cation permeable film. Therefore, while corrosion prevention by passivation is expected by the addition of as $Na_2B_{10}O_{16}$, there is a possibility that localized corrosion occurs.

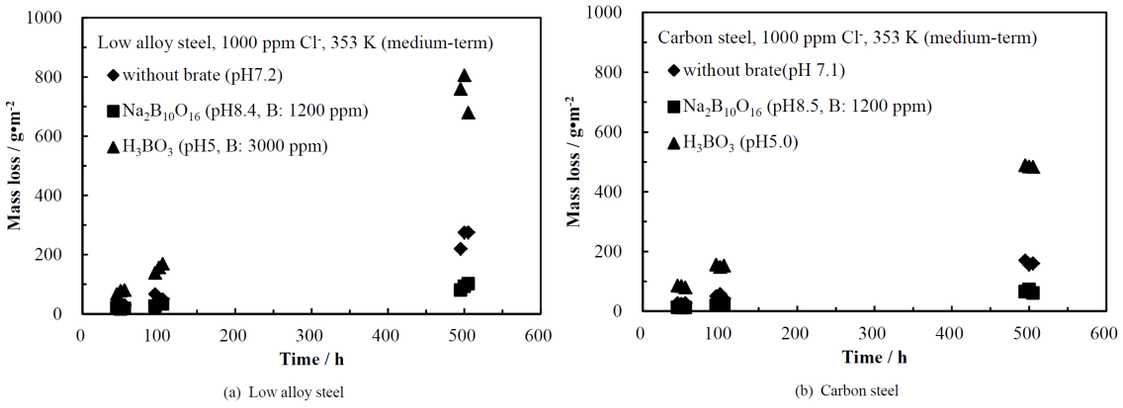

Figure 23-4: Influence of borate on the corrosion behavior of low alloy steel and carbon steel [Kaneko T. et al, 2015].

The surface photograph of carbon steel after the corrosion test in the long-term condition (100 ppm Cl^-, 323K) with nitrogen deaeration is shown in Figure 23-5 left. The specimens surface was changed color to light brown. It was considered that the specimens were covered with thin surface film. The time dependence of the mass loss with and without nitrogen deaeration is shown in Figure 23-5 right. As compared with the conditions without nitrogen deaeration (aerated long-term condition), the significant decrease in mass loss was observed in each test materials in the case of nitrogen gas deaeration. Because measurement results of dissolved oxygen concentration with nitrogen deaeration were 0.1 to 0.3 ppm, it is considered that this result has been attributed to cathodic reaction rate which was decreased remarkably. For this reason, it seems that nitrogen deaeration is effective in corrosion suppression.

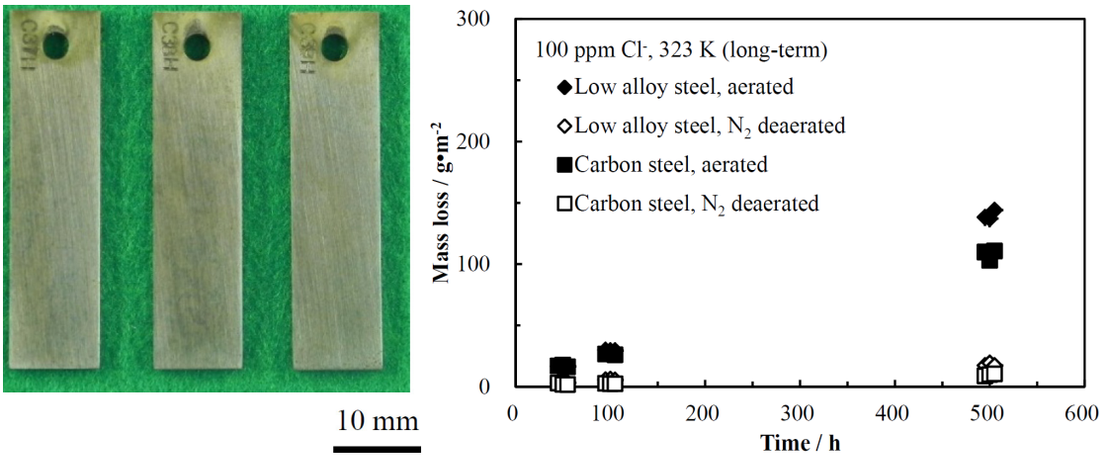

Figure 23-5: Left: result of appearance observation after corrosion test (500 h) in 100 ppm Cl^-, 323K (long-term) with N_2 deaeration. Right: effect of nitrogen deaeration on the corrosion behavior of low alloy steel and carbon steel [Kaneko T. et al, 2015].

As a result of performing preliminary attempt to estimate the structural integrity, in consideration of the plate thickness reduction by corrosion (Figure 23-6) and the load calculated by the earthquake response analysis for the standard seismic ground motion *Ss* under the condition of the PCV filling with water, the equipment of RPVs and PCVs in 1F unit 1, 2 and 3 has the potential to maintain the structural integrity in more than 15 years after the accident.

24 Supercritical water corrosion

Concerns with greenhouse gas emissions and uncertainties in the long-term supply of fossil fuels have resulted in renewed interest in nuclear energy as an essential part of the energy mix for the future. Current generation nuclear reactors (often referred to as Generation II and Generation III reactors) are not considered to be sufficiently efficient to guarantee a long-term sustainable energy supply. In an effort to improve nuclear plant efficiency, an international collaboration known as the Generation IV International Forum (GIF) was initiated to develop GEN-IV reactor technologies to improve reactor efficiency, safety, sustainability and proliferation resistance. One of the six technologies selected by the GIF is the Supercritical Water-Cooled Reactor, which represents the logical evolution of the current generation of water-cooled reactors that supply the majority of the electricity generated by nuclear. The various SCWR concepts currently being developed utilize single-phase supercritical water as the coolant, which will increase the thermodynamic efficiency to about 45% (as compared to 33% for current light water reactors), and is expected to provide considerable plant simplification. In the current Canadian SCWR core concept, a high pressure (25 MPa) inlet plenum feeds water into the core through 336 vertical fuel channels containing the nuclear fuel. The coolant enters the core at a temperature of 350°C. The fuel channel outlets are connected to an outlet plenum; the outlet coolant temperature reaches ~625°C. The outlet plenum connects to the high-pressure turbine via a main steam line.

The main difference between the LWR and the SCWR is the water phase, while in the first one the water exists as liquid, in the SCWR, water is in the supercritical region which appears above the critical point (374ºC, 22.1 MPa). Operating with water to the supercritical region has a number of advantages: water is a familiar and relatively safe heat transfer medium used by many power utilities under operation so there is a lot of information about its behavior as coolant and about its interaction with structural materials. Secondly, the supercritical water (SCW) is in one phase inside the supercritical region, this situation simplifies the design of the SCWR and avoids some problems of the Boiling Water Reactors where the water is in two phases inside of the vessel: liquid water and steam. Furthermore, the SCW has a high thermal enthalpy, this means there is an optimum heat exchange between the fuel and the coolant. In spite of these good properties, some features of the SCW raises questions about the behavior of the SCW as coolant that have not been answered so far. It is well known that the physicochemical properties of water changes sharply with pressure and temperature inside the supercritical region. According to some works found in the literature, these changes in the physicochemical properties of water could imply that water behaves more like liquid or like gas depending on pressure and temperature. However, other authors support the idea that supercritical water behaves as liquid water at higher temperature, suggesting a common corrosion mechanism in both phases. On the other hand, Guzonas and Cook have pointed out that, at temperatures above about 500°C, corrosion issues in superheated steam and SCW are very similar.

The identification of appropriate materials for in-core and out-of-core components to contain the SCW coolant is one of the major challenges in the design of the SCWR. Ferritic-martensitic steels (e.g., HT-9, T91, T92, and HCM12A), austenitic stainless steels (e.g., 304, 304L, 316, 316L, 310), and iron-based oxide dispersion strengthened alloys have all been considered as candidate materials for both the fuel cladding and other components exposed to the SCW coolant. It has been proposed that a Zr-modified 310 austenitic stainless steel can be considered as potential fuel cladding material for the SCWR concept; this alloy was observed to have good general corrosion resistance up to 600°C. Precipitation-hardened and solid solution Ni-based alloys (e.g., IN718, IN625) have also been considered for SCWR applications, particularly where the radiation dose is lower. Nickel-base alloys in general exhibit better corrosion resistance in SCW than ferritic-martensitic and austenitic stainless steels, and have enhanced creep resistance at higher operating temperatures; however, nickel-based alloys are not suitable for use in the reactor core due to their high neutron absorption cross-sections and greater susceptibility to radiation damage than iron-based alloys.

For the Canadian SCWR concept, the peak cladding temperature is forecast to be as high as 800°C. There have been no reported test results for materials under SCW condition and at elevated temperature (near 800°C). In order to ensure safe operation of Canadian SCWR, corrosion and stress corrosion evaluation of various candidate materials must be carried out at the proposed reactor peak temperature. As no known test facility exists to test materials in supercritical water at temperatures above 650°C and 30 MPa, the use of superheated steam as an equivalent fluid for corrosion testing has

been proposed. The objective of this preliminary study ([McClure P. et al, 2015]) is to test 310 stainless steel in two corrosive environments, supercritical water and superheated steam at 600°C to determine whether these environments can be used interchangeably in testing the corrosion behaviour of materials.

Figure 24-1 shows 310 samples before and after exposure to supercritical water (600°C, 29 MPa) and superheated steam (600°C, 0.1 MPa) for varying durations. After 100 hours of exposure in SCW samples became a dull gray. The difference in appearance between samples exposed for 100, 200, and 300 hours was not significant, with little change in colouring or lustre as exposure time was increased. This suggests that the oxide film was formed in the early stage of the test and remained stable andprotective during extended exposure.

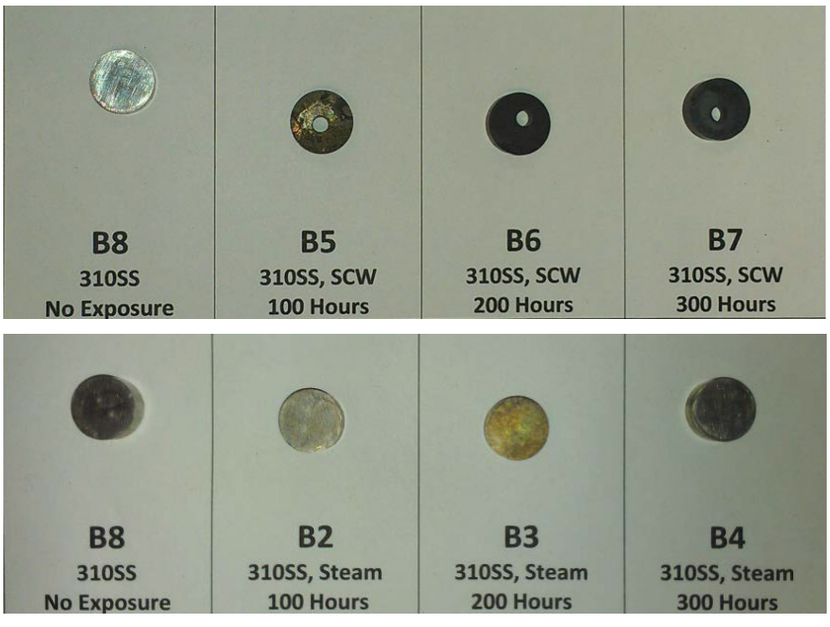

Figure 24-1: Visual inspection of samples exposed to supercritical water for 100 to 300 hours (top) at 600°C, 29 MPa and (bottom) 600°C, 0.1 MPa [McClure P. et al, 2015].

The samples were weighed before and after testing, showing a weight gain after exposure to both supercritical water and superheated steam due to the formation of oxides on the exposed surfaces. On the average, the SHS led to higher weight change to 310 samples than SCW. More specifically, 310 samples tested under SCW show a small initial weight gain that remains fairly constant as exposure time increases. This suggests that an oxide surface layer may have formed after 100 hours and this layer remains stable throughout the testing. The degree of the weight gains for the superheated steam tested samples is greater on the average; however, reduced weight gain measured after 300 hours' exposure is seen, i.e., there was weight loss between 200 to 300 hours. This suggests a possible oxide layer dissolution or spallation in SHS. As the SHS test was conducted in two batches, the first one for 100 hours and the second batch for 200 hours. The sample tested for 300 hours was in both batches and went through heating and cooling cycles twice; the thermal cycles may have caused oxide to spall. Furthermore, the test rig for SHS test has a flow rate of 1 - 2 kg/hour creating a dynamic condition (vs. static condition in autoclave) which could also contribute to surface scale removal. Despite possible scale removal in SHS, the averaged weight gain is greater than that that experienced in SCW.

SEM/EDS analysis was performed on samples exposed to supercritical water (600°C, 29 MPa) for varying durations. Figure 24-2 shows surface features of AISI 310 samples exposed to supercritical water for durations of 100, 200 and 300 hours. Formation of small spherical particles was observed on the surface of the sample after 100 hours of exposure to the supercritical water. This was consistent across the surface of the sample. These particles are varying in sizes and loosely distributed on the surface. The samples exposed for 200 hours showed similar features as that exposed for 100 hours. This is in agreement with the visual inspection and weight gain analysis, which suggested that the AISI 310 samples formed a stable oxide layer soon after being exposed, and did not exhibit significant

change in oxide formation as exposure duration increased. Similar results were found for the sample exposed to supercritical water for 300 hours.

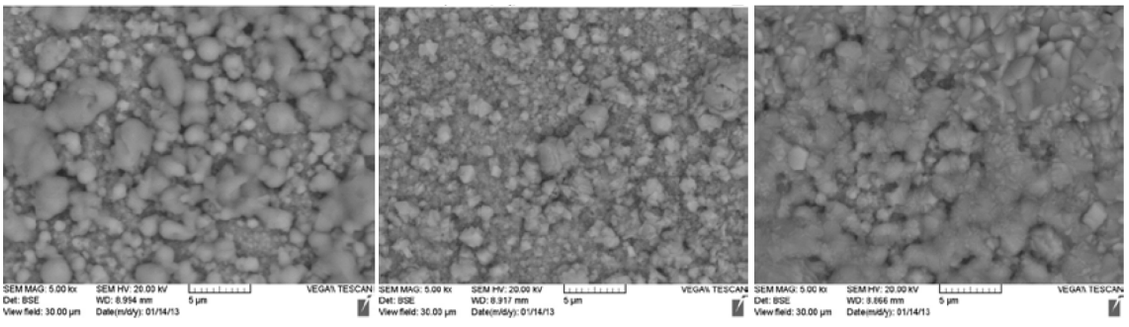

Figure 24-2: SEM images of AISI 310 exposed to SCW (600°C, 29 MPa, 100 hrs) [McClure P. et al, 2015].

SEM/EDS analysis was performed on 310 samples exposed to SHS (600°C, 0.1 MPa) for durations of 100, 200 and 300 hours. SEM images of AISI 310 exposed for 100, 200 and 300 hours are given in Figure 24-3. After 100 hours of exposure to superheated steam, some evidence of very fine oxide scale formation is visible; however, the particle size is less than the sample exposed to supercritical water. After 200 hours of exposure to superheated steam, signs of oxide scale formation are clearly present. This is consistent with the weight gain results, which suggest that significant oxide formation occurs after 200 hours of exposure. After 300 hours, the surface does not seem to be covered with the same oxide on the sample tested for 200 hours. Also, there is an indication of more surface pitting.

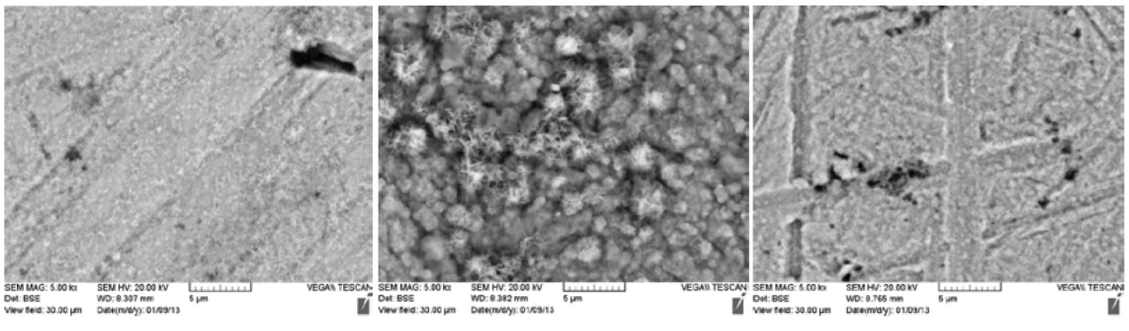

Figure 24-3: SEM images of AISI 310 exposed to SHS (600°C, 0.1 MPa), left: 100 hours, middle: 200 hours and right: 300 hours [McClure P. et al, 2015].

From this preliminary study, it is found that SHS, a dynamic environment with open loop flowing steam, has resulted in higher weight change to 310. This is consistent with work done by Ruther and Greenberg, who found corrosion in dynamic tests, such as these superheated steam tests, was 1.5 times higher than that in the static tests, such as the supercritical water tests. The difference in oxidation behaviour for samples exposed to the supercritical water and to the superheated steam also suggests that further test for longer duration will be needed to establish a clear understanding of the surface oxide formation and dissolution/spallation in high temperature SCW and SHS.

Based on the literature review, there is no single alloy that currently has demonstrated satisfactory performance to enable it to be used for fuel cladding or components transporting fluid in Canadian SCWR where a temperature as high as 800°C is predicted. Performance is defined by maximum allowable scale thickness increase per year, metal loss (after descaling) per year or the occurrence of large cracks. To further complicate the design process, there has no known test facility exists to test materials in supercritical water at temperatures above 650°C and 30 MPa; the use of superheated steam as an equivalent fluid for corrosion testing is therefore proposed. Two candidate materials IN 625 and A-286 are evaluated in the reference [Garcia R. et al, 2015] by exposing them to subcritical and supercritical water and also to superheated steam to study effects of steam pressure/density on material's corrosion behavior.

Samples were weighed before and after exposure. The dissolution of surface oxides in the fluid may cause weight loss while oxide formation and deposition of dissolved substances in the fluid during cooling in the autoclave, could lead to weight gain. There are also possibilities of sealant contamination to the samples tested in autoclave. Sample cleaning process may further remove loose oxide particles from the surface. As such, weight change should only be used in the screening stage of material testing. All calculations of weight change are with respect to sample's initial weights before testing. The bar graph in Figure 24-4 shows the influence of test conditions on weight change of all samples exposed for 1,000 hours.

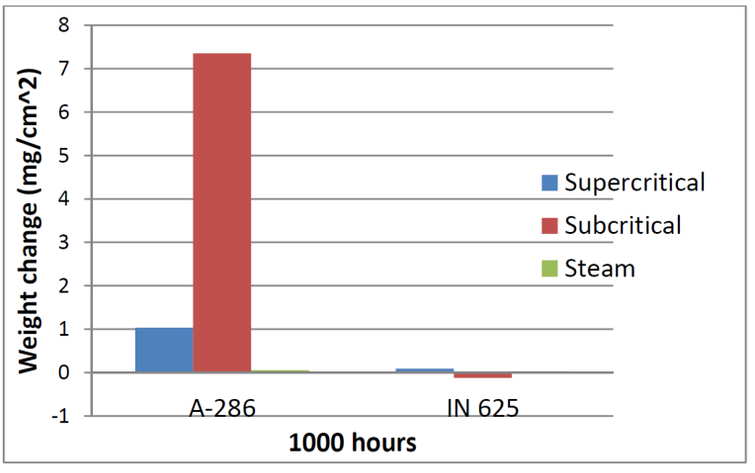

Figure 24-4: Bar graph of weight change mg/cm^2 vs. test condition for all samples tested for 1,000 hours [Garcia R. et al, 2015].

The IN 625 samples experienced very little weight change overall, with slight weight gain in the supercritical test and weight loss in the supercritical condition. While the limited weight gain signals thin layer of oxide formation on the surface, weight loss can be a cause for concern if dissolution or spallation of material affects the working fluid. A-286 suffered much greater weight change in supercritical water as shown in Figure 24-4. Even greater weight gain was observed in the subcritical test condition. Very minimal weight changes occurred in the superheated steam condition. According to these results, it seems that alloy (IN 625) with higher Cr content is not affected substantially by the change in water/steam conditions. While low Cr content in A-286 might be responsible for the elevated weight gain under subcritical condition.

Figure 24-5 provides SEM images of A-286 samples exposed to supercritical water at 625°C and 29 MPa for 1,000 hours. It shows that after 1,000 hours in SCW A-286 alloy has developed islands of corrosion produce that covers more than 50% of the surface area. The morphology of the oxide is similar to iron oxide seen on AISI 304. The oxide particles have a similar pattern in all areas where it can be found. They have a random orientation and irregular/angular shapes. EDS measured base metal composition in the matrix area, except slightly elevated oxygen.

25 Posters

25.1 Corrosion behavior of platinium treated type 304 stainless steels in oxygenated pure water environments ([Yeh T.K. et al, 2015b])

As the boiling water reactors age, incidents of intergranular stress colrosion cracking and irradiation-assisted stress corrosion cracking are more readily seen in the vessel internals. The technology of hydrogen water chemistry has been widely adopted in BWRs around the world to mitigate the problem of stress corrosion cracking in the structural components. To further improve the corrosion mitigation effrciency of HWC, a noble metal treatment on the structural components may be adopted for catalyzing the recombination of hydrogen and the oxidizing species in the reactor coolant. During the practice of HWC, hydrogen injection is not placed into service until the reactor power exceeds 30% of the rated power. The reactor coolant, which usually contains high levels of dissolved oxygen due to intrusion of atmospheric air in the cold shutdown period, could remain relatively oxidizing during a startup operation. Accordingly, as the reactor is being started up, the elecfrochemical corrosion potential of a structural component would be relatively high in the oxygenated water environment. More importantly, in the absence of hydrogen during a startup operation, a noble metal treated component would in theory experience an even higher ECP, due to the catalyzed reduction reaction of oxygen.

In this study, the ECP of Type 304 stainless steel treated with platinum was investigated in oxidizing water environments at various temperatures of 250°C and 288°C via electrochemical polarization analyses. The ECPs and corrosion current densities of both untreated and Pt-treated samples were analyzed. In pure water environments with 300 ppb dissolved oxygen at the two selected temperatures, the ECPs and corrosion current densities of the Pt-treated samples were greater than those of the untreated ones. It was also found that the exchange current density of the oxygen reduction reaction on the treated sample was more than two times greater than that on the untreated one. In addition, the catalytic efficiency of Pt decreased with decreasing temperature in oxidizing water environments. A noble metal treatment would result in a comparatively more severe corrosion behavior of the treated components under plant startup condition in the absence of sufficient dissolved hydrogen.

25.2 Investigation of the impact of coatings on the corrosion of nuclear components ([Daub K. et al, 2015])

Structural reactor components are prone to degradation and, for advanced reactor concepts, the proposed operating temperatures are higher than in curent reactors, which is expected to lead to enhanced degradation. To improve the performance of some components, coatings may be applied and used for: hardening of surfaces, protection against wear, protection against corrosion, reduction of tritium diffusion, reduction of hydrogen ingress, and electrical insulation. commercially available coatings such as CrN, AlCrN, and TiAlN + AlCrN were applied by physical vapour deposition to obtain 3-5 micrometres thick coatings on substrates of AISI 3l6L stainless steel. The corrosion resistance of these coatings was investigated under pure water at 350°C for 24 hours and under CANDU® reactor primary-side conditions (300°C and $pH_{25°C}$ 10.5 LiOH) for up to 120 days. The coated surfaces were analyzed by scanning electron microscopy before and after the testing of the samples, with additional transmission electron microscopy analysis on a limited selection of samples. The relative compositions of the coatings were determined by energy dispersive X-ray spectroscopy and the in-depth distributions of elements throughout the coatings were determined by secondary ion mass spectrometry.

25.3 The SCC behavior of alloy 82/low alloy steel dissimilar metal weld in the fusion boundary region in a simulated primary water environment ([Xu J. et al, 2015b])

The present work focused on the SCC behavior of Alloy 82/LAS dissimilar metal weld in the fusion boundary region in simulated primary water reactor primary water environments and

the time domain analysis was applied to illustrate the threshold for the crack growth rate under which the crack can be arrested by the fusion boundary. It is found that 10-10 m/s seems to be the threshold for retarding crack propagation. However, even if the crack had penetrated into the low alloy steel, it will not likely propagate further in the low alloy steel under constant load condition.

25.4 Characterization of pre-transition oxides formed on zirlo™ ([Bae H.Y. et al, 2015])

Corrosion of zirconium fuel cladding is known to limit the lifetime and reloading cycles of the fuel in nuclear reactors. Oxide layers formed on ZIRLO™ cladding samples after immersion for 300-hour and 50-day in a simulated primary water chemistry condition (360°C and 20 MPa) were analyzed by using the scanning transmission electron microscopy, in-situ transmission electron microscopy with the focused ion beam technique, and x-ray diffraction. It is interesting to note that both samples (immersion for 300-hour and 50-day) revealed the presence of the ZrO sub-oxide phase at the metal/oxide interface and columnar grains developed perpendicularly to the metal/oxide interface. Voids and micro-cracks were also detected near the water/oxide interface while relatively large lateral cracks were found just above less advanced metal/oxide interface. Equiaxed grains were mainly observed near the water/oxide interface.

25.5 Fuel surveillance results from the first TiO_2 application in a BWR plant ([Takagi J. et al, 2015])

TiO_2 injection technology has been developed as an intergranular stress corrosion cracking mitigation countermeasure for BWR plants and was successfully applied during the course of plant shutdown at the Unit-1 of Fukushima-Daini Nuclear Power Station of Tokyo Electric Power Company in 2010. The TiO_2 chemical was injected to the primary coolant system in order to deposit TiO_2 onto the structural materials to prevent IGSCC. The TiO_2 deposition amount onto the structural materials and the fuel rods were measured during the following maintenance outage period. The oxide thickness of the fuel cladding with TiO_2 pre-coated one cycle before the application was measured and turned out to be within an allowable range.

25.6 Mechanisms of crud deposition in pressurised water nuclear plant ([Johnson N. et al, 2015])

Experience from nuclear plants suggests that large build-up rates of CRUD are found at the entrance to flow restrictions, such as those found at the entrance to steam generator tubes. The build-up of these deposits causes reductions in heat transfer efficiency and local chemistries that significantly differ from the bulk. The deposition process also influences the manner in which radioisotopes, such as ^{60}Co, are incorporated into the oxide layers.

The process by which deposits are made on reactor surfaces is not well understood, although one of the most developed theories attributes deposition to electrokinetic phenomena associated with the linear acceleration of the flow disturbing the electrical double layer at the flow restriction. The accumulation of positive ions at the restriction entrance promotes anodic reactions, such as the oxidation of iron (II) in the coolant stream.

The aim of this project is to use a rig representative of plant geometry to investigate the deposition rate as a function of water chemistry and flow rate, alongside experiments determining the release rate of metallic cations into primary water. Of particular interest is the zeta potential at the steam generator tube entrance, which is to be investigated and measured at high temperature and flow-rates, by measuring the streaming current under the short circuiting condition. In combination with corrosion release rate experiments for different materials and surface finishes, this project aims to gain a mechanistic understanding of the electrokinetically stimulated deposition process, and hence a suitable mitigation strategy.

25.7 Corrosion fatigue and scc behavior of 316LN in high purity and boron/lithium water ([Du D. et al, 2015])

The corrosion fatigue and stress corrosion cracking property of primary piping 316LN stainless steel was characterized in different water chemistry. Crack length was measured by the direct current potential drop method and crack growth rates were calculated in different water chemistries. We found that the fatigue crack growth rates were closely related to loading model with the less aggressive R and lower frequency each decreasing the crack growth rate. Stress corrosion crack growth rates of 316LN were significantly affected by dissolved gas. 316LN has the highest crack growth rate in boron-lithium water when 2 ppm oxygen was dissolved in the water. No cracking difference was found in different water chemistries when hydrogen was dissolved into the water.

25.8 Grain boundary characterization for initial stage of igscc of alloy 600 in PWR primary water environment ([Jung K.T. et al, 2015])

Three-dimensional characterization of IGSCC of Alloy 600 in a simulated primary side water of PWR was performed using SEM/EBSD observation. IGSCC susceptibility of Alloy 600 was evaluated with different dissolved hydrogen of 0.5, 2.75 ppm and tensile elongation rate of 5, 10%. After the SSRT test, the specimen was polished from top of surface to approximately into 2 μm in depth. By comparing the SEM images before and after polishing, grain boundary inside of materials was characterized. Crystal orientation analysis of the specimen was performed using EBSD configured to FE-SEM. It is revealed that Σ3 coincident site lattice grain boundary occupied more than approximately 80% of grain boundaries with misorientation angle of around 60 degrees. The crack probability of coincident site lattice grain boundaries depends on the character, that is, the highest at Σ27 grain boundary compared with Σ9, Σ3. It is to be noted that actually no crack occurs at Σ3 grain boundary. In terms of crack angle that is defined at the angle between grain boundary plane and load axis, the specimen at dissolved hydrogen of 2.75 ppm and tensile elongation rate of 5% indicated high susceptibility of IGSCC at misorientation angle between 30 and 40 degrees. It is suggested that susceptibility of IGSCC in the initial stage is influenced by the characteristics and stress condition at grain boundary.

25.9 Properties of the oxide films on Ni-Cr-xFe alloys in simulated PWR water environment ([Ru X. et al, 2015])

The oxide films formed on Ni-Cr-xFe alloys in simulated PWR primary water environments simulating normal operating conditions and abnormal conditions were characterized by scanning electron microscope, focused ion beam, transmission electron microscope, X-ray diffraction and laser Raman spectroscopy. Iron in Ni-base alloys has a strong effect on the surface morphologies of the oxides formed in the oxygenated PWR primary water, which does not significantly affect the surface morphologies of the oxides formed in the hydrogenated PWR primary water. Ni was concentrated in the oxide films formed in the oxygenated PWR primary water, but depleted in the oxide films formed in the hydrogenated PWR primary water. Cr-depletion was significant in the oxide films formed on Ni-base alloys in the oxygenated PWR primary water, which was not significant in the oxide film formed in the hydrogenated PWR primary water. Increasing the Fe content in the alloy, more and

more needle-like oxides appeared in the outer layer of oxide films formed in the oxygenated PWR primary water. The needle-like oxides consisted of a lot of nano-sized iron oxides. The inner layer of oxide films formed in the oxygenated PWR primary water mainly consisted of cellular oxides. The center of cellular oxides was Ni rich whereas Cr was concentrated at the boundaries.

25.10 Effects of hydrogen in alloy 690 on interfacial reaction kinetics ([Xia X. et al, 2015])

The effects of charged hydrogen on mechanical properties and electrochemical behavior of Alloy 690 in aqueous solutions such as simulated PWR primary water or bicarbonate solutions at relatively low temperatures were studied. Hydrogen-charging was achieved by galvanostatically cathodic polarization in an acidic solution. Open circuit potential, anodic polarization curves, electrochemical impedance spectroscopy and potentiostatic polarization of non-charged and hydrogen-charged Alloy 690 specimens were measured. Charged-hydrogen had a significant effect on electrochemical behavior for Alloy 690 in bicarbonate solutions. Charged-hydrogen could cause a negative shift of open circuit potential. Anodic current densities of hydrogen-charged specimens were generally higher than those of non-charged Alloy 690 at potentials before the first transpassivation potential. Electrochemical impedance of hydrogen-charged Alloy 690 was significantly lower than that of non-charged one. Hydrogen in Alloy 690 tended to accelerate the interfacial reactions through enhancing anodic dissolution or decreasing the protectiveness of the surface film. Similar effects of charged hydrogen on electrochemical behavior of Alloy 690 in simulated PWR primary water at 25 and 70°C were observed, where the effect of hydrogen on anodic polarization curve could extend to higher potentials than those in bicarbonate solutions. The effect of temperature on electrochemical behavior was investigated.

25.11 Progress in assessment of non-destructive techniques for evaluating the state of aging cables in nuclear power plants ([Fifield L.S. and Ramuhalli P., 2015b])

Electrical cables used for power, control, instrumentation and communication represent key components of existing nuclear power plants. It is important for operators to be able to determine the status of installed cables in ways that minimize disruption of power generation and do not destroy the cables in the process. Environmental stress on nuclear power plant cables that can lead to degradation of cable performance over the long operational life of the plants includes radiation, heat and moisture. Continued operation of existing plants over periods greatly exceeding their original forty years of qualified life will require effective non-destructive methods for monitoring cable condition and for appraising cable remaining useful life. We present an update of the ongoing assessment of non-destructive nuclear cable evaluation technologies at the Pacific Northwest National Laboratory supported by the Light Water Reactor Sustainability program of the U.S. Department of Energy Office of Nuclear Energy. (PNNL-SA-111465).

25.12 Effect of water chemistry on oxidation behavior of β-Nb precipitates in Zr-Nb-0.2Bi alloy ([Yao M.Y. et al, 2015])

In order to understand the mechanism of the accelerated effect of LiOH on the corrosion of Zr-Nb alloy, Zr-Nb-0.2Bi alloy was adopted for corrosion test in deionized water and in lithiated water with 0.01 M LiOH at 360°C/18.6 MPa. Focused ion beam milling technique was used to prepare the cross-sectional sample of oxide film for the microstructural observation. High resolution transmission electron microscopy with X-ray energy dispersive spectrometer was applied to analyze the microstructure of oxide film and the oxidation behavior of second phase precipitates. This study focused on the oxidation of β-Nb precipitates, considering the fact that the major second phase precipitates in Zr-Nb alloy are β-Nb. From the high resolution transmission electron microscope observation and the analysis for the oxide layer, it is found that the corrosion rate and corrosion products of β-Nb precipitates are different in various water chemistries. Exposed in deionized water at

References

Abe H. (1), Yano T. (1), Miyazaki T. (1), Watanabe Y. (1), Fujiwara K. (2), Yoneda K. (2) and Inada F. (2), *Characterization of oxide film formed in flow accelerated corrosion of carbon steels and its relationship to thinning rate*, (1) Graduate School of Engineering, Tohoku University 6-6-01-2 Aoba, Aramaki, Aoba-ku, Sendai, 980-8579 Japan, (2) Central Research Institute of Electric Power Industry 2-11-1 Iwadokita, Komae, Tokyo, 201-004 Japan, Proceedings of the 17th International Conference on Environmental Degradation of Materials in Nuclear Power Systems-Water Reactor, Ottawa (Canada), 2015.

Ahmedabadi P. and Was G.S., *Stress corrosion cracking of proton irradiated Alloy 33 for accident tolerant fuel cladding*, Nuclear Engineering & Radiological Sciences, University of Michigan, Bonisteel Boulevard, Ann Arbor, MI 48109, USA, Proceedings of the 17th International Conference on Environmental Degradation of Materials in Nuclear Power Systems-Water Reactor, Ottawa (Canada), 2015.

Ahonen M. (1), Ehrnstén U. (1), Saukkonen T. (2), Todoshchenko O. (2) and Hänninen H. (2), *Factors affecting low temperature crack propagation (LTCP) susceptibility of nickel-based Alloy 182, 82, 152 and 52 weld metals*, (1) VTT Technical Research Centre of Finland Ltd, P. O. Box 1000, FI-02044 VTT, Finland, (2) Aalto University School of Engineering, P. O. Box 14200, FI-00076 Aalto, Finland, Proceedings of the 17th International Conference on Environmental Degradation of Materials in Nuclear Power Systems-Water Reactor, Ottawa (Canada), 2015.

Alexandreanu B., Chen Y., Natesan K. and Shack B., *Stress corrosion cracking of a 52M weld overlay in a PWR environment*, Argonne National Laboratory, Nuclear Engineering Division, 9700 S. Cass Avenue, Argonne IL 60439, USA, Proceedings of the 17th International Conference on Environmental Degradation of Materials in Nuclear Power Systems-Water Reactor, Ottawa (Canada), 2015a.

Alexandreanu B., Chen Y., Natesan K. and Shack B., *Stress corrosion cracking of Alloy 152 weld butter near the low alloy steel interface*, Argonne National Laboratory, Nuclear Engineering Division, 9700 S. Cass Avenue, Argonne IL 60439, USA, Proceedings of the 17th International Conference on Environmental Degradation of Materials in Nuclear Power Systems-Water Reactor, Ottawa (Canada), 2015b.

Andresen P. (1) and Carter R. (2), *Development and analysis of an Alloy X-750 SCC growth rate database,* (1) GE Global Research Center, One Research Circle, CE2513, Schenectady, NY 12309, (2) Electric Power Research Institute, 1300 Harris Blvd, Charlotte, NC 28221, Proceedings of the 17th International Conference on Environmental Degradation of Materials in Nuclear Power Systems-Water Reactor, Ottawa (Canada), 2015.

Andresen P., Rebak R. and Evan Dolley, *SCC growth rate of irradiated and unirradiated high Cr ferritic steels*, GE Global Research, One Research Circle CE 2513, Schenectady, NY 12309, Proceedings of the 17th International Conference on Environmental Degradation of Materials in Nuclear Power Systems-Water Reactor, Ottawa (Canada), 2015.

Arai T. (1), Hirano T. (2), Aoike S. (3) and Terachi T. (4), *Technical basis of the JSCE standard of the method for measuring the SCC growth rate in high temperature water – specimen size requirement-*, (1) Central Research Institute of Electric Power Industry, 2-11-1 Iwado-kita, Komae, Tokyo, 201-8511, Japan, (2) IHI Corporation, 1, Shinnakahara-cho, Isogo-ku, Yokohama 235-8501, Japan, (3) Hitachi, 7-7-1 Ohmika, Hitachi-shi, Ibaraki, 319-1292, Japan, (4) Institute of Nuclear Safety System, Incorporated, 64 Sata, Mihama-cho, Mikata-gun 919-1205, Fukui, Japan, Proceedings of the 17th International Conference on Environmental Degradation of Materials in Nuclear Power Systems-Water Reactor, Ottawa (Canada), 2015.

Arioka K. (1), Yamada T. (1), Miyamoto T. (2) and Terachi T. (1), *SCC initiation of CW Alloy TT690 and Alloy 600 in PWR water*, (1) lnstitute of Nuclear Safety Systems, Inc., Japan, (2) Kobe Material Testing Laboratory Co., Ltd, Japan, Proceedings of the 17th International Conference on Environmental Degradation of Materials in Nuclear Power Systems-Water Reactor, Ottawa (Canada), 2015.

Ashida Y., Sung S.J., Pan J. and Was G.S., *Experimental and finite element analysis of crack growth in neutron irradiated stainless steels*, University of Michigan, 2355 Bonisteel Blvd., Ann Arbor, MI 48109, USA, Proceedings of the 17th International Conference on Environmental Degradation of Materials in Nuclear Power Systems-Water Reactor, Ottawa (Canada), 2015.

Bae H.Y. (1), Kim T.H. (2), Kim J.H. (2) and Bahn C.B. (1), *Characterization of pre-transition oxides formed on Zirlo™*, (1) School of Mechanical and Nuclear Engineering, Pusan National University (PNU), Busandaehak-ro, 63Beon-gil, Geumjeong-gu Busan. 609-735, Republic of Korea, (2) School of Mechanical and Nuclear Engineering, Ulsan National Institute of Science and Technology (UNIST), 100 Banyeon-ri, Eonyang-eup, Ulju-gun, Ulsan. 689-798, Republic of Korea, Proceedings of the 17th International Conference on Environmental Degradation of Materials in Nuclear Power Systems-Water Reactor, Ottawa (Canada), 2015.

Baldrey D.G. (1), Brown C.M. (2), Burns J.B. (1), Capobianco T.E. (1), Mohr H.M. (1), Morton D.S. (1), Moss T.E. (1), Mullen J.V. (1), Paul L. (3), West E. (1) and Young G.A. (1), *Properties and performance of high chromium nickel alloy filler metal 52i*, (1) Bechtel Marine Propulsion Corporation, Knolls Atomic Power Laboratory, Niskayuna, NY 12309, (2) Bechtel Marine Propulsion Corporation Bettis Atomic Power Laboratory, West Mifflin, PA 15122, (3) Outokumpu VDM USA LLC, Richburg, SC 29706, Proceedings of the 17th International Conference on Environmental Degradation of Materials in Nuclear Power Systems-Water Reactor, Ottawa (Canada), 2015.

Berger S. (1), Kilian R. (1), Hernandez S.E. (1) and Hasse G. (2), *Reliability and long term behaviour of novel accident level measurement devices in simulated fuel pool environment*, (1) AREVA GmbH, Paul-Gossen-Str. 100, 91052 Erlangen, (2) EPCM Global Engineering (Pty) Ltd, 35 Sarel-Baard Crescent Gateway Industrial Park, Centurion, South-Africa, Proceedings of the 17th International Conference on Environmental Degradation of Materials in Nuclear Power Systems-Water Reactor, Ottawa (Canada), 2015.

Bertali G. (1), Scenini F. (1), Gilles P. (2) and Burker M.G. (1), *Solution annealed and thermally treated Alloy 600 preferential intergranular oxidation: a comparison,* (1) The University of Manchester, Material Performance Centre, Manchester (UK), (2) AREVA ,92084 Paris La défense, France, Proceedings of the 17th International Conference on Environmental Degradation of Materials in Nuclear Power Systems-Water Reactor, Ottawa (Canada), 2015.

Bjurman M. (1), Thuvander M. (2), Liu F. (2) and Efsing P. (3), *Phase separation study of in-service thermally aged cast stainless steel – Atom probe thermography*, (1) Studsvik Nuclear AB / Royal Institute of Technology (KTH), Nyköping, SE-611 82, Sweden, (2) Chalmers University of Technology, Department of Applied Physics, Goteborg, SE-412 96, Sweden, (3) Ringhals AB / Royal Institute of Technology (KTH), Väröbacka, SE-430 22, Sweden, Proceedings of the 17th International Conference on Environmental Degradation of Materials in Nuclear Power Systems-Water Reactor, Ottawa (Canada), 2015.

Boccanfuso M., Thébault Y. and Massini B., *The first two occurrences of external damage on 600TT Alloy tubes in France,* EDF-CEIDRE - BP23 - 37420 Avoine – France, Proceedings of the 17th International Conference on Environmental Degradation of Materials in Nuclear Power Systems-Water Reactor, Ottawa (Canada), 2015.

Bock B. (1), Licina G. (2), Jarvis A. (3) and Giannelli J. (3), *Admiralty brass main condenser tube degradation at Fitzpatrick*, (1) James A. FitzPatrick Nuclear Power Plant, PO Box 110, Lycoming, NY. 13039. USA, (2) Structural Integrity Associates, Inc. 5215 Hellyer Ave., Suite 210, San Jose, CA. 95138. USA, (3) Finetech, Inc., 959 US Highway 46 East, Suite 403, Parsippany, NJ. 07054. USA, Proceedings of the 17th International Conference on Environmental Degradation of Materials in Nuclear Power Systems-Water Reactor, Ottawa (Canada), 2015.

Brown P. (1), Mclennan A. (1), Hill T. (1), Medway S. (1), Stairmand J. (1), Jaffer S. (2) and Wright M. (2), *Measurements of fatigue initiation of carbon steel in high temperature water using blunt notch compact tension specimens*, (1) Amec Foster Wheeler, Walton House, Birchwood Park, Warrington, Cheshire, WA3 6GA, UK, (2) Canadian Nuclear Laboratories, Chalk River Laboratories, Chalk River, Ontario, KOJ 1JO, Canada, 17th International Conference on Environmental Degradation of Materials in Nuclear Power Systems-Water Reactor, Ottawa (Canada), 2015.

Bruemmer S.M., Olszta M.J., Overman N.R. and Toloczko M.B., *Cold work effects on stress corrosion crack growth in Alloy 690 tubing and plate materials*, Pacific Northwest National Laboratory, Richland, WA 99352 USA, Proceedings of the 17th International Conference on Environmental Degradation of Materials in Nuclear Power Systems-Water Reactor, Ottawa (Canada), 2015.

Capell B. (1), Wolfe R. (1), Lumsden J. (2), and Eaker R. (3), *PbSCC of Alloy 800NG steam generator tubing in alkaline environments*, (1) Electric Power Research Institute (EPRI), 1300 West WT Harris Blvd., Charlotte, NC 28262, (2) Teledyne Scientific and Imaging Company, 1049 Camino Dos Rios, Thousand Oaks, CA 91360, 3 HKA Enterprises, 337 Spartagreen Blvd, Ducan, SC 29334, Proceedings of the 17th International Conference on Environmental Degradation of Materials in Nuclear Power Systems-Water Reactor, Ottawa (Canada), 2015.

Changizian P., Zhang K.H. and Yao Z., *Investigation into the microstructural changes in Alloy X-750 spacer material during Kr^{2+} / He^{+} dual beam irradiation using in-situ TEM observation*, Department of Mechanical and Materials Engineering, Queen's University, Kingston, ON, K7L 3N6, Proceedings of the 17th International Conference on Environmental Degradation of Materials in Nuclear Power Systems-Water Reactor, Ottawa (Canada), 2015.

Chaumun E. (1,2), Crépin J. (2), Duhamel C. (2), Guerre C. (1), Héripré E. (3), Sennour M. (2) and de Curières I. (4), *SCC crack initiation in nickel based alloy welds in hydrogenated steam at 400°C*, (1) CEA, DEN, DPC, SCCME, Laboratoire d'Etude de la Corrosion Aqueuse, F-91191 Gif-sur-Yvette, France, (2) MINES ParisTech, PSL - Research University, MAT – Centre des matériaux, CNRS UMR 7633, BP 87 91003 Evry, France, (3) Ecole Polytechnique, Laboratoire de Mécanique des Solides, CNRS UMR 7649, 91128 Palaiseau cedex, France, (4) IRSN, Institut de Radioprotection et de Sureté Nucléaire, BP 17, 92262 Fontenay-aux-Roses cedex, France, Proceedings of the 17th International Conference on Environmental Degradation of Materials in Nuclear Power Systems-Water Reactor, Ottawa (Canada), 2015.

Chen Y. (1), Alexandreanu B. (1), Chen W.Y. (1), Li Z. (2), Yang Y. (2), Natesan K. (1) and Rao A.S. (3), *Crack growth rate and fracture toughness J-R curve test on irradiated cast austenitic steels*, (1) Argonne National Laboratory, 9700 S. Cass Ave., Lemont, IL 60439, USA, (2) University of Florida, Gainesville, FL 32611, USA, (3) US Nuclear Regulatory Commission, 11545 Rockville Pike, Rockville, MD 20852, USA, Proceedings of the 17th International Conference on Environmental Degradation of Materials in Nuclear Power Systems-Water Reactor, Ottawa (Canada), 2015.

Chen J. (1), Lu Z. (1,2), Xiao Q. (1), Ru X. (1) and Han G. (1), *The electrochemical behavior and stress corrosion cracking of cold rolled 316L stainless steel in simulated PWR water environments*, (1) Institute of Materials Science, School of Materials Science and Engineering, Shanghai University, Mailbox 269, 149 Yanchang Road, Shanghai, 200072, China, (2) State Key Laboratory of Advanced Special Steels, Shanghai University, 149 Yanchang Road, Shanghai, 200072, China, Proceedings of the 17th International Conference on Environmental Degradation of Materials in Nuclear Power Systems-Water Reactor, Ottawa (Canada), 2015a.

Chen J. (1), Obitz C. (1), Arwin H. (2) and Forssgren B. (3), *Corrosion kinetics of nickel-base alloys with high chromium contents under simulated BWR normal water chemistry conditions and high flow velocity*, (1) Studsvik Nuclear AB, SE-611 82 Nyköping, Sweden, (2) Laboratory of Applied Optics, Department of Physics, Chemistry and Biology, Linköping University, SE-581 83 Linköping, Sweden, (3) Ringhals AB, SE-430 22 Väröbacka, Sweden, Proceedings of the 17th International Conference on Environmental Degradation of Materials in Nuclear Power Systems-Water Reactor, Ottawa (Canada), 2015b.

Nomenclature

AC	Acidic Crevice
AE	Acoustic Emission
AEM	Analytical Electron Microscopy
AES	Auger Electron Spectroscopy
AFEA	Advanced Finite Element Analysis
AFM	Atomic Force Microscopy
AFW	Auxiliary Feed Water
AISI	American Iron and Steel Institute
ALARA	As Low As Reasonably Achievable
ALM	Accident proof Level Measurement
AM	Additive Manufacturing
ANL	Argonne National Laboratory
APM	Adaptive Phased Management
APT	Atom Probe Tomography
ARB	Accumulative Roll Bonding
ASME	American Society of Mechanical Engineers
ASTM	American Society for Testing and Materials
ATEM	Analytical Transmission Electron Microscopy
ATF	Accident Tolerant Fuel
AVT	All Volatile Treatment
B&W	Babcock and Wilcox
BAC	Boric Acid Corrosion
BF	Bright Field or Baffle-to-Former
BHDL	Bottom Head Drain Line
BMI	Bottom Mounted Instrumentation
BR	Belgian Reactor
BRAC	BWR Radiation Assessment and Control program
BSE	Back Scattered Electrons
BWR	Boiling Water Reactor
CANDU	CANnada Deuterium Uranium
CASS	Cast Austenitic Stainless Steels
CDCB	Contoured Double Cantilever Beam
CER	Contact Electric Resistance
CERT	Constant Extension Rate Test
CET	Core Exit Thermocouple
CF	Corrosion Fatigue
CFCGR	Corrosion Fatigue Crack Growth Rate
CFD	Computational Fluid Dynamics
CFR	Code of Federal Regulations
CGHAZ	Coarse Grain HAZ
CGR	Crack Growth Rate
CL	Cold Leg
CNL	Canadian Nuclear Laboratories
CNSC	Canadian Nuclear Safety Commission
CoC	Certificates of Compliance
CP	Cavitation Peening
CPFEM	Crystal Plasticity FEM
CPS	Colloidal Polished Surface
CR	Cold Roll(ed)
CRA	Corrosion Resistant Alloy
CRDM	Control Rod Drive Mechanism
CRSS	Critical Resolved Shear Stress
CRUD	Chalk River Unidentified Deposits

CS	Carbon Steel
CSA	Canadian Standards Association
CSL	Coincidence Site Lattice
CSS	Component, System or Structure
CT	Compact Tension
CTS	Cold Tensile Straining
CVCS	Chemistry and Volume Control System
CW	Cold Work
CZM	Cohesive Zone Model
DC	Direct Current
DC-GB	Dislocation Channel-Grain Boundary
DCPD	Direct Current Potential Drop
DCSS	Dry Cask Storage System
DGR	Deep Geologic Repository
DH	Dissolved Hydrogen
DHC	Delayed Hydride Cracking
DHD	Deep Hole Drilling
DIC	Digital Image Correlation
DM	Dissimilar Metal
DMLM	Direct Metal Laser Melting
DMW	Dissimilar Metal Weld
DO	Dissolved Oxygen
DOE	Department Of Energy
DOE-NE	Department of Energy Office of Nuclear Energy
DOS	Degree Of Sensitization
dpa	displacements per atom
DPI	Dye Penetrate Inspection
DPW	Dearated Pressurized Water
DSA	Dynamic Strain Aging
DW	Deaerated pure Water
D/W	DryWell
EAC	Environmentally Assisted Cracking/Corrosion
EAF	Environmentally Assisted Fatigue
EBSD	Electron BackScattered Diffraction
ECAP	Equal-Channel Angular Pressing
ECP	Electrochemical Corrosion Potential
ECT	Eddy Current Tests
ED	ElectroDialysis
EDF	Electricité de France
EDG	Emergency Diesel Generator
EDM	Electro Discharge Machining
EDS	Energy Dispersive Spectroscopy
EDX	Energy Dispersive X-ray
EDXA	Energy Dispersive X-ray Analysis
EDY	Effective Degradation Year
EELS	Electron Energy Loss Spectrometry
EFPH	Effective Full Power hours
EFPY	Effective Full Power Year
EFTEM	Energy-Filtering Transmission Electron Microscopy
EIS	Electrochemical Impedance Spectroscopy
EOC	End-Of-Cycle
EPFM	Elastic-Plastic Fracture Mechanics
EPR	European Pressurized Reactor
EPRI	Electric Power Research Institute
EPS	ElectroPolished Surface
ESP	Spontaneous Potential
ET	Eddy current Testing
FAC	Flow Accelerated Corrosion
FB	Fusion Boundary

FCAW	Flux Cored Arc Welding
FCG	Fatigue Crack Growth
FD	Flow Distributor
FE	Field Emission
FEA	Finite Elements Analysis
FEGSEM	Field Emission Gun Scanning Electron Microscope
FEGSTEM	Field Emission Gun Scanning Transmission Electron Microscope
FEM	Finite Element Method/Modeling
FFSG	Fitness-For-Service assessment Guidelines
FFT	Fast Fourier Transform
FGTU	Floater Guide Tube Unit
FI	Factor of Improvement
FIB	Focused Ion Beam
FO	Forced Outage
FOI	Factor Of Improvement
FTT	Flux Thimble Tube
GALL	Generic Aging Lessons Learned
GB	Grain Boundary
GBE	Grain Boundary Engineering
GDC	General Design Criterion/Criteria
GDS	Glow Discharge Spectroscopy
GE	General Electric
GIF	Generation IV International Forum
GND	Geometrically Necessary Dislocation
GTAW	Gas Tungsten Arc Welding
HAADF	High-Angle Annular Dark Field
HAGB	High Angle Grain Boundary
HAZ	Heat Affected Zone
HDS	Hold Down Spring
HER	Hydrogen Evolution Reaction
HIP	Hot Isostatic Pressing
HL	Hot Leg
HPT	High Pressure Torsion
HREM	High Resolution Electron Microscopy
HRR	Hutchinson-Rice-Rosengren
HRTEM	High Resolution Transmission Electron Microscopy
HRXR	High-Resolution X-ray Reflectivity
HSSI	Heavy-Section Steel Irradiation
HTW	High Temperature Water
HWC	Hydrogenated Water Chemistry
HWC-M	Hydrogen Water Chemistry in Moderate concentrations
HWI	Heater Well Insert
I&E	Inspection and Evaluation
IAC	Irradiated Accelerated Corrosion
IAD	Irradiation Assisted Degradation
IASCC	Irradiation Assisted Stress Corrosion Cracking
ICI	In-Core Instrumentation
ICP-MS	Inductively Coupled Plasma Mass Spectrometry
ID	Inside Diameter
IG	InterGranular
IGA	InterGranular Attack
IGC	InterGranular Corrosion (cracking)
IGSCC	InterGranular Stress Corrosion Cracking
IIAC	International IASCC Advisory Committee
INL	Idaho National Laboratory
INPO	Institute of Nuclear Power Operations
IPF	Inverse Pole Figure
IRWST	In Containment Refueling Water Storage Tank
IVEC	Injected Vacancy Enhanced Creep

Unit conversion

TEMPERATURE		
°C + 273.15 = K	°C × 1.8 + 32 = °F	
T(K)	T(°C)	T(°F)
273	**0**	32
289	16	61
298	25	77
373	**100**	212
473	**200**	392
573	**300**	572
633	360	680
673	**400**	752
773	**500**	932
783	510	950
793	520	968
823	550	1022
833	560	1040
873	**600**	1112
878	605	1121
893	620	1148
923	650	1202
973	**700**	1292
1023	750	1382
1053	780	1436
1073	**800**	1472
1136	863	1585
1143	870	1598
1173	**900**	1652
1273	**1000**	1832
1343	1070	1958
1478	1204	**2200**

Radioactivity	
1 Sv	= 100 Rem
1 Ci	= 3.7×10^{10} Bq = 37 GBq
1 Bq	= 1 s^{-1}

MASS	
kg	lbs
0.454	**1**
1	2.20

DISTANCE	
x (µm)	x (mils)
0.6	0.02
1	0.04
5	0.20
10	0.39
20	0.79
25	0.98
25.4	**1.00**
100	3.94

PRESSURE		
bar	MPa	psi
1	0.1	14
10	**1**	142
70	7	995
70.4	7.04	**1000**
100	10	1421
130	13	1847
155	15.5	2203
704	70.4	**10000**
1000	100	14211

STRESS INTENSITY FACTOR	
MPa√m	ksi√inch
0.91	**1**
1	1.10